REPORT DOCUMENTATION PAGE

Form Approved
OMB No. 074-0188

1. AGENCY USE ONLY (Leave blank)

2. REPORT DATE
April 1998

3. REPORT TYPE AND DATES COVERED
Final Technical Report - 1/1/95 - 9/30/97

4. TITLE AND SUBTITLE
LARGE EDDY SIMULATION OF SUPERSONIC INLET FLOWS

5. FUNDING NUMBERS
F-49620-95-1-0108

6. AUTHOR(S)
PROF. PARVIZ MOIN
PROF. SANJIVA K. LELE

7. PERFORMING ORGANIZATION NAME(S) AND ADDRESS(ES)

STANFORD UNIVERSITY
MECHANICAL ENGINEERING
FLOW PHYSICS & COMPUTATION
DIVISION
STANFORD, CA 94305-3030

8. PERFORMING ORGANIZATION REPORT NUMBER
2DJA423

9. SPONSORING / MONITORING AGENCY NAME(S) AND ADDRESS(ES)

AFOSR
DR. LEONIDAS SAKELL
110 DUNCAN AVE., STE. B115
BOLLING AFB, DC 20332-0001

NA

10. SPONSORING / MONITORING AGENCY REPORT NUMBER

19980514 104

11. SUPPLEMENTARY NOTES

12a. DISTRIBUTION / AVAILABILITY STATEMENT
APPROVED FOR PUBLIC RELEASE. DISTRIBUTION IS UNLIMITED

12b. DISTRIBUTION CODE

13. ABSTRACT ***(Maximum 200 Words)***

The interaction of a shock wave with a turbulent boundary layer is a central problem in supersonic inlet flows. This work uses numerical and analytical techniques to study shock/turbulence interaction in order to identify and explain factors important in shock/boundary layer interaction. Direct numerical simulation of a normal shock wave with an isotropic turbulent field of vorticity and entropy fluctuations showed that negative upstream correlation between the vorticity and entropy fluctuations enhances the turbulence across the shock. Positive upstream correlation has a suppressing effect. A new numerical method providing excellent high wavenumber resolution while reducing the computational cost was developed. A model with no adjustable constants was developed to study the vortex breakdown resulting from the interaction of canard or forbody vortices with the shock waves in a supersonic inlet flow. Very good agreement with both experiment and computation was obtained. A numerical method to compute shock/turbulence interaction using a conservative form of the Large Eddy Simulation (LES) equations has been developed and validated. LES of the interaction of isotropic turbulence with a normal shock was performed and comparisons with direct numerical simulation (DNS) results were favorable. A new Fortran 90 code has been developed for the computation of shock/turbulence interaction. The code is an improved version of codes used previously in shock/turbulence interaction simulations.

DTIC QUALITY INSPECTED 4

14. SUBJECT TERMS
LARGE EDDY SIMULATION, SUPERSONIC INLET FLOWS, TURBULENCE, SHOCK TURBULENCE

15. NUMBER OF PAGES
90

16. PRICE CODE

17. SECURITY CLASSIFICATION OF REPORT
UNCLASSIFIED

18. SECURITY CLASSIFICATION OF THIS PAGE
UNCLASSIFIED

19. SECURITY CLASSIFICATION OF ABSTRACT
UNCLASSIFIED

20. LIMITATION OF ABSTRACT

NSN 7540-01-280-5500

Standard Form 298 (Rev. 2-89)
Prescribed by ANSI Std. Z39-18
298-102

Final Technical Report for the period January 1, 1995 - September 30, 1997 for the grant entitled:

AIR FORCE OF SCIENTIFIC RESEARCH (AFSC)
NOTICE OF TRANSMITTAL TO DTIC
This technical report has been reviewed and is
approved for public release IAW AFR 190-12
Distribution in unlimited.
Joan Boggs
STINFO Program Manager

Approved for public release;
distribution unlimited.

Large Eddy Simulation of Supersonic Inlet Flows

Parviz Moin and Sanjiva K. Lele

Stanford University

Mechanical Engineering, Flow Physics & Computation Division

Stanford, CA 94305-3030

Prepared with the support of the

Air Force Office of Scientific Research

under AFOSR Grant: F49620-95-1-0108

OVERVIEW

This report summarizes our study of the interaction of a shock wave with turbulent flows for the period 1995–1997. One post–doctoral fellow and one graduate student were supported by this program: Dr. Krishnan Mahesh obtained his degree in 1996 (his thesis was published as Report TF–69, a copy was sent to Dr. Sakell) and Mr. Albert Honein is continuing his doctoral studies in the Department of Mechanical Engineering at Stanford. The salient achievements of this program are presented below. Details are provided in the attached enclosures of relevant reports.

A combination of linear analysis and direct simulation was used by Mahesh, Moin and Lele$^{(1-3)}$ to study the interaction of turbulent shear flow with a normal shock wave. Subsequent to graduation, Dr. Mahesh continued his work as a post-doctoral fellow at the Center for Turbulence Research. His principal accomplishments are as follows:

1. Direct numerical simulation was used to study the interaction of a normal shock wave with an isotropic turbulent field of vorticity and entropy fluctuations. The upstream correlation between the vorticity and entropy fluctuations was shown to strongly influence the evolution of the turbulence across the shock. The validity of Morkovin's hypothesis behind a shock was also examined; shock-front oscillations were found to invalidate the part of the hypothesis relating u_{rms} and T_{rms}. For further details, refer to Part 4 of the report.
2. A new numerical method providing excellent high wavenumber resolution while reducing the computational cost was developed$^{(4)}$. This method is now being incorporated in the shock/boundary layer codes. Refer to Part 3 for details.
3. The vortex breakdown resulting from the interaction of canard or forbody vortices with the shock waves in a supersonic inlet flow was studied. A model with no adjustable constants was developed$^{(5)}$ and very good agreement with both experiment and computation was obtained. Refer to part 2 for details.

The project was extended by Mr. Honein to develop the technology of large-eddy simulation (LES) for turbulent flows with shock waves. His principal achievements are summarized below:

1. A numerical method to compute shock/turbulence interaction using LES has been developed. The important feature of this method is that the energy equation is written

in a conservative form, which is essential in computing flows with shock waves. The method has been validated by computing spatially decaying compressible turbulence.

2. The interaction of isotropic turbulence with a normal shock was computed. For low values of Re_λ, comparisons with direct numerical simulation (DNS) results were favorable. The trends found with DNS at low Re_λ were also observed with LES at higher Re_λ.

3. A new code has been developed for the computation of shock/turbulence interaction. The code is an improved version of codes used previously in shock/turbulence interaction simulations. It is currently being used to study the interaction of a flat plate boundary layer with a normal shock wave.

This report is organized as follows. The development of LES for shock/turbulence interaction is described in Part 1. Part 2 deals with the model used to predict the onset of shock-induced vortex-breakdown. The new numerical method is described in Part 3. Part 4 concludes the report with the influence of entropy fluctuations on the interaction of turbulence with shock waves.

REFERENCES

1. Mahesh, K., Lee, S., Moin, P. & Lele, S.K. (1995) 'The interaction of an isotropic field of acoustic waves with a shock wave', *J. Fluid Mech.* **300**, 383-407.

2. Mahesh, K., Moin, P. & Lele, S.K. (1996) 'The interaction of a shock wave with a turbulent shear flow', Report No. TF–69, Dept. of Mechanical Engineering, Stanford University, Stanford, California.

3. Mahesh, K., Lele, S.K. & Moin, P. (1997) 'The influence of entropy fluctuations on the interaction of turbulence with a shock wave', *J. Fluid Mech.* **334**, 353-379.

4. Mahesh, K. (1996) 'A family of finite difference schemes with good spectral resolution', CTR Manuscript 162, submitted to *J. Comp. Phys.*

5. Mahesh, K. (1996) 'A model for the onset of breakdown in an axisymmetric compressible vortex', *Phys. Fluids*, **8**, 3338-3345.

PART 1

Large eddy simulation of shock turbulence interaction

1. Motivation and objectives

The presence of shock waves is an essential characteristic of high speed flows. Understanding the mechanisms of turbulence interacting with a shock wave is of fundamental importance in predicting the interaction of turbulent boundary layers with shock waves which occur in many engineering applications. The high Reynolds number in practical flows makes direct numerical simulation (DNS) unfeasible. Large eddy simulation (LES), where the large scales of turbulence are resolved and small scale effects are modeled, is thus required for detailed analysis.

The goal of this work is to study shock/wave boundary layer interactions using LES. Toward this goal a simpler problem of the spatial evolution of compressible isotropic turbulence and its interaction with a shock wave were studied first. The developed numerical method for LES was then incorporated in a new code for the simulation of shock/boundary layer interaction. The simulations conducted to test and develop the numerical method for LES are described below. A description of the new code is also provided.

2. Accomplishments

A nonconservative formulation of the energy equation (internal energy) was used to perform large eddy simulations of compressible turbulence in Moin et al. (1991). A conservative form of the energy equation is highly desirable for computing flows containing shocks. A conservative set of equations for LES were derived from the nonconservative equations derived by Moin et al. (1991). The validation of the formulation for spatially decaying turbulence is described in §2.1. Performance of the formulation was compared with a DNS of isotropic turbulence/shock wave interaction, which is reported in §2.2. The new code for shock/turbulence interaction is described in §2.3.

2.1 Spatially evolving compressible turbulence

A separate temporal simulation is advanced in time until realistic turbulent conditions are realized. The resulting field is used to generate inflow turbulence for the spatial calculation. The simulations are advanced in time until statistical convergence is reached.

Taylor's hypothesis is then invoked to compare the spatial simulation to the corresponding temporal one. Comparisons between the two simulations are shown in Figures 1, 2, and 3. The computation corresponds to a microscale Reynolds number $Re_\lambda = 24.4$ and a turbulent Mach number $M_t = 0.39$, specified at the inflow of the spatial simulation. A mesh with 33^3 grid points was used. As seen in Figures 1, 2, and 3, good agreement is obtained.

For higher values of Re_λ, it was noted that a build-up of aliasing errors and insufficient model dissipation prevented the simulations from being advanced for long times. Increasing the streamwise number of points, and using the skew symmetric form in discretizing the continuity equation helped in stabilizing the simulations. Similar agreement with the corresponding temporal simulation was found except for the evolution of the density fluctuations.

2.2 Isotropic turbulence/shock wave interaction

The LES formulation was next applied to the interaction of isotropic turbulence with a shock wave. The parameters used were chosen to reproduce a DNS of isotropic turbulence/shock wave interaction performed by Mahesh et al. (1997). The mean Mach number was 1.29 and the inflow turbulence had a Re_λ of 19.1 and a turbulent Mach number M_t of 0.14.

A summary of the numerical method used follows. A uniform mesh is used in the two homogeneous directions and a stretched mesh is used in the non-homogeneous direction. In computing spatial derivatives, a sixth order essentially non-oscillatory (ENO) shock capturing scheme is used for the shock region while a sixth order Padé scheme is used outside of this region. A third order Runge-Kutta method is used for time advancement. Finally, a sponge layer where the flow is forced towards the laminar solution is used for the outflow boundary condition.

Results shown in Figures 4 and 5 indicate that shock/turbulence interaction at this Re_λ is well predicted by LES, with moderate savings in computation time and in memory usage. Simulations at a higher inflow Re_λ of 49, where DNS cannot be used, were also performed (Figures 6 and 7). It is observed that the trends found at low Re_λ are also obtained at higher Re_λ.

2.3 New code for shock/turbulence interaction

A spectral, finite-difference hybrid code was developed and is currently being applied to the normal shock wave/flate plate boundary layer interaction calculations. The numerical methodology used in our previous computations of shock/turbulence interaction was implemented. In addition, a spectral Fourier collocation scheme was employed in the homogeneous spanwise direction. This code is written in Fortran 90 and is an optimized version of our previous codes used in the shock/turbulence calculations. It runs four times faster and requires only half the memory. Finally, it is highly structured and will be easily ported and optimized for use on parallel machines.

REFERENCES

1. Moin, P., Squires, K., Cabot, W. & Lee, S. (1991) 'A dynamic subgrid-scale model for compressible turbulence and scalar transport', *Phys. Fluids A.*, **3**, 2746-2757.
2. Mahesh, K., Lele, S.K. & Moin, P. (1997) 'The influence of entropy fluctuations on the interaction of turbulence with a shock wave', *J. Fluid Mech.* **334**, 353-379.

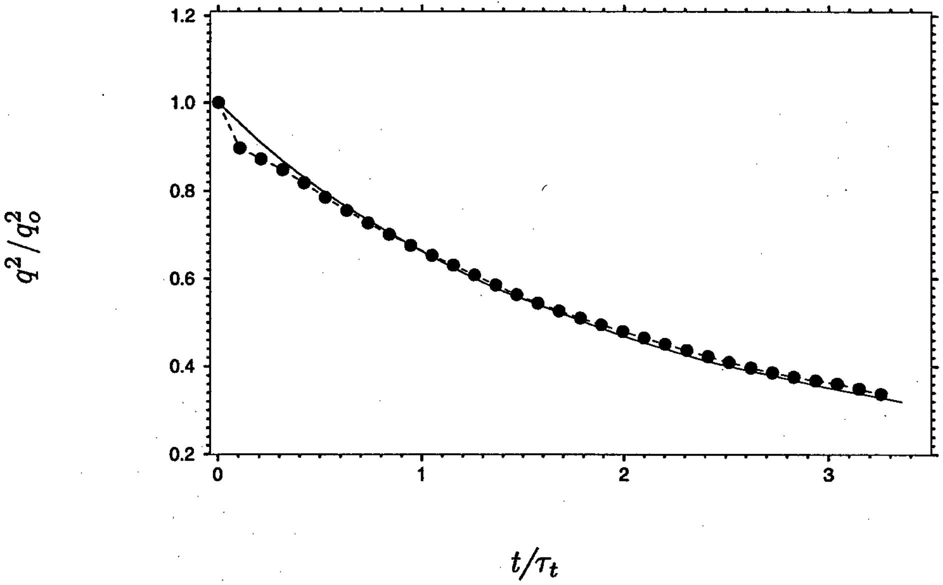

FIGURE 1. Comparison of the temporal (——) and spatial (•) evolution of the turbulent kinetic energy. Conditions at the inflow correspond to Re_λ=24.4 and M_t=0.39 (τ_t is the turbulence time scale).

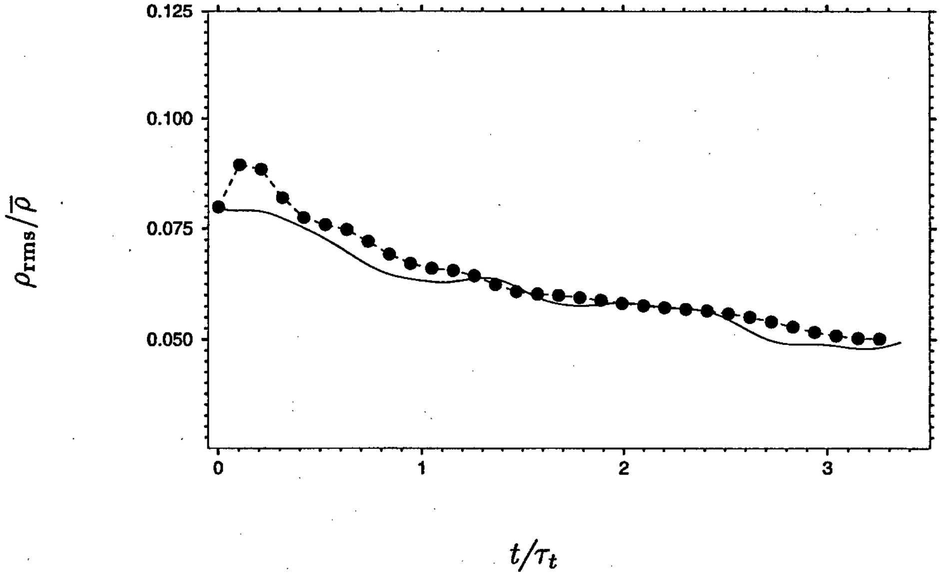

FIGURE 2. Comparison of the temporal (——) and spatial (•) evolution of the density fluctuations. Conditions at the inflow correspond to Re_λ=24.4 and M_t=0.39 (τ_t is the turbulence time scale).

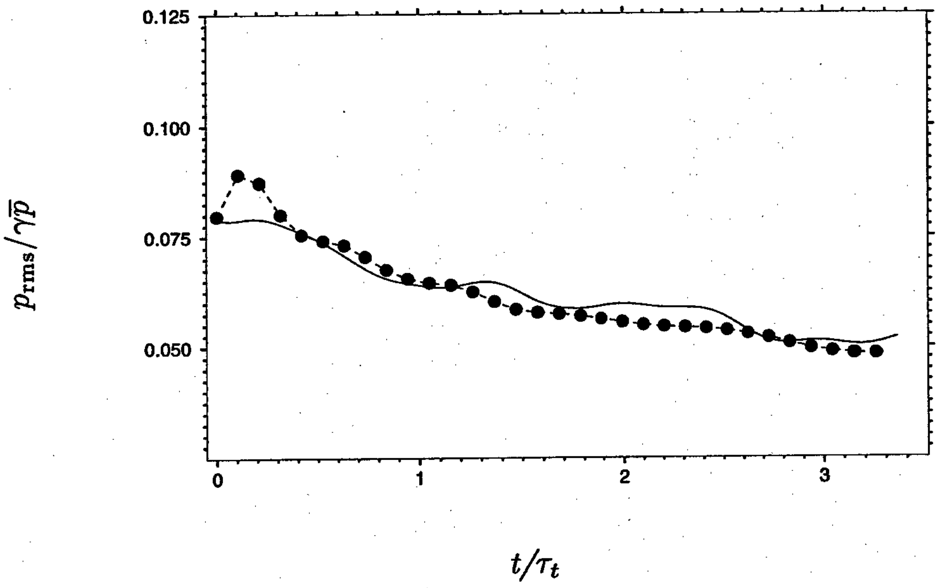

FIGURE 3. Comparison of the temporal (———) and spatial (•) evolution of the pressure fluctuations. Conditions at the inflow correspond to Re_λ=24.4 and M_t=0.39 (τ_t is the turbulence time scale).

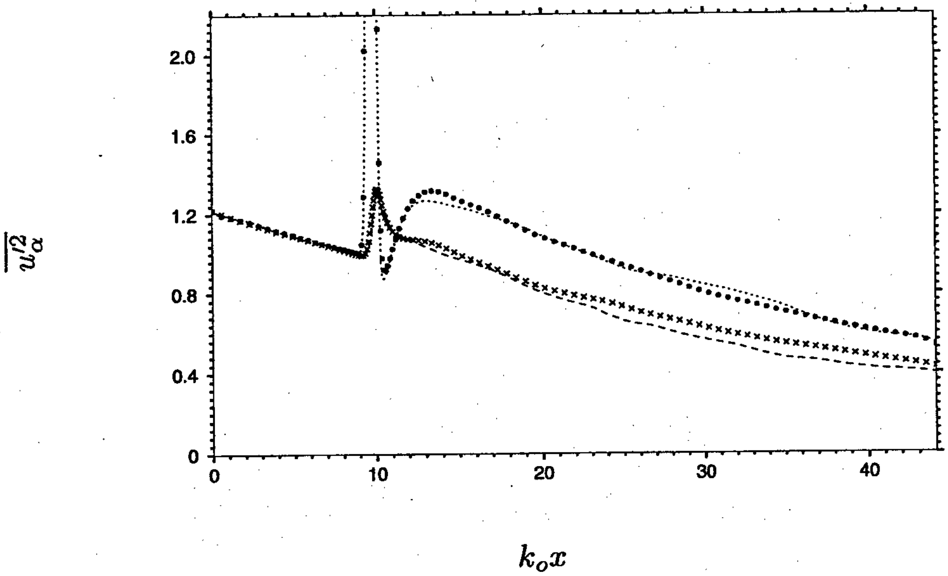

FIGURE 4. Streamwise evolution of the turbulent kinetic energy components across a Mach 1.29 shock wave with inflow $Re_\lambda = 19.1$. All the curves are normalized by their value immediately upstream of the shock. DNS : • $\overline{u'^2}$, × $\overline{v'^2}$; LES : ········ $\overline{u'^2}$, ---- $\overline{v'^2} = \overline{w'^2}$.

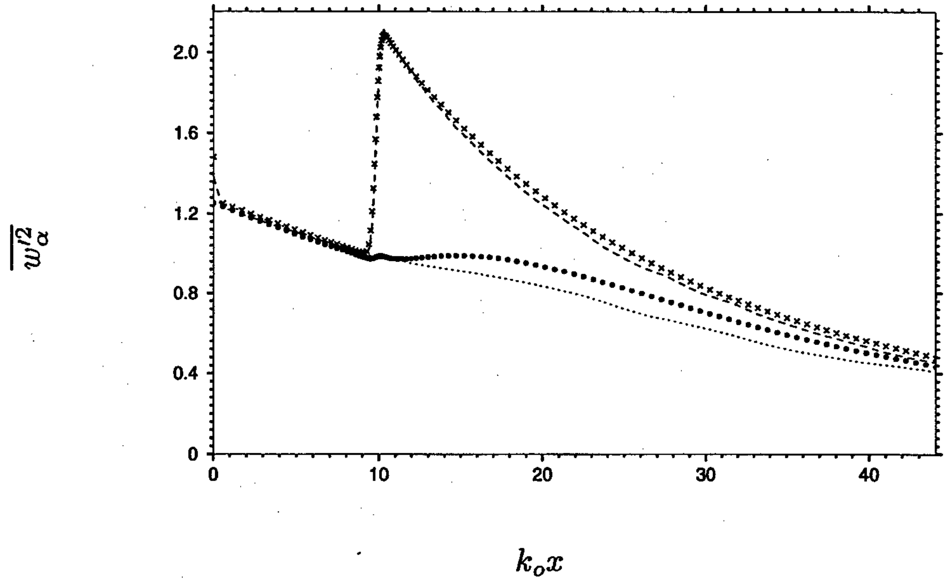

FIGURE 5. Streamwise evolution of vorticity fluctuations across a Mach 1.29 shock wave with inflow $Re_\lambda = 19.1$. All the curves are normalized by their value immediately upstream of the shock. DNS : • $\overline{w_1'^2}$, × $\overline{w_2'^2} = \overline{w_3'^2}$; LES : ········ $\overline{w_1'^2}$, ---- $\overline{w_2'^2} = \overline{w_3'^2}$.

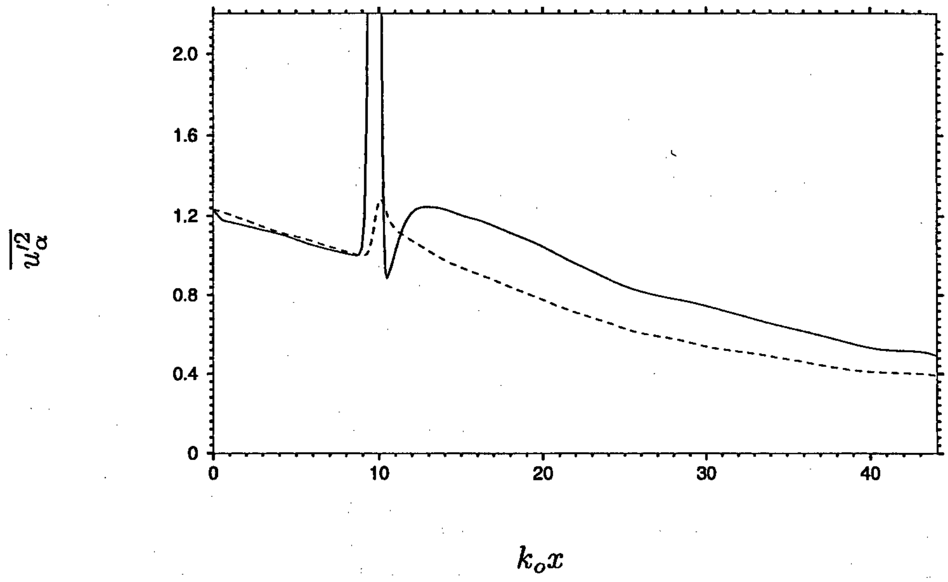

FIGURE 6. Streamwise evolution of the turbulent kinetic energy components from LES of a Mach 1.29 shock wave with inflow $Re_\lambda = 49$. All the curves are normalized by their value immediately upstream of the shock. ——— $\overline{u'^2}$, ---- $\overline{v'^2} = \overline{w'^2}$.

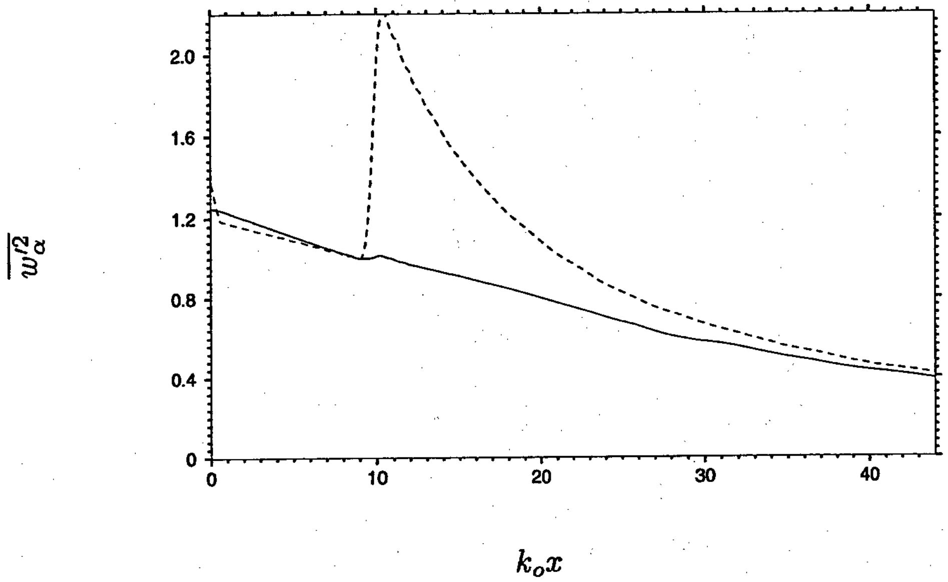

FIGURE 7. Streamwise evolution of vorticity fluctuations from LES of a Mach 1.29 shock wave with inflow $Re_\lambda = 49$. All the curves are normalized by their value immediately upstream of the shock. —— $\overline{w_1'^2}$, ---- $\overline{w_2'^2} = \overline{w_3'^2}$.

PART 2

A model for the onset of breakdown in an axisymmetric compressible vortex

Krishnan Mahesh[a)]
Center for Turbulence Research, Stanford University, Stanford, California 94305

(Received 28 May 1996; accepted 5 September 1996)

A simple inviscid model to predict the onset of breakdown in an axisymmetric vortex is proposed. Three problems are considered: the shock-induced breakdown of a compressible vortex, the breakdown of a free compressible vortex, and the breakdown of a free incompressible vortex. The same physical reasoning is used in all three problems to predict the onset of breakdown. It is hypothesized that breakdown is the result of the competing effects of adverse pressure rise and streamwise momentum flux at the vortex centerline. Breakdown is assumed to occur if the pressure rise exceeds the axial momentum flux. A formula with no adjustable constants is derived for the critical swirl number in all three problems. The dependence of the critical swirl number on parameters such as upstream Mach number, excess/deficit in centerline axial velocity, and shock oblique angle is explored. The predictions for the onset of shock-induced breakdown and free incompressible breakdown are compared to experiment and computation, and good agreement is observed. Finally, a new breakdown map is proposed. It is suggested that the adverse pressure rise at the vortex axis be plotted against the axial momentum flux to determine the onset of breakdown. The proposed map allows the simultaneous comparison of data from flows ranging from incompressible breakdown to breakdown induced by a shock wave. © *1996 American Institute of Physics.* [S1070-6631(96)02112-5]

I. INTRODUCTION

A large body of information exists (e.g. see the review articles by Hall,[1] Leibovich,[2] Wedemeyer,[3] Escudier,[4] Stuart,[5] and Delery[6]) on the breakdown of incompressible streamwise vortices. Less is known about vortex breakdown at high speeds. An interesting example of supersonic vortex breakdown is the breakdown induced by the interaction of the vortex with a shock wave. The flow in supersonic engine inlets and over high-speed delta wings constitute technologically important examples of this phenomenon, which is termed "shock-induced vortex breakdown."

Gustintsev *et al.*[7] and Zatoloka *et al.*[8] appear to have conducted the earliest investigations into shock-induced vortex breakdown. The qualitative similarity of the flow to that of a separated boundary layer was noted in these experiments. Subsequently, Horowitz,[9] Delery *et al.*,[10] Metwally *et al.*,[11] and Cattafesta and Settles[12] have experimentally studied vortex breakdown induced by a normal shock. The interaction between streamwise vortices and wedge-attached oblique shock waves was experimentally investigated by Kalkhoran and Sforza.[13]

Horowitz[9] and Delery *et al.*[10] were the first to quantitatively characterize the nature of the breakdown. Their experiments studied normal shocks of strength equal to Mach 1.6, 1.75, 2 and 2.28. At each Mach number, they varied the swirl in the incident vortex and identified a critical swirl number above which the vortex would break down. The results were plotted on a "breakdown map" of swirl number against Mach number, where it was observed that the critical swirl number decreased as the Mach number of the shock increased. A companion numerical study using the Euler equations supported the experimentally observed trends. The experiments by Metwally *et al.*[11] and Cattafesta and Settles[12] extended the range of available data to Mach 4. Based on their visualization of the flow, Metwally *et al.*[11] proposed a qualitative picture of the flow-field resulting from the breakdown of the vortex.

Rizzetta[14] obtained numerical solutions to the Reynolds averaged Euler and Navier–Stokes equations, with the objective of predicting Kalkhoran and Sforza's[13] experimental measurements of pressure distribution on the wedge. The swirling supersonic flow in a circular duct was computed by Kandil *et al.*[15,16] who provided qualitative flow-field information on the breakdown. The most extensive computations of shock-induced vortex breakdown are the recent calculations by Erlebacher *et al.*[17] These workers studied the interaction between a streamwise vortex and a normal shock wave using the unsteady, axisymmetric, compressible Navier–Stokes equations. Mach numbers from 1.3 to 10 were computed. In the same spirit as Delery *et al.*,[10] a critical swirl number was numerically identified at each Mach number, and a breakdown map of swirl number against Mach number made. The trend observed by Delery *et al.*[10] was seen to extend to Mach 10; i.e., the critical swirl number decreased with increasing Mach number. Some interesting features of the flow field were also highlighted.

The only attempt to quantitatively predict some aspect of shock-induced breakdown appears to have been made by Cattafesta[18] who equated the ratio of swirl number (downstream to upstream) across the shock wave to the velocity ratio (upstream to downstream) across the shock. By comparing to experimental data, he obtained a value of 0.6 for the swirl number behind the shock wave. More recently, Erlebacher *et al.*[17] have proposed an empirical correlation between the critical swirl number and the Mach number of the shock wave, based on a curve fit to their data.

[a)] Phone: (415) 723-9599; Fax: (415) 723-9617; Electronic mail: krishnan@leland.stanford.edu

1070-6631/96/8(12)/3338/8/$10.00

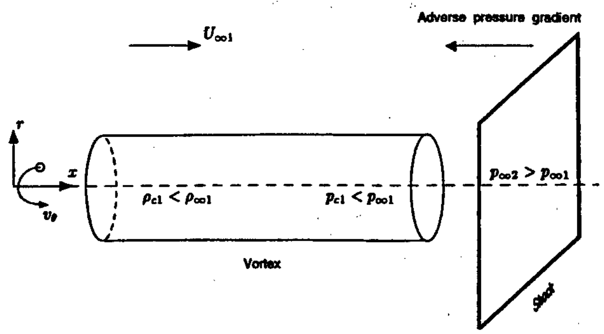

FIG. 1. Schematic of the interaction between a streamwise vortex and a normal shock wave.

In this paper, we propose a model to predict the onset of shock-induced vortex breakdown. The proposed model has no adjustable constants, and is compared to both experiment and computation. Also, the dependence of the critical swirl number on parameters such as the upstream Mach number, excess/deficit in centerline axial velocity, and shock oblique angle is explored. Two other problems are then considered: the breakdown of a free compressible vortex, and free incompressible vortex breakdown. The same breakdown criterion is used in all three problems to predict the onset of breakdown. Finally, a new breakdown map is proposed, that allows the simultaneous comparison of data from flows ranging from incompressible breakdown to breakdown induced by a shock wave.

This paper is organized as follows. A description of the upstream vortex is first provided in Section II A. This is followed in Section II B by a description of the proposed breakdown criterion and expressions for the critical swirl number. Section III compares the model predictions to computation and experiment. The influence of centerline excess/deficit in axial velocity, and obliquity of the shock wave is also discussed. The onset of breakdown in a free compressible vortex is discussed in Section IV. Incompressible vortex breakdown is briefly considered in Section V. A new breakdown map is then proposed in Section VI. The paper is concluded with a brief summary in Section VII.

II. STATEMENT OF PROBLEM

Figure 1 shows a schematic of the interaction between a streamwise vortex and a normal shock wave. The axial flow is from left to right. The variables x and r are used to denote the axial and radial coordinate respectively. The axial and swirl components of velocity are denoted by U and v_θ respectively, and p, ρ and T represent the pressure, density and temperature. The subscripts "∞" and "c" correspond to values in the free-stream and the centerline of the vortex, and the states upstream and downstream of the shock wave are respectively denoted by the subscripts "1" and "2" (e.g., $p_{\infty 2}$ denotes the free-stream pressure downstream of the shock wave).

A description of the incident vortex is first provided in Section II A. This is followed in Section II B by an outline of the model.

A. The upstream vortex

Studies of incompressible vortex breakdown (e.g. Darmofal[19]) suggest that the onset of breakdown is generally independent of viscosity for vortex Reynolds number (based on free-stream axial velocity and core radius) greater than about 300. As a result, viscosity is neglected in this paper. The upstream vortex is therefore governed by the axisymmetric, compressible Euler equations. It is readily seen that the profiles,

$$v_\theta = v_\theta(r), \quad U = U(r), \quad p = p(r), \quad \rho = \rho(r) \tag{1}$$

trivially satisfy the continuity, axial momentum and energy equations. The radial momentum equation,

$$\frac{dp}{dr} = \frac{\rho v_\theta^2}{r} \tag{2}$$

remains to be satisfied. Experiments[10,12] show that the swirl profile of the Burgers vortex is a good fit to experimental data. However, the Burgers profile makes analytical solution difficult. As a result, this paper uses the Rankine vortex as an approximation for the upstream vortex. Non-dimensionalizing the radial coordinate by the core radius (location where v_θ is maximum) and velocity by the peak value of the swirl velocity (denoted by $v_{\theta m}$), the swirl velocity profile of the upstream vortex is given by,

$$\begin{aligned} \tilde{v}_\theta &= \tilde{r}, \quad \tilde{r} \leqslant 1 \\ &= \frac{1}{\tilde{r}}, \quad \tilde{r} \geqslant 1, \end{aligned} \tag{3}$$

where the tilde is used to denote non-dimensional variables.

The density varies with radius for a compressible vortex. This paper considers two different idealizations of the thermodynamic field in the upstream vortex: spatially uniform stagnation temperature and spatially uniform entropy. The assumption of uniform stagnation temperature is prompted by experimental data. Delery *et al.*[10] note that the total temperature in the upstream vortex in their experiments is approximately uniform. Measurements in a Mach 3 vortex by Metwally *et al.*[11] and Cattafesta and Settles[12] seem to support this approximation. Cattafesta and Settles' data (Fig. 7 of their paper) show a deficit of about 4% of free-stream in total temperature at the centerline. The idealization of uniform entropy is prompted by past theoretical and computational studies on compressible vortices (e.g. Colonius *et al.*[20]).

Expressions for the centerline pressure and density for the uniform stagnation temperature vortex and uniform entropy vortex are obtained below. Defining the non-dimensional variables,

$$\tilde{p} = \frac{p}{p_\infty}, \quad \tilde{\rho} = \frac{\rho}{\rho_\infty}, \quad \tilde{T} = \frac{T}{T_\infty} \tag{4}$$

the radial momentum equation becomes,

$$\frac{d\tilde{p}}{d\tilde{r}} = \gamma(\Gamma M_\infty)^2 \tilde{\rho} \frac{\tilde{v}_\theta^{\,2}}{\tilde{r}}. \tag{5}$$

The variable γ denotes the ratio of specific heats and is taken as 1.4 in this paper. Γ is the swirl number of the vortex, and is defined as $\Gamma=v_{\theta m}/U_\infty$. M_∞ is the free-stream Mach number, defined as $M_\infty=U_\infty/c_\infty$. ΓM_∞ will be recognized as the swirl Mach number, $v_{\theta m}/c_\infty$.

Uniform entropy vortex: If the entropy is spatially uniform,

$$\tilde{p}=\tilde{\rho}^{\gamma}. \tag{6}$$

Expressing the density in terms of the pressure in the radial momentum equation and integrating yields the following expressions for the centerline pressure and density:

$$\begin{aligned}\tilde{p}_c&=[1-(\gamma-1)\Gamma^2M_\infty^2]^{\gamma/(\gamma-1)},\\ \tilde{\rho}_c&=[1-(\gamma-1)\Gamma^2M_\infty^2]^{1/(\gamma-1)}.\end{aligned} \tag{7}$$

Uniform stagnation temperature vortex: The spatial uniformity of stagnation temperature requires that

$$T+\frac{U^2+v_\theta^2}{2C_p}=T_\infty+\frac{U_\infty^2}{2C_p}. \tag{8}$$

Delery *et al.*'s[10] experiments show that the axial velocity in the upstream vortex was nearly uniform; i.e., $U=U_\infty$. Cattafesta and Settles[12] on the other hand, observe a wake-like profile. This paper assumes uniform axial velocity for the uniform stagnation temperature vortex. This yields the following expression for the non-dimensional temperature in the vortex:

$$\tilde{T}=1-\frac{\gamma-1}{2}(\Gamma M_\infty)^2\tilde{v}_\theta{}^2. \tag{9}$$

The equation of state implies that $\tilde{p}=\tilde{\rho}\,\tilde{T}$. Substituting for $\tilde{\rho}$ and $\tilde{T}$ in the radial momentum equation and integrating yields the following expressions for the density and pressure at the centerline of the uniform stagnation temperature vortex:

$$\begin{aligned}\tilde{p}_c&=\left[1-\frac{(\gamma-1)}{2}\Gamma^2M_\infty^2\right]^{2\gamma/(\gamma-1)},\\ \tilde{T}_c&=1,\quad \tilde{\rho}_c=\tilde{p}_c.\end{aligned} \tag{10}$$

B. A criterion for shock-induced breakdown

A simple criterion for breakdown of the upstream vortex is first proposed. The properties of the upstream vortex (Section II A) are then used to obtain an expression for the critical swirl number above which the vortex would break down. The breakdown criterion is based upon an approximation to the axial momentum equation at the centerline of the vortex. Note that as a result of axisymmetry, the radial velocity at the centerline would be zero. When combined with the swirl velocity being zero at the centerline, this suggests that the flow near the vortex centerline would largely be in the streamwise direction. The one-dimensional momentum equations may therefore be used to model the flow around the vortex centerline. $p+\rho U^2$ would therefore be constant across a region of rapid streamwise variation.

Consider the vortex impinging upon the shock wave. On account of the rotation, the pressure at the center of the vortex is less than the free-stream value; i.e., $p_{c1}<p_{\infty1}$. Pressure rises across a shock wave; i.e., $p_{\infty2}>p_{\infty1}$. The vortex therefore experiences an adverse streamwise pressure rise, which may be quantified by the pressure difference, $p_{\infty2}-p_{c1}$. The fluid in the vortex has a certain inertia in the streamwise direction, which may be quantified by the streamwise momentum flux, $\rho_{c1}U_{c1}^2$. Breakdown is assumed to occur if the axial pressure rise exceeds the upstream streamwise momentum flux, thereby stagnating the flow; i.e., if

$$p_{\infty2}-p_{c1}\geqslant\rho_{c1}U_{c1}^2\geqslant\rho_{c1}U_{\infty1}^2\left(1+\frac{\Delta U}{U_{\infty1}}\right)^2 \tag{11}$$

where ΔU denotes the upstream excess in axial velocity at the centerline. If the axial velocity is uniform, then $\Delta U=0$. The threshold for breakdown is therefore given by the relation,

$$p_{\infty2}-p_{c1}=\rho_{c1}U_{\infty1}^2\left(1+\frac{\Delta U}{U_{\infty1}}\right)^2. \tag{12}$$

The axial velocity is assumed to be uniform through most of this paper. The effect of non-uniform axial velocity is separately discussed in Section III B. Equation (12) may be rewritten in non-dimensional form for uniform axial velocity as,

$$\tilde{p}_{\infty2}-\tilde{p}_{c1}=\gamma\tilde{\rho}_{c1}M_{\infty1}^2. \tag{13}$$

We have already obtained expressions for $\tilde{p}_{c1}$ and $\tilde{\rho}_{c1}$ in terms of Γ and $M_{\infty1}$. The Rankine–Hugoniot equations for a normal shock express $\tilde{p}_{\infty2}$ in terms of the upstream Mach number, $M_{\infty1}$. Substituting for $\tilde{p}_{c1}$, $\tilde{\rho}_{c1}$ and $\tilde{p}_{\infty2}$ into the above breakdown criterion will therefore yield an expression for the critical swirl number Γ_{crit} in terms of Mach number of the shock wave for a vortex with uniform axial velocity. This expression is derived below.

Uniform stagnation temperature vortex: For a uniform stagnation temperature vortex, we have $\tilde{\rho}_{c1}=\tilde{p}_{c1}$. Substitution into the criterion for breakdown [Eq. (13)] yields,

$$\tilde{p}_{c1}=\frac{\tilde{p}_{\infty2}}{1+\gamma M_{\infty1}^2}, \tag{14}$$

where $\tilde{p}_{\infty2}$ is given by the Rankine–Hugoniot equations as,

$$\tilde{p}_{\infty2}=1+\frac{2\gamma}{\gamma+1}(M_{\infty1}^2-1). \tag{15}$$

Substituting for $\tilde{p}_{c1}$ from Eq. (10) and $\tilde{p}_{\infty2}$ from Eq. (15) into Eq. (14), we get,

$$\begin{aligned}&\left[1-\frac{\gamma-1}{2}\Gamma_{\text{crit}}^2M_{\infty1}^2\right]^{2\gamma/(\gamma-1)}\\ &\quad=\frac{1}{1+\gamma M_{\infty1}^2}\left[1+\frac{2\gamma}{\gamma+1}(M_{\infty1}^2-1)\right],\end{aligned} \tag{16}$$

which upon rearrangement yields the following expression for the critical swirl number as a function of the Mach number of the shock:

$$\Gamma_{\text{crit}}=\frac{1}{M_{\infty 1}}\sqrt{\frac{2}{\gamma-1}\left\{1-\left(\frac{1}{1+\gamma M_{\infty 1}^{2}}\left[1+\frac{2\gamma}{\gamma+1}(M_{\infty 1}^{2}-1)\right]\right)^{(\gamma-1)/2\gamma}\right\}}. \tag{17}$$

Uniform entropy vortex: Expressions for the centerline density and temperature for a uniform entropy vortex are given by Eq. (7). Substitution into Eq. (13) yields the following implicit equation for the critical swirl number as a function of the Mach number:

$$1+\frac{2\gamma}{\gamma+1}(M_{\infty 1}^{2}-1)-[1-(\gamma-1)\Gamma_{\text{crit}}^{2}M_{\infty 1}^{2}]^{\gamma/(\gamma-1)} = \gamma M_{\infty 1}^{2}[1-(\gamma-1)\Gamma_{\text{crit}}^{2}M_{\infty 1}^{2}]^{1/(\gamma-1)}. \tag{18}$$

The Newton–Raphson method was used to solve the above equation for Γ_{crit} as a function of the Mach number of the shock wave.

III. RESULTS: SHOCK-INDUCED VORTEX BREAKDOWN

A. Uniform axial velocity

Results for the critical swirl number are presented for the case where the axial velocity is uniform. Figure 2 shows the predicted values of the critical swirl number as a function of the Mach number of the shock. The predicted values are compared to the experimental values reported by Delery *et al.*[10] (the data were obtained from Fig. 35 of their paper) for Mach numbers of 1.75, 2 and 2.28. Also shown are results from the computations by Erlebacher *et al.*[17] (the data were obtained from Table 3 of their report). Note that the computational data at Mach 1.7 were very close to the experimental value at Mach 1.75 (0.331 as compared to 0.33). This made the experimental data hard to discern when both experimental and computational results were plotted. As a result, the computational value at Mach 1.7 is not plotted in Fig. 2.

The predicted values are seen to be in good agreement with both experiment and computation. The critical swirl number is predicted to decrease with increasing Mach number as observed. According to the proposed criterion [Eqs. (7), (10) and (13)], this decrease in Γ_{crit} is due to a combination of two factors: increase in the adverse pressure rise (due to $\tilde{p}_{\infty 2}$ increasing while $\tilde{p}_{c1}$ decreases) and decrease in streamwise momentum flux (due to $\tilde{\rho}_{c1}$ decreasing) with increasing Mach number.

The ability of the model to predict the onset of shock-induced breakdown is further evaluated in Fig. 3, where data from Metwally *et al.*[11] are plotted (obtained from Fig. 6 of their paper). The "strong interactions" observed experimentally are seen to lie in the region where the model predicts breakdown, while the "weak interaction" regions lie in the predicted region of non-breakdown. Note that the curve of Γ_{crit} in Fig. 3 assumes uniform axial velocity. Metwally *et al.*[11] point out that the Mach 3 and Mach 3.5 vortices had noticeable deficit in centerline velocity for the breakdown cases. As will be seen in Section III B, the critical swirl number is predicted to decrease as the centerline velocity decreases; i.e., the filled symbols for the Mach 3 and Mach 3.5 cases would move further into the breakdown region if the deficit in centerline velocity were accounted for in Fig. 3.

B. Non-uniform axial velocity

The influence of an excess/deficit in the centerline axial velocity on the critical swirl number is next considered. For

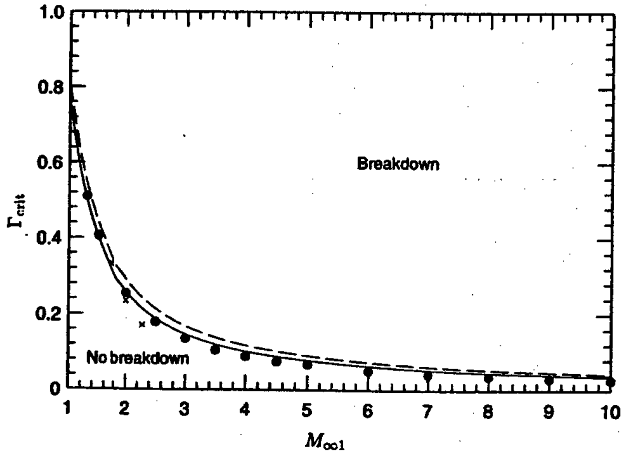

FIG. 2. Comparison of predicted critical swirl number to experiment and computation of shock-induced vortex breakdown. — (Prediction: uniform stagnation temperature), — (prediction: uniform entropy), ● (computation—Ref. 17), × (experiment—Ref. 10).

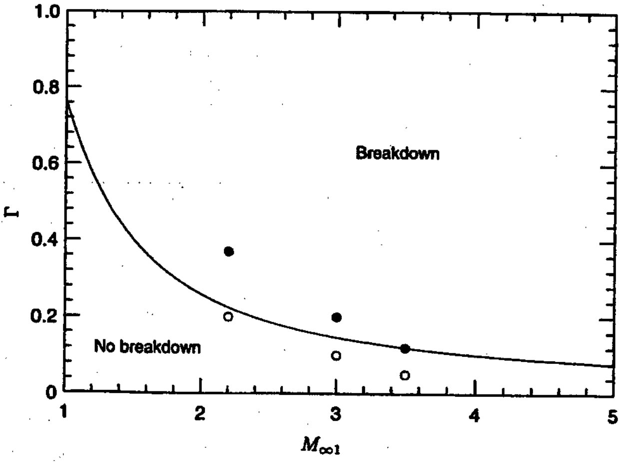

FIG. 3. Evaluation of model in predicting the onset of shock-induced vortex breakdown. — (Predicted Γ_{crit} [Eq. (17)]: uniform stagnation temperature), ● (experiment—Ref. 11: breakdown), ○ (experiment—Ref. 11: no breakdown).

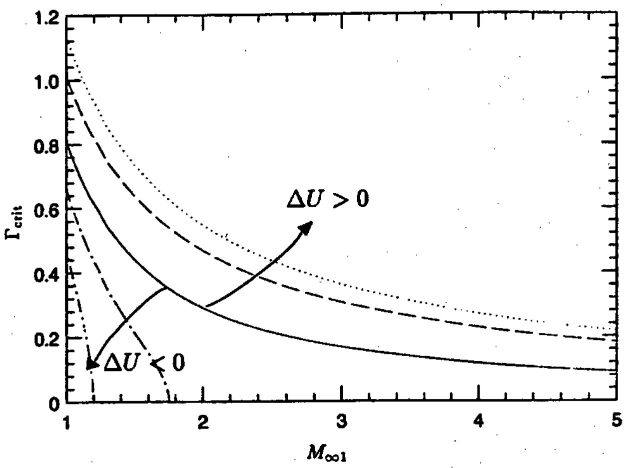

FIG. 4. Influence of axial velocity on the onset of vortex breakdown induced by a shock. —·— ($\Delta U/U_{\infty 1}=-0.5$), – – – ($\Delta U/U_{\infty 1}=-0.25$), — ($\Delta U/U_{\infty 1}=0$), --- ($\Delta U/U_{\infty 1}=0.5$), ··· ($\Delta U/U_{\infty 1}=1$).

convenience, results are shown only for the uniform entropy vortex. The breakdown criterion [Eq. (12)] may be divided through by $p_{\infty 1}$ to yield the following non-dimensional criterion:

$$\tilde{p}_{\infty 2}-\tilde{p}_{c1}=\gamma\tilde{\rho}_{c1}M_{\infty 1}^2\left(1+\frac{\Delta U}{U_{\infty 1}}\right)^2. \tag{19}$$

Substituting for $\tilde{p}_{c1}$ and $\tilde{\rho}_{c1}$ from Eqs. 7, we get the following equation for Γ_{crit} as a function of $M_{\infty 1}$ and $\Delta U/U_{\infty 1}$:

$$\begin{aligned}\tilde{p}_{\infty 2}-&[1-(\gamma-1)\Gamma_{\text{crit}}^2M_{\infty 1}^2]^{\gamma/(\gamma-1)}\\&=\gamma M_{\infty 1}^2\left(1+\frac{\Delta U}{U_{\infty 1}}\right)^2[1-(\gamma-1)\Gamma_{\text{crit}}^2M_{\infty 1}^2]^{1/(\gamma-1)}.\end{aligned} \tag{20}$$

The Newton–Raphson method was used to solve the above equation for Γ_{crit}, after expressing $\tilde{p}_{\infty 2}$ in terms of $M_{\infty 1}$. Figure 4 shows the variation of the critical swirl number with Mach number for different values of $\Delta U/U_{\infty 1}$. Note that $\Delta U>0$ corresponds to a jet-like axial velocity profile of the upstream vortex while $\Delta U<0$ corresponds to a wake-like profile. The predicted results show a strong sensitivity to the excess/deficit in centerline axial velocity. Jet-like profiles of the axial velocity are observed to delay breakdown, while a wake-like profile makes the vortex more susceptible to breakdown. The same trend is known to apply in the breakdown of an incompressible vortex, where axial blowing is often used to alleviate the breakdown.[6]

Figure 4 shows that for vortices with a wake-like axial velocity, the critical swirl number becomes zero at a finite Mach number; i.e., breakdown is predicted at and beyond this cut-off Mach number, even in the absence of swirl . This result may be explained as follows. In the absence of swirl, the "vortex" reduces to an axisymmetric wake (or jet). This wake (or jet) can undergo reverse flow accompanied by radial outflow upon experiencing a strong enough adverse pressure gradient. We have assumed that breakdown occurs when the adverse pressure rise at the vortex centerline exceeds the centerline axial momentum flux. We noted that on account of its rotation, the centerline pressure rise, $p_{\infty 2}-p_{c1}$ is greater than the free-stream rise, $p_{\infty 2}-p_{\infty 1}$. Also, rotation results in the centerline density (ρ_{c1}) being lower than the free-stream density. As a result, the centerline momentum flux, $\rho_{c1}U_{c1}^2$ is less than its value computed using the free-stream density. Thus, swirl "amplifies" (in the terminology of Hall[1]) the adverse pressure rise experienced by the vortex while suppressing the axial momentum flux. Both factors make the vortex more susceptible to breakdown. This implies that if the free-stream pressure rise exceeds the axial momentum flux computed using the free-stream density, then the presence of swirl is not needed for "breakdown." The flow at and above the cut-off Mach number corresponds to this scenario. The cut-off Mach number (denoted by M_{cut}) can therefore be predicted by the following criterion:

$$p_{\infty 2}-p_{\infty 1}=\rho_{\infty 1}U_{c1}^2 \tag{21}$$

which yields,

$$\tilde{p}_{\infty 2}-1=\gamma M_{\text{cut}}^2\left(1+\frac{\Delta U}{U_{\infty 1}}\right)^2. \tag{22}$$

Substituting for $\tilde{p}_{\infty 2}$ from Eq. (15), we get the following equation for the cut-off Mach number in terms of the velocity excess/deficit:

$$\frac{2\gamma}{\gamma+1}(M_{\text{cut}}^2-1)=\gamma M_{\text{cut}}^2\left(1+\frac{\Delta U}{U_{\infty 1}}\right)^2 \tag{23}$$

which may be rearranged to obtain the following expression for the cut-off Mach number:

$$M_{\text{cut}}=\sqrt{\frac{2\gamma}{\gamma+1}\left[\frac{2\gamma}{\gamma+1}-\gamma\left(1+\frac{\Delta U}{U_{\infty 1}}\right)^2\right]^{-1}}. \tag{24}$$

C. Breakdown induced by an oblique shock wave

If the shock wave were oblique, the onset of breakdown would be expected to depend on the oblique angle. Although the interaction of an oblique shock with an axisymmetric vortex is not axisymmetric, it is envisioned that the onset of breakdown can be predicted by extending the arguments of the previous section. Reiterating the criterion for breakdown for uniform axial velocity, we require that $\tilde{p}_{\infty 2}-\tilde{p}_{c1}=\gamma\tilde{\rho}_{c1}M_{\infty 1}^2$. The influence of shock obliquity is modeled as follows. The properties of the upstream vortex ($\tilde{p}_{c1},\tilde{\rho}_{c1}$) depend solely upon the free-stream Mach number and swirl number. However the pressure behind the shock ($\tilde{p}_{\infty 2}$) is determined by the normal Mach number, $M_{\infty 1}\sin\alpha$ (α denotes the angle the shock makes with the streamwise direction). Replacing $M_{\infty 1}$ in Eq. (15) by $M_{\infty 1}\sin\alpha$ to obtain $\tilde{p}_{\infty 2}$ and substituting as before for $\tilde{p}_{c1}$ and $\tilde{\rho}_{c1}$ yields the following expressions for the critical swirl number.

Uniform stagnation temperature vortex:

$$\Gamma_{\text{crit}}=\frac{1}{M_{\infty 1}}\sqrt{\frac{2}{\gamma-1}\left\{1-\left(\frac{1}{1+\gamma M_{\infty 1}^2}\left[1+\frac{2\gamma}{\gamma+1}([M_{\infty 1}\sin\alpha]^2-1)\right]\right)^{(\gamma-1)/2\gamma}\right\}}. \tag{25}$$

Uniform entropy vortex:

$$1+\frac{2\gamma}{\gamma+1}([M_{\infty 1}\sin\alpha]^2-1)-[1-(\gamma-1)\Gamma_{\text{crit}}^2M_{\infty 1}^2]^{\gamma/(\gamma-1)}=\gamma M_{\infty 1}^2[1-(\gamma-1)\Gamma_{\text{crit}}^2M_{\infty 1}^2]^{1/(\gamma-1)}. \tag{26}$$

It is readily seen that for the same upstream Mach number, Γ_{crit} is predicted to increase as the shock becomes increasingly oblique. This prediction may be explained by noting that the pressure rise across an oblique shock is lower than that for a normal shock at the same Mach number. As a result, the adverse pressure rise that the vortex experiences is smaller, thereby delaying the onset of breakdown.

IV. SHOCK-FREE BREAKDOWN OF A COMPRESSIBLE VORTEX

Section III discussed vortex breakdown induced by a shock wave. The breakdown of a free axisymmetric vortex, i.e. breakdown in the absence of an externally imposed pressure gradient, is considered in this section. Incompressible streamwise vortices at sufficiently high swirl number are known to break down, even in the absence of an externally applied adverse pressure gradient. It is to be expected that their high-speed counterparts would exhibit similar behavior. The critical swirl number in high-speed flow would be a function of the Mach number. This section derives an expression for the critical swirl number in terms of the free-stream Mach number; i.e., we consider the influence of compressibility on the breakdown of a free vortex. The arguments used are identical to those in breakdown induced by a shock. The only difference is that while the adverse pressure rise was set equal to $p_{\infty 2}-p_{c1}$ for shock-induced breakdown, it is set equal to $p_{\infty 1}-p_{c1}$ for the shock-free breakdown. The rationale for this assumption is that in the absence of the shock, the vortex discharges into the atmosphere. As a result, the vortex sees a pressure equal to $p_{\infty 1}$ ahead of it, as well as in the free-stream. The difference between atmospheric pressure ($p_{\infty 1}$), and the pressure at the vortex centerline (p_{c1}) provides the adverse pressure rise that causes breakdown. Breakdown of the vortex is therefore assumed to occur when

$$p_{\infty 1}-p_{c1}\geqslant\rho_{c1}U_{c1}^2. \tag{27}$$

The criterion for shock-free breakdown is therefore given by,

$$1-\bar{p}_{c1}=\gamma\bar{\rho}_{c1}M_{\infty 1}^2 \tag{28}$$

which is identical to the expression obtained when $\bar{p}_{\infty 2}$ is set to 1 in Eq. (13). The corresponding expressions for the critical swirl number are given below.

Uniform stagnation temperature vortex:

$$\Gamma_{\text{crit}}=\frac{1}{M_{\infty 1}}\sqrt{\frac{2}{\gamma-1}\left[1-\left(\frac{1}{1+\gamma M_{\infty 1}^2}\right)^{(\gamma-1)/2\gamma}\right]}. \tag{29}$$

Uniform entropy vortex:

$$1-[1-(\gamma-1)\Gamma_{\text{crit}}^2M_{\infty 1}^2]^{\gamma/(\gamma-1)} = \gamma M_{\infty 1}^2[1-(\gamma-1)\Gamma_{\text{crit}}^2M_{\infty 1}^2]^{1/(\gamma-1)}. \tag{30}$$

Figure 5 shows the predicted values of the critical swirl number as a function of the free-stream Mach number. Also shown (for supersonic flow) are the values obtained for breakdown induced by a shock wave at the same Mach number. Compressibility is seen to make the vortex more susceptible to breakdown. A similar trend was noted by Keller.[21] This trend may be explained by noting [Eqs. (7) and (10)] that increase in the free-stream Mach number decreases the centerline pressure and density, thereby increasing the adverse pressure rise while decreasing the axial momentum flux. The predicted values of Γ_{crit} in the absence of the shock are seen to be greater than those predicted for shock-induced breakdown. This trend can be explained by noting that the pressure rise across the shock wave produces a larger adverse pressure rise for the same upstream momentum flux.

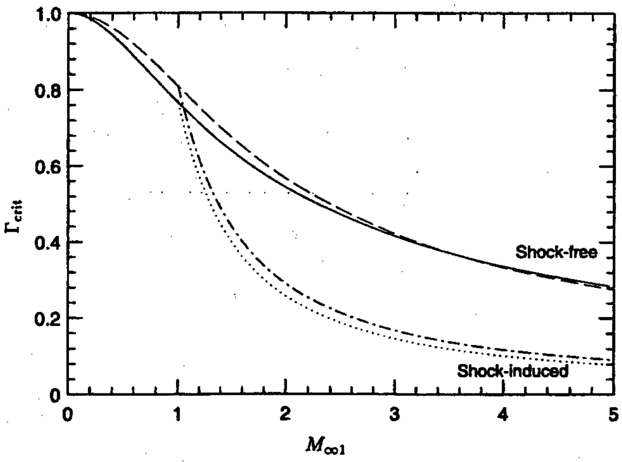

FIG. 5. Predicted critical swirl number for shock-free vortex breakdown compared to the prediction for shock-induced breakdown. — (Shock-free: uniform stagnation temperature), --- (shock-free: uniform entropy), ··· (shock-induced: uniform stagnation temperature), -·- (shock-induced: uniform entropy).

TABLE I. Prediction of critical swirl number for incompressible vortex breakdown compared to other approaches. All data other than the present reproduced from review article by Delery (Ref. 6).

	S_{crit}
Quasi-cylindrical	1.41
Axisymmetric N-S	1.35
Bossel	1.12
Squire	1.4
Benjamin	1.4
Num. simulation	1.28
Spall *et al.*	1.37
Present	**1.4**

V. INCOMPRESSIBLE VORTEX BREAKDOWN

Figure 5 shows that as $M_{\infty 1}$ tends towards 0, Γ_{crit} tends towards 1. An incompressible vortex in the absence of externally imposed adverse pressure gradients, is therefore predicted to undergo breakdown at a critical swirl number of one. The same result can of course be derived, by setting $\rho = \rho_\infty$ in the radial momentum equation and integrating to obtain the centerline pressure ($p_{c1} = p_{\infty 1} - \rho_\infty v_{\theta m}^2$), which is then substituted into the breakdown criterion [Eq. (27)]. In a recent review article, Delery[6] documents (Section 3.4.5 of his paper) critical swirl numbers for incompressible vortex breakdown as predicted by different theories. He considers a Burgers vortex, and defines a swirl parameter S as

$$S = \frac{C}{r_c U_\infty}, \tag{31}$$

where the variables C and r_c denote the circulation and core radius respectively. For a Burgers vortex, the swirl velocity is given by (Eq. 1 in Delery's[6] paper)

$$v_\theta = \frac{C}{r}\left[1 - e^{-1.256(r/r_c)^2}\right]. \tag{32}$$

This implies that the swirl parameter S is related to the swirl number Γ by,

$$S = \frac{\Gamma}{1 - e^{-1.256}} = 1.398\Gamma. \tag{33}$$

Thus $\Gamma_{\text{crit}} = 1$ corresponds to $S_{\text{crit}} = 1.398 \approx 1.4$. We reproduce in Table I, from Delery's[6] paper, the critical swirl numbers predicted by different approaches. Most approaches are seen to predict values very close to that predicted by our simple criterion.

VI. A "UNIVERSAL" BREAKDOWN MAP

The preceding sections presented results for the onset of vortex breakdown by plotting the critical swirl number as a function of Mach number. The curve $\Gamma_{\text{crit}} = \Gamma_{\text{crit}}(M_{\infty 1})$ defined the boundary between the regimes of breakdown and non-breakdown. However, it is clear that the critical swirl number is not universal (as also observed by Delery[6]). For example, Section III B (Fig. 4) showed that Γ_{crit} depended on the velocity excess/deficit at the centerline. If the breakdown were precipitated by an oblique shock wave as opposed to a normal shock, then Γ_{crit} was noted to depend on the inclination angle of the shock. Similarly, if the breakdown were that of a free vortex instead of being shock induced, yet another curve for the critical swirl number was obtained.

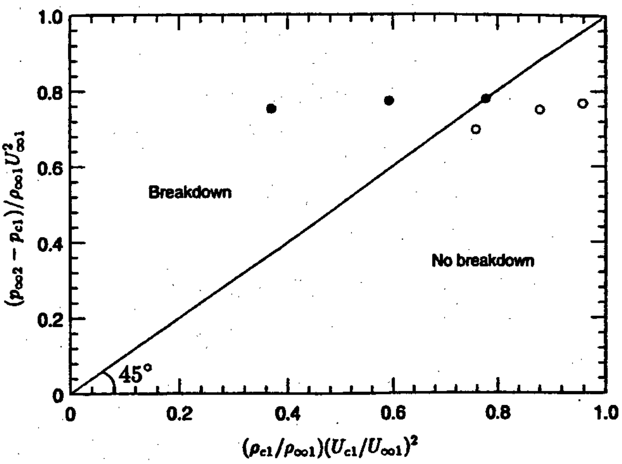

FIG. 6. Evaluation of the proposed breakdown map in predicting the onset of vortex breakdown. ● (Experiment: breakdown), ○ (experiment: no breakdown).

In this section, we propose a breakdown map that allows a common breakdown boundary to be defined for all of the above mentioned problems. The proposed map is based on the breakdown criterion that was proposed in Section II B; i.e.,

$$p_{\infty 2} - p_{c1} \geqslant \rho_{c1} U_{c1}^2. \tag{34}$$

Recall that the same criterion with $p_{\infty 2}$ appropriately defined, was applied to all the breakdown problems discussed in this paper. This suggests that a plot of $p_{\infty 2} - p_{c1}$ against $\rho_{c1} U_{c1}^2$ could be used to map the onset of vortex breakdown. The proposed map could even be used for incompressible vortex breakdown, and would be expected to adequately represent the onset of breakdown induced by pressure gradients acting over distances that are small as compared to a characteristic length scale of the vortex. The curve $p_{\infty 2} - p_{c1} = \rho_{c1} U_{c1}^2$ (the 45° line) would act as the boundary between the breakdown and non-breakdown regimes. Note that the proposed map does not require any additional data to be measured. Experimental information on parameters such as $\Gamma, \Delta U/U_\infty, M_\infty$ and shock angle could be used to obtain both the pressure rise and the axial momentum flux using the equations in Section II A. The proposed map is illustrated in Fig. 6. Note that the pressure rise and momentum flux are nondimensionalized by $\rho_{\infty 1} U_{\infty 1}^2$ to allow incompressible data to be plotted. Data from Metwally [11] (the same data shown in Fig. 3) are also shown. The data from Fig. 3 are combined with Eq. 10 to determine the pressure rise and axial momentum flux. The breakdown and non-breakdown cases are seen to be appropriately delineated.

VII. SUMMARY

A simple inviscid model was proposed to predict the onset of breakdown in an axisymmetric vortex. Three problems were considered: the shock-induced breakdown of a compressible vortex, the breakdown of a free compressible vortex, and the breakdown of a free incompressible vortex.

The same physical reasoning was used to predict the onset of breakdown in all three problems. It was hypothesized that breakdown is the result of the competing effects of adverse pressure rise and streamwise momentum flux at the vortex centerline. Breakdown was assumed to occur if the pressure rise exceeded the axial momentum flux. A formula with no adjustable constants was derived for the critical swirl number in all three problems. The dependence of the critical swirl number on parameters such as upstream Mach number, excess/deficit in centerline axial velocity, and shock oblique angle was explored. The predictions for the onset of shock-induced breakdown and free incompressible breakdown were compared to experiment and computation, and good agreement was observed. Finally, a new breakdown map was proposed as an alternative to the map of critical swirl number against free-stream Mach number. The new map was based on the observation that the same breakdown criterion was used in all the problems considered in this paper. To determine the onset of breakdown, it was suggested that the adverse pressure rise at the vortex centerline, be plotted against the axial momentum flux. The proposed map allows the simultaneous comparison of data from flows ranging from incompressible breakdown to breakdown induced by a shock wave.

ACKNOWLEDGMENTS

This work was supported by the AFOSR under Contract No. F49620-92-J-0128 with Dr. Len Sakell as technical monitor. I am thankful to Professor Sanjiva Lele and Professor Parviz Moin, and Keith Lucas for useful discussions. I am grateful to Professor Peter Bradshaw for his comments on a draft of this manuscript.

[1] M. G. Hall, "Vortex breakdown," Annu. Rev. Fluid Mech. **4**, 195 (1972).

[2] S. Leibovich, "The structure of vortex breakdown," Annu. Rev. Fluid Mech. **10**, 221 (1978).

[3] E. Wedemeyer, "Vortex breakdown," AGARD-VKI Lecture Series 121: High angle of attack aerodynamics, 1982.

[4] M. Escudier, "Vortex breakdown: Observations and explanations," Prog. Aerosp. Sci. **25**, 189 (1988).

[5] J. T. Stuart, "A critical review of vortex breakdown theory," Vortex Control and Breakdown Behavior, Second International Colloquium on Vortical Flows, Baden, Switzerland 1987 (unpublished).

[6] J. M. Delery, "Aspects of vortex breakdown," Prog. Aerosp. Sci. **30**, 1 (1993).

[7] Y. A. Gustintsev, V. V. Zelentsov, V. S. Ilyukhin, and V. S. Pokhil, "Structure of underexpanded supersonic swirling gas jet," Izv. Akad. Nauk SSR, Mech. Zhidk. Gaza **4**, 158 (1969).

[8] V. V. Zataloka, A. K. Ivanyushkin, and A. V. Nikolayev, "Interference of vortices with shocks in airscoops. Dissipation of vortices," Fluid Mech. - Sov. Res. **7**, 195 (1978).

[9] E. Horowitz, "Contribution a l'etude de l'eclatement tourbillonaire en ecoulement. Interaction onde de choc-tourbillon," Ph.D. thesis, Universite Pierre et Marie Curie, Paris, 1984.

[10] J. M. Delery, E. Horowitz, O. Leuchter, and J. L. Solignac, "Fundamental studies on vortex flows," Rech. Aerospat. **2**, 1 (1984).

[11] O. Metwally, G. S. Settles, and C. Horstman, "An experimental study of shock/vortex interaction," AIAA Paper 89-0082, 1989 (unpublished).

[12] L. N. Cattafesta III and G. S. Settles, "Experiments on shock/vortex interaction," AIAA Paper 92-0315, 1992 (unpublished).

[13] I. M. Kalkhoran and P. M. Sforza, "Airfoil pressure measurements during oblique shock wave-vortex interaction in a Mach 3 stream," AIAA J. **32**, 783 (1994).

[14] D. P. Rizzetta, "Numerical simulation of oblique shock wave/vortex interaction," AIAA J. **33**, 1441 (1995).

[15] O. A. Kandil, H. A. Kandil, and C. H. Liu, "Computation of steady and unsteady compressible quasi-axisymmetric vortex flow and breakdown," AIAA Paper 91-0752, 1991 (unpublished).

[16] O. A. Kandil, H. A. Kandil, and C. H. Liu, "Supersonic quasi-axisymmetric vortex breakdown," AIAA Paper 91-3311, 1991 (unpublished).

[17] G. Erlebacher, M. Y. Hussaini, and C-W Shu, "Interaction of a shock with a longitudinal vortex," NASA CR-198332, ICASE Report No. 96-31, 1996.

[18] L. N. Cattafesta III, "An experimental investigation of shock/vortex interaction," Ph.D. thesis, Pennsylvana State University, 1992.

[19] D. L. Darmofal, "A study of the mechanisms of axisymmetric vortex breakdown," Ph.D. thesis, Massachusetts Institute of Technology, 1993.

[20] T. Colonius, S. K. Lele, and P. Moin, "The free compressible viscous vortex," J. Fluid Mech. **230**, 45 (1991).

[21] J. J. Keller, "On the practical application of vortex breakdown theory to axially symmetric and three-dimensional compressible flow," Phys. Fluids **6**, 1515 (1994).

PART 3

CENTER FOR TURBULENCE RESEARCH

A family of high order finite difference schemes with good spectral resolution

K. Mahesh

September 1996

CTR Manuscript 162

Center for Turbulence Research
Bldg. 500
Stanford University
Stanford, CA 94305-3030

A family of high order finite difference schemes with good spectral resolution

Krishnan Mahesh

Center for Turbulence Research, Stanford University, Stanford, California 94305

ABSTRACT

This paper presents a family of finite difference schemes for the first and second derivatives of smooth functions. The schemes are Hermitian and symmetric, and may be considered a more general version of the standard compact (Padé) schemes discussed by Lele [1]. They are different from the standard Padé schemes, in that the first and second derivatives are evaluated simultaneously. For the same stencil width, the proposed schemes are two orders higher in accuracy, and have significantly better spectral representation. Eigenvalue analysis, and numerical solutions of the one-dimensional wave equation are used to demonstrate the numerical stability of the schemes. The computational cost of computing both derivatives is assessed, and shown to be essentially the same as the standard Padé schemes. The proposed schemes appear to be attractive alternatives to the standard Padé schemes for computations of the Navier Stokes equations.

1. INTRODUCTION

Fluid flows in the transitional and turbulent regimes possess a wide range of length and time scales. The numerical computation of these flows therefore requires numerical methods that can accurately represent the entire, or at least a significant portion, of this range of scales. The length scales that are resolved by a computation are determined by the resolution; the accuracy with which these scales are represented depends upon the numerical scheme. Fourier analysis (see *e.g.* [2]) describes both, the range of scales present, and the accuracy with which they are computed (exactly for problems with periodic boundary conditions, and in a WKB sense for more general problems). Such analysis of finite difference schemes (see *e.g.* Fig. 1 in [1]) shows that the error in computing the first and second derivatives can be quite large for the smaller scales. This small scale inaccuracy becomes increasingly important as the energy in the small scales becomes increasingly comparable to that of the large scales; *i.e.*, as the spectrum becomes increasingly 'flat'. This situation is commonly encountered in computations, particularly large-eddy simulations, of high Reynolds number turbulence. As shown by Kravchenko and Moin [3] the inaccurate numerical representation of the small scales in these large-eddy simulations can result in the numerical error overwhelming the contribution of the subgrid-scale model.

Finite difference schemes may be classified as 'explicit' or 'implicit'. Explicit schemes express the nodal derivatives as an explicit weighted sum of the nodal values of the function, *e.g.*, $f'_i = (f_{i+1} - f_{i-1})/2h$, and $f''_i = (f_{i+1} - 2f_i + f_{i-1})/h^2$. Throughout this paper, f_i and f_i^k denote the values of the function and its k^{th} derivative respectively, at the node $x = x_i$, and h denotes the uniform mesh spacing. By comparison, implicit (compact) equate a weighted sum of the nodal derivatives to a weighted sum of the function, *e.g.*, $f'_{i-1}+4f'_i+f'_{i+1}=3(f_{i+1}-f_{i-1})/h$, and $f''_{i-1}+10f''_i+f''_{i+1}=12(f_{i+1}-2f_i+f_{i-1})/h^2$. It is well known [1,4,5] that implicit schemes have better small scale accuracy, than explicit schemes with the same stencil width. This increase in accuracy is achieved at the cost of inverting a banded (usually tridiagonal) matrix to obtain the nodal derivatives. Since tridiagonal matrices can be inverted quite efficiently [6], the implicit schemes are extremely attractive when explicit time advancement schemes are used. The most popular of the implicit schemes (also called Padé schemes due to their derivation from Padé approximants) appear to be the symmetric fourth and sixth order versions (see *e.g.* [1]). There have been several recent computations of transitional boundary layers [7-10], turbulent flows [11-13] and flow-generated noise [14-15] that have used the Padé schemes to evaluate the spatial derivatives. The standard Padé schemes are symmetric and therefore non-dissipative; a non-symmetric compact scheme was recently developed by Adams and Shariff [16].

This paper presents a related family of finite difference schemes for the spatial derivatives in the Navier Stokes equations. The proposed schemes are more accurate than the standard Padé schemes, while incurring essentially the same computational cost. They are based on Hermite interpolation, and may be considered a more general version of the standard Padé schemes described in [1]. For the same stencil width as the Padé schemes, the proposed schemes have higher order of accuracy and better spectral representation. This is achieved by simultaneously solving for the first and second derivatives. When defined on a uniform mesh†, the schemes are of the form,

$$a_1 f'_{i-1}+a_0 f'_i+a_2 f'_{i+1}+h(b_1\, f''_{i-1}+b_0 f''_i+b_2 f''_{i+1}) = \frac{1}{h}(c_1 f_{i-2}+c_2 f_{i-1}+c_0 f_i+c_3 f_{i+1}+c_4 f_{i+2}) \tag{1}$$

Note that the above expression differs from the standard Padé schemes, in that the left-hand side contains a linear combination of the first and second derivatives. The stencil and the coefficients are restricted to be symmetric in this paper. The resulting schemes are therefore non-dissipative. The width of the stencil is taken to be three on the left-hand side and five on the right. This corresponds to the stencil width of the popular sixth-order Padé scheme.

The motivation to formulate schemes that simultaneously evaluate both derivatives is provided by the Navier Stokes equations requiring both derivatives of most variables. Consider for example the one-dimensional compressible equations in primitive form (extension to multiple dimensions is straightforward). We have:

$$\frac{\partial \rho}{\partial t}+u\frac{\partial \rho}{\partial x}=-\rho\frac{\partial u}{\partial x}. \tag{2a}$$

---

† This paper develops the schemes on uniform meshes. It is assumed that computations with non-uniform grids can define analytical mappings between the non-uniform grid and a corresponding uniform grid. The metrics of the mapping may then be used to relate the derivatives on the uniform grid to those on the non-uniform grid.

$$\rho\left(\frac{\partial u}{\partial t}+u\frac{\partial u}{\partial x}\right)=-RT\frac{\partial \rho}{\partial x}-R\rho\frac{\partial T}{\partial x}+\underbrace{\frac{4}{3}\mu\frac{\partial^2 u}{\partial x^2}+\frac{4}{3}\frac{\partial u}{\partial x}\frac{\mathrm{d}\mu}{\mathrm{d}T}\frac{\partial T}{\partial x}}_{\frac{\partial}{\partial x}\left(\frac{4}{3}\mu\frac{\partial u}{\partial x}\right)}. \tag{2b}$$

$$\rho C_v\left(\frac{\partial T}{\partial t}+u\frac{\partial T}{\partial x}\right)=-\rho RT\frac{\partial u}{\partial x}+\frac{4}{3}\mu\left(\frac{\partial u}{\partial x}\right)^2+\underbrace{k\frac{\partial^2 T}{\partial x^2}+\frac{\mathrm{d}k}{\mathrm{d}T}\left(\frac{\partial T}{\partial x}\right)^2}_{\frac{\partial}{\partial x}\left(k\frac{\partial T}{\partial x}\right)}. \tag{2c}$$

The variables ρ, u and T denote the density, velocity and temperature respectively, while R, μ, k and C_v denote the specific gas constant, dynamic viscosity, thermal conductivity and specific heat at constant volume. Note that the viscous terms are expanded prior to their evaluation. This is because direct evaluation of the second derivatives is significantly more accurate than two applications of a first derivative operator. Equation 2 shows that the following spatial derivatives need to be evaluated:

$$\frac{\partial u}{\partial x},\quad \frac{\partial^2 u}{\partial x^2},\quad \frac{\partial T}{\partial x},\quad \frac{\partial^2 T}{\partial x^2},\quad \text{and}\quad \frac{\partial \rho}{\partial x}.$$

Thus, a scheme that simultaneously evaluates both derivatives would only be performing one unnecessary evaluation ($\partial^2\rho/\partial x^2$).

Next, consider the conservative form of the equations. The viscous terms are still evaluated in their non-conservative form, for the reasons given above. We have:

$$\frac{\partial \rho}{\partial t}+\frac{\partial}{\partial x}(\rho u)=0. \tag{3a}$$

$$\frac{\partial}{\partial t}(\rho u)+\frac{\partial}{\partial x}\left(\rho u^2\right)+\frac{\partial p}{\partial x}=\frac{4}{3}\mu\frac{\partial^2 u}{\partial x^2}+\frac{4}{3}\frac{\partial u}{\partial x}\frac{\mathrm{d}\mu}{\mathrm{d}T}\frac{\partial T}{\partial x}. \tag{3b}$$

$$\begin{aligned}\frac{\partial E_t}{\partial t}+\frac{\partial}{\partial x}(E_t u)+\frac{\partial}{\partial x}(pu) =& u\left(\frac{4}{3}\mu\frac{\partial^2 u}{\partial x^2}+\frac{4}{3}\frac{\partial u}{\partial x}\frac{\mathrm{d}\mu}{\mathrm{d}T}\frac{\partial T}{\partial x}\right)+\frac{4}{3}\mu\left(\frac{\partial u}{\partial x}\right)^2\\ &+k\frac{\partial^2 T}{\partial x^2}+\frac{\mathrm{d}k}{\mathrm{d}T}\left(\frac{\partial T}{\partial x}\right)^2.\end{aligned} \tag{3c}$$

Equation 3 requires the following spatial derivatives to be obtained:

$$\frac{\partial}{\partial x}(\rho u),\quad \frac{\partial}{\partial x}\left(\rho u^2\right),\quad \frac{\partial p}{\partial x},\quad \frac{\partial u}{\partial x},\quad \frac{\partial^2 u}{\partial x^2},\quad \frac{\partial T}{\partial x},\quad \frac{\partial^2 T}{\partial x^2},\quad \frac{\partial}{\partial x}(E_t u),\quad \text{and}\quad \frac{\partial}{\partial x}(pu).$$

As one might expect, the conservative formulation requires fewer simultaneous derivative evaluations. However, if the chain rule is invoked as follows, then a formulation that evaluates both derivatives is still attractive. First evaluate (simultaneously)

$$\frac{\partial}{\partial x}(\rho u),\quad \frac{\partial^2}{\partial x^2}(\rho u),\quad \frac{\partial}{\partial x}\left(\rho u^2\right),\quad \frac{\partial^2}{\partial x^2}\left(\rho u^2\right),\quad \frac{\partial \rho}{\partial x},\quad \frac{\partial^2 \rho}{\partial x^2},\quad \frac{\partial}{\partial x}(E_t u),\quad \frac{\partial^2}{\partial x^2}(E_t u),$$
$$\frac{\partial}{\partial x}(pu),\quad \text{and}\quad \frac{\partial^2}{\partial x^2}(pu).$$

The chain rule may then be used to obtain $\partial u/\partial x$, $\partial^2 u/\partial x^2$, $\partial p/\partial x$ and $\partial^2 p/\partial x^2$. The equation of state and the chain rule then yield $\partial T/\partial x$ and $\partial^2 T/\partial x^2$. In this manner, a total of only ten derivative evaluations are performed for the nine derivatives that are needed. The increase in accuracy that is obtained by the simultaneous evaluation of derivatives will be seen to make this additional derivative evaluation worthwhile.

For the same stencil width, the standard Padé schemes are two orders higher in accuracy and have better spectral representation than the corresponding symmetric, explicit schemes. The implicit relation between the derivatives in the Padé schemes yields additional degrees of freedom that allow higher accuracy to be achieved. It is therefore to be expected that including the second derivatives in the implicit expression would further increase the degrees of freedom, and thereby the accuracy that can be obtained. Hermitian expressions involving functions and their first, and higher derivatives have been suggested in the literature (*e.g.* [4], sections 2.4, 2.5). Peyret and Taylor ([17], section 2.5.1) and Hirsch ([18], section 4.3) discuss a symmetric version of equation 1 on a three point stencil. However, the development was not completed to a point where the resulting schemes could be used for solving partial differential equations.

The objective of this paper is to develop this family of schemes, and assess their potential for computations of the Navier Stokes equations. The schemes will be referred to as the 'coupled-derivative', or 'C-D' schemes to distinguish them from the standard Padé schemes. The paper is organized as follows. Section 2 describes the interior schemes that may be obtained from equation 1. Fourier analysis is then used in section 3 to perform a detailed comparison between the proposed schemes and the standard Padé schemes. The restrictions imposed by numerical (Cauchy) stability are then discussed in section 4. Section 5 presents appropriate boundary closures for the interior scheme, and evaluates the stability of the complete scheme. The computational cost of the proposed schemes is evaluated in section 6, and compared to that of the standard Padé schemes. The paper is concluded with a brief summary in section 7.

2. THE INTERIOR SCHEME

The interior scheme is of the form given by equation 1. Simultaneous solving for f_i' and f_i'', implies that the number of unknowns is equal to $2N$. A total of $2N$ equations are therefore needed to close the system. Equation 1 may be used to derive two linearly independent equations at each node. This is done as follows. Both sides of equation 1 are first expanded in a Taylor series. The resulting coefficients are then matched, such that equation 1 maintains a certain order of accuracy. Note that equation 1 has eleven coefficients, of which one is arbitrary, *i.e.*, equation 1 may be divided through by one of the constants, without loss of generality. A convenient choice of the normalizing constant, is either of a_0 or b_0. It will be seen that the equation obtained by setting a_0 equal to 1, is linearly independent of the equation obtained when b_0 is set equal to 1. The two equations may therefore be applied at each node, and the resulting system of $2N$ equations solved for the nodal values of the first and second derivative. The process of obtaining the two equations is outlined in sections 2.1 and 2.2.

	LHS	RHS
f_i	0	c_0
f_i'	$1+2a_1$	$2(2c_4+c_3)$
f_i''	b_0	0
f_i'''	$2h^2\left(a_1/2!+b_2\right)$	$2h^2\left(2^3\ c_4+c_3\right)/3!$
f_i^{iv}	0	0
f_i^{v}	$2h^4\left(a_1/4!+b_2/3!\right)$	$2h^4\left(2^5\ c_4+c_3\right)/5!$
f_i^{vi}	0	0
f_i^{vii}	$2h^6\left(a_1/6!+b_2/5!\right)$	$2h^6\left(2^7\ c_4+c_3\right)/7!$
f_i^{viii}	0	0
f_i^{ix}	$2h^8\left(a_1/8!+b_2/7!\right)$	$2h^8\left(2^9\ c_4+c_3\right)/9!$

TABLE 1: Taylor table for $a_0 = 1$.

2.1: First equation ($a_0 = 1$)

Consider first the case where $a_0 = 1$. The symmetry of the schemes requires that $a_1 = a_2$, $b_1 = -b_2$, $c_1 = -c_4$ and $c_2 = -c_3$. Equation 1 therefore reduces to the form:

$$a_1 f_{i-1}' + f_i' + a_1 f_{i+1}' + h(-b_2\ f_{i-1}'' + b_0 f_i'' + b_2 f_{i+1}'') = \frac{1}{h}\Big[c_0 f_i + c_3(f_{i+1} - f_{i-1}) + c_4(f_{i+2} - f_{i-2})\Big] \tag{4}$$

Expanding both sides of equation 4 in a Taylor series and collecting terms of the same order yields Table 1. Note that 'LHS' and 'RHS' denote the coefficients of f_i^k on the left and right-hand sides respectively of equation 4.

The Taylor table shows that $b_0 = c_0 = 0$. This leaves four undetermined constants $(a_1, b_2, c_3$ and $c_4)$. Expressions for these constants may be obtained by matching the terms in the Taylor table. Schemes of order ranging from two through eight may be obtained by solving the resulting set of equations. The coefficients and the resulting orders are listed below.

<u>*Second order*</u>

Matching terms up to f_i'' yields,

$$a_1 = -\frac{1}{2} + c_3 + 2c_4, \qquad b_2 \ \text{arbitrary.} \tag{5a}$$

The resulting leading order error is equal to $(3 - 12b_2 - 4c_3 + 4c_4)h^2 f_i'''/6$.

Fourth order

Matching terms up to f_i^{iv} yields,

$$a_1 = -\frac{1}{2} + c_3 + 2c_4, \qquad b_2 = \frac{1}{12}[3 - 4(c_3 - c_4)]. \tag{5b}$$

The resulting leading order error is given by$(-15 + 16c_3 + 92c_4)h^4 f_i^v/360$. Note that $c_4 = 0, \;\; c_3 = 3/4$ yields the standard fourth order Padé scheme for the first derivative.

Sixth order

Matching terms up to f_i^{vi} yields,

$$a_1 = \frac{7}{16} - \frac{15}{4}c_4, \qquad b_2 = \frac{1}{16}(-1 + 36c_4), \qquad c_3 = \frac{15}{16} - \frac{23}{4}c_4. \tag{5c}$$

The resulting leading order error is equal to $(1/5040 + 3c_4/140)h^6 f_i^{vii}$. Note that $c_4 = 1/36$ yields the standard sixth order Padé scheme for the first derivative.

Eighth order

Matching terms up to f_i^{viii} yields,

$$a_1 = \frac{17}{36}, \qquad b_2 = -\frac{1}{12}, \qquad c_3 = \frac{107}{108}, \qquad c_4 = -\frac{1}{108}. \tag{5d}$$

The error to leading order is equal to $-h^8 f_i^{ix}/90720$.

Table 1 shows that b_0 is equal to zero when a_0 is set equal to one. The above expressions may therefore be considered expressions for the nodal values of the first derivative. It also implies that if instead of setting a_0 equal to one, we set b_0 equal to one, we would obtain an equation that would be linearly independent. The equation thus derived could be considered an expression for the second derivative. This equation is obtained below.

2.2: Second equation ($b_0 = 1$)

Consider the case where $b_0 = 1$. Note that a tilde is used above the constants to indicate their difference from the constants obtained when $a_0 = 1$; *e.g.*, b_1 is replaced by $\widetilde{b}_1$. Symmetry requires that $\widetilde{b}_1 = \widetilde{b}_2$, $\widetilde{c}_1 = \widetilde{c}_4$, $\widetilde{c}_2 = \widetilde{c}_3$ and $\widetilde{a}_1 = -\widetilde{a}_2$. Equation 1 therefore becomes:

$$\widetilde{a}_0 f'_i + \widetilde{a}_2(f'_{i+1} - f'_{i-1}) + h(\widetilde{b}_1\, f''_{i-1} + f''_i + \widetilde{b}_1 f''_{i+1}) = \frac{1}{h}\left[\widetilde{c}_1(f_{i-2} + f_{i+2}) + \widetilde{c}_2(f_{i-1} + f_{i+1}) + \widetilde{c}_0 f_i\right] \tag{6}$$

Expanding both sides of the above equation in a Taylor series and collecting terms of the same order yields the Taylor table 2.

Table 2 shows that $\widetilde{a}_0$ is required to be zero if b_0 is equal to one. The resulting equation may therefore be considered an expression for the second derivative. We have five unknown constants ($\widetilde{c}_0, \widetilde{c}_1, \widetilde{c}_2, \widetilde{a}_2$ and $\widetilde{b}_1$). These constants may be obtained by matching the terms in the above Taylor table, and solving the resulting equations. Expressions of varying order

	LHS	RHS
f_i	0	$\tilde{c}_0 + 2\tilde{c}_1 + 2\tilde{c}_2$
f_i'	$\tilde{a}_0$	0
f_i''	$h(2\tilde{a}_2 + 2\tilde{b}_1 + 1)$	$2h\,(2^2\ \tilde{c}_1 + \tilde{c}_2)\,/2!$
f_i'''	0	0
f_i^{iv}	$2h^3(\tilde{a}_2/3! + \tilde{b}_1/2!)$	$2h^3\,(2^4\ \tilde{c}_1 + \tilde{c}_2)\,/4!$
f_i^{v}	0	0
f_i^{vi}	$2h^5(\tilde{a}_2/5! + \tilde{b}_1/4!)$	$2h^5\,(2^6\ \tilde{c}_1 + \tilde{c}_2)\,/6!$
f_i^{vii}	0	0
f_i^{viii}	$2h^7(\tilde{a}_2/7! + \tilde{b}_1/6!)$	$2h^7\,(2^8\ \tilde{c}_1 + \tilde{c}_2)\,/8!$
f_i^{ix}	0	0
f_i^{x}	$2h^9(\tilde{a}_2/9! + \tilde{b}_1/8!)$	$2h^9\,(2^{10}\ \tilde{c}_1 + \tilde{c}_2)\,/10!$

TABLE 2: Taylor table obtained for $b_0 = 1$.

are obtained, depending upon the number of equations matched. At first glance, it appears that the order of accuracy obtained, ranges from three through nine. By comparison, the expressions obtained when a_0 was equal to 1 ranged from second through eighth order. However, note that the nodal second derivatives in equation 1 are premultiplied by h. Equation 1 (and therefore the terms in the Taylor table) needs to be divided through by h, to consider it an expression for the second derivatives. This process will yield expressions for the second derivative, ranging in order from two through eight. The values for the constants and the corresponding orders are given below.

Second order

Matching terms up to f_i'' yields,

$$\tilde{c}_0 = -2(\tilde{c}_1 + \tilde{c}_2), \qquad \tilde{a}_2 = \frac{1}{2}(-1 - 2\tilde{b}_1 + 4\tilde{c}_1 + \tilde{c}_2). \tag{7a}$$

The resulting leading order error is $(2 - 8\tilde{b}_1 + 8\tilde{c}_1 - \tilde{c}_2)h^2 f_i^{iv}/12$.

Fourth order

Matching terms up to f_i^{iv} yields,

$$\tilde{c}_0 = -2(\tilde{c}_1 + \tilde{c}_2), \qquad \tilde{a}_2 = -\frac{3}{4} + \tilde{c}_1 + \frac{5}{8}\tilde{c}_2, \qquad \tilde{b}_1 = \frac{1}{4} + \tilde{c}_1 - \frac{\tilde{c}_2}{8}. \tag{7b}$$

The error to leading order, is given by $(-3+28\tilde{c}_1+\tilde{c}_2)h^4 f_i^{vi}/360$. Note that $\tilde{c}_1 = 0$, $\tilde{c}_2 = 6/5$ yields the standard fourth order Padé scheme for the second derivative.

Sixth order

Matching terms up to f_i^{vi} yields,

$$\tilde{c}_0 = -6 + 54\tilde{c}_1, \qquad \tilde{c}_2 = 3 - 28\tilde{c}_1, \qquad \tilde{a}_2 = \frac{9}{8} - \frac{33}{2}\tilde{c}_1, \qquad \tilde{b}_1 = -\frac{1}{8} + \frac{9}{2}\tilde{c}_1. \tag{7c}$$

The resulting error to leading order is $(1/20160 + 3\tilde{c}_1/560)h^6 f_i^{viii}$. Note that $\tilde{c}_1 = 3/44$ yields the standard sixth order Padé scheme for the second derivative.

Eighth order

Matching terms up to f_i^{viii} yields,

$$\tilde{c}_0 = -\frac{13}{2}, \qquad \tilde{c}_1 = -\frac{1}{108}, \qquad \tilde{c}_2 = \frac{88}{27}, \qquad \tilde{a}_2 = \frac{23}{18}, \qquad \tilde{b}_1 = -\frac{1}{6}. \tag{7d}$$

The resulting leading order error is $-h^8 f_i^{x}/453600$.

2.3: The scheme

The interior scheme involves applying the equations derived in sections 2.1 and 2.2 at each node. The resulting system of $2N$ equations is then solved to obtain f_i' and f_i''. Of the various schemes obtained, two schemes are discussed in detail below. These are the sixth order scheme with $c_1 = \tilde{c}_1 = 0$, and the eighth order schemes. These schemes have the same stencil width as the standard fourth and sixth order Padé schemes. A detailed comparison between these schemes and the standard Padé schemes is therefore performed. The appendix presents the schemes in matrix form, for completeness.

Sixth order C-D scheme ($c_1 = \tilde{c}_1 = 0$)

$$7f_{i-1}' + 16f_i' + 7f_{i+1}' + h(f_{i-1}'' - f_{i+1}'') = \frac{15}{h}(f_{i+1} - f_{i-1}). \tag{8a}$$

$$9(f_{i+1}' - f_{i-1}') - h(f_{i-1}'' - 8f_i'' + f_{i+1}'') = \frac{24}{h}(f_{i-1} - 2f_i + f_{i+1}). \tag{8b}$$

Eighth order C-D scheme

$$51f_{i-1}' + 108f_i' + 51f_{i+1}' + 9h(f_{i-1}'' - f_{i+1}'') = \frac{107}{h}(f_{i+1} - f_{i-1}) - \frac{f_{i+2} - f_{i-2}}{h}. \tag{9a}$$

$$138(f_{i+1}' - f_{i-1}') - h(18f_{i-1}'' - 108f_i'' + 18f_{i+1}'') = -\frac{f_{i+2} + f_{i-2}}{h} + \frac{352}{h}(f_{i+1} + f_{i-1}) - \frac{702}{h}f_i. \tag{9b}$$

Standard fourth order Padé

$$f_{i-1}' + 4f_i' + f_{i+1}' = \frac{3}{h}(f_{i+1} - f_{i-1}). \tag{10a}$$

$$f''_{i-1}+10f''_i+f''_{i+1}=\frac{12}{h^2}(f_{i-1}-2f_i+f_{i+1}). \tag{10b}$$

Standard sixth order Padé

$$f'_{i-1}+3f'_i+f'_{i+1}=\frac{7}{3h}(f_{i+1}-f_{i-1})+\frac{f_{i+2}-f_{i-2}}{12h}. \tag{11a}$$

$$2f''_{i-1}+11f''_i+2f''_{i+1}=\frac{12}{h^2}(f_{i-1}-2f_i+f_{i+1})+\frac{3}{4h^2}(f_{i-2}-2f_i+f_{i+2}). \tag{11b}$$

The expressions for the first and second derivative are seen to be independent in the standard Padé schemes (equations 10 and 11). Obtaining the first and second derivatives using the standard Padé schemes therefore involves separately inverting two tridiagonal matrices with band length of N. By comparison, the first and second derivatives are coupled in the C-D schemes. The vector of unknowns is therefore of length $2N$; $[....f'_{i-1},f''_{i-1},f'_i,f''_i,f'_{i+1},f''_{i+1}...]^T$. Note that for the same stencil width as the Padé schemes, the C-D schemes are two orders higher in accuracy. This is achieved at the cost of inverting a matrix that has seven bands instead of three. However, although the band width is increased from three to seven, the inversion yields both the first and second derivatives. A more systematic cost comparison with the Padé schemes is performed in section 6.

3. FOURIER ANALYSIS OF THE DIFFERENCING ERROR

Fourier analysis, and the notion of the 'modified wavenumber' provides a convenient means of quantifying the error associated with differencing schemes [2]. Consider the test function $f_j=e^{ikx_j}$ on a periodic domain. Discretize the function on a domain of length 2π, using a uniform mesh of N points. The mesh spacing is therefore given by $h=2\pi/N$. The exact values of the first and second derivative of f are ike^{ikx_j} and $-k^2e^{ikx_j}$. However, the numerically computed derivatives will be of the form, $ik'e^{ikx_j}$ and $-k''^2e^{ikx_j}$. The variables k' and k''^2 are functions of k and h, and are called the modified wavenumber for the first and second derivative operator respectively. The difference between k' and k, and k''^2 and k^2, provides the differencing error. The modified wavenumbers for the coupled-derivative schemes are derived and compared to the standard Padé schemes, in sections 3.1 and 3.2.

3.1: Modified wavenumber for the standard Padé schemes

The modified wavenumbers for the standard Padé schemes are given by Lele [1] as follows:

First derivative

$$k'h=\frac{a\sin kh+b/2\sin 2kh}{1+2\alpha\cos kh} \tag{12a}$$

where $\alpha=1/4$, $a=3/2$, and $b=0$ for the fourth order Padé scheme. For the sixth order Padé scheme, $\alpha=1/3$,$a=14/9$ and $b=1/9$.

Second derivative

$$k''^2h^2 = \frac{2a(1-\cos kh) + b/2(1-\cos 2kh)}{1+2\alpha\cos kh} \tag{12b}$$

where $\alpha = 1/10$,$a = 6/5$ and $b = 0$ for the fourth order Padé scheme. For the sixth order Padé scheme, $\alpha = 2/11$, $a = 12/11$, and $b = 3/11$.

3.2: Modified wavenumber for the C-D schemes

The modified wavenumbers for the C-D schemes are given below. As seen in sections 2.1 and 2.2, the sixth and eighth order schemes are members of the following two-equation family of schemes:

$$f'_i + a_1(f'_{i+1} + f'_{i-1}) + hb_2(f''_{i+1} - f''_{i-1}) = \frac{c_3}{h}(f_{i+1} - f_{i-1}) + \frac{c_4}{h}(f_{i+2} - f_{i-2}). \tag{13a}$$

$$\widetilde{a}_2(f'_{i+1} - f'_{i-1}) + h(\widetilde{b}_1 f''_{i-1} + f''_i + \widetilde{b}_1 f''_{i+1}) = \frac{\widetilde{c}_0}{h}f_i + \frac{\widetilde{c}_2}{h}(f_{i+1} + f_{i-1}) + \frac{\widetilde{c}_1}{h}(f_{i+2} + f_{i-2}). \tag{13b}$$

The constants in the above equations are as follows:

Sixth order scheme

$$c_4 = 0, \quad a_1 = 7/16, \quad b_2 = -1/16, \quad c_3 = 15/16$$

$$\widetilde{c}_1 = 0, \quad \widetilde{c}_2 = 3, \quad \widetilde{c}_0 = -6, \quad \widetilde{a}_2 = 9/8, \quad \widetilde{b}_1 = -1/8. \tag{14}$$

Eighth order scheme

$$c_4 = -1/108, \quad a_1 = 17/36, \quad b_2 = -1/12, \quad c_3 = 107/108$$

$$\widetilde{c}_1 = -1/108, \quad \widetilde{c}_2 = 88/27, \quad \widetilde{c}_0 = -13/2, \quad \widetilde{a}_2 = 23/18, \quad \widetilde{b}_1 = -1/6. \tag{15}$$

Equations 13a and 13b are used to obtain the modified wavenumbers as follows. Consider the function, $f_i = e^{ikx_i}$ on a periodic domain. Using the relations, $f'_{i\pm1} = f'_i e^{\pm ikh}$ and $f''_{i\pm1} = f''_i e^{\pm ikh}$, equations 13$a$ and 13b become,

$$f'_i(1 + 2a_1\cos kh) + f''_i(i2hb_2\sin kh) = i\frac{2f_i}{h}(c_3\sin kh + c_4\sin 2kh). \tag{16a}$$

$$f'_i(i2\widetilde{a}_2\sin kh) + f''_i(h + 2h\widetilde{b}_1\cos kh) = \frac{f_i}{h}(\widetilde{c}_0 + 2\widetilde{c}_2\cos kh + 2\widetilde{c}_1\cos 2kh). \tag{16b}$$

Equations 16a and 16b may be solved for f'_i and f''_i. The resulting expressions are of the form $ik'f_i$ and $-k''^2f_i$ where the modified wavenumbers (after some rearrangement) are given by the following expressions:

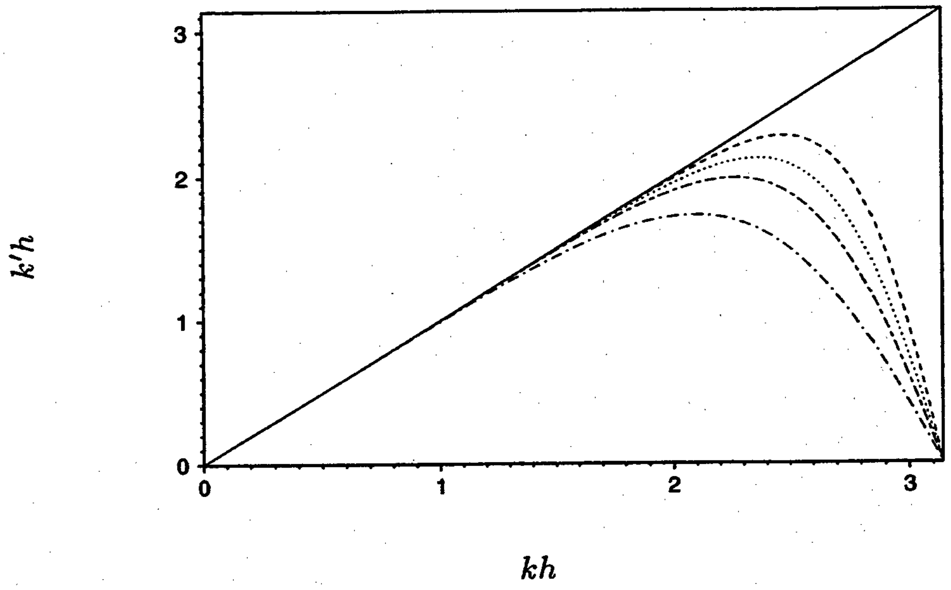

FIGURE 1 : The modified wavenumber for the first derivative. The C-D schemes are compared to the standard Padé schemes. ——— (Exact), ---- (C-D: eighth order), ········ (C-D: sixth order), —–— (Sixth order Padé), —·— (Fourth order Padé).

$$k'h = 2\sin kh \frac{c_3 + 2c_4\widetilde{b}_1 - \widetilde{c}_0 b_2 + 2(c_3\widetilde{b}_1 + c_4 - b_2\widetilde{c}_2)\cos kh + 2(c_4\widetilde{b}_1 - b_2\widetilde{c}_1)\cos 2kh}{1 + 2a_1\widetilde{b}_1 + 2\widetilde{a}_2 b_2 + 2(\widetilde{b}_1 + a_1)\cos kh + 2(a_1\widetilde{b}_1 - \widetilde{a}_2 b_2)\cos 2kh}. \tag{17a}$$

$$\begin{aligned} k''^2 h^2 = &- \frac{\widetilde{c}_0 + 2a_1\widetilde{c}_2 + 2\widetilde{a}_2 c_3 + 2(\widetilde{c}_2 + a_1\widetilde{c}_0 + 2\widetilde{a}_2 c_4)\cos kh}{1 + 2a_1\widetilde{b}_1 + 2\widetilde{a}_2 b_2 + 2(\widetilde{b}_1 + a_1)\cos kh + 2(a_1\widetilde{b}_1 - \widetilde{a}_2 b_2)\cos 2kh} \\ &- \frac{2(\widetilde{c}_1 + a_1\widetilde{c}_2 - \widetilde{a}_2 c_3)\cos 2kh + 4(a_1\widetilde{c}_1 - \widetilde{a}_2 c_4)\cos kh \cos 2kh}{1 + 2a_1\widetilde{b}_1 + 2\widetilde{a}_2 b_2 + 2(\widetilde{b}_1 + a_1)\cos kh + 2(a_1\widetilde{b}_1 - \widetilde{a}_2 b_2)\cos 2kh}. \end{aligned} \tag{17b}$$

3.3: Evaluation of first derivative

The modified wavenumbers for the first derivative are shown in figure 1. The C-D schemes are seen to follow the exact solution more closely than the standard Padé schemes. Recall that the sixth order C-D scheme has the same stencil width as the fourth order Padé, while the eighth order C-D scheme has the same stencil width as the sixth order Padé. In spite of its smaller stencil, the sixth order C-D scheme is seen to have lower error than the sixth order Padé. A more quantitative comparison of the schemes is provided in table 3. The fractional error in the first derivative may be defined as

$$\epsilon = \frac{|k'h - kh|}{kh}. \tag{18}$$

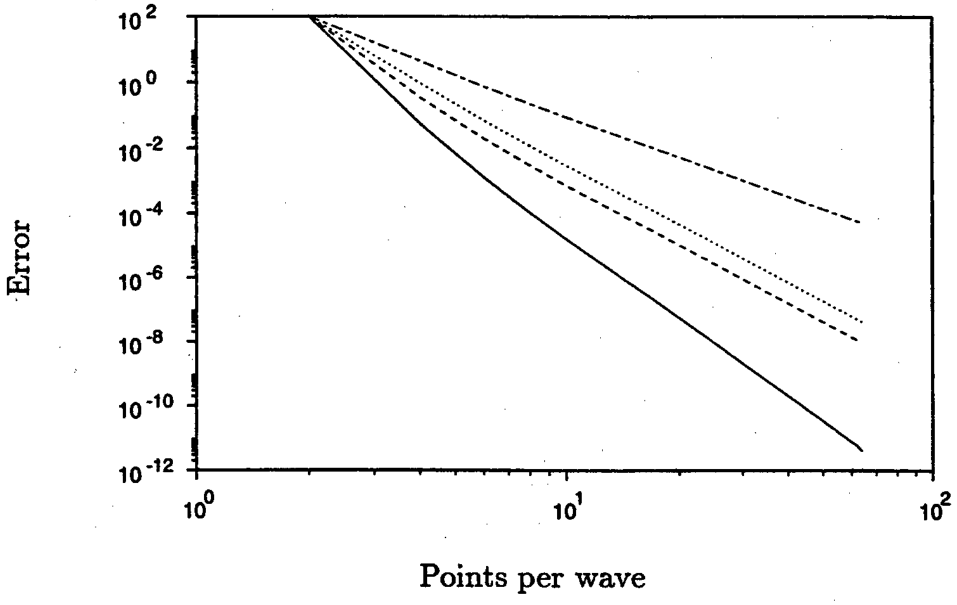

FIGURE 2: The percentage error in the first derivative as a function of the resolution. The C-D schemes are compared to the standard Padé schemes. ——— (C-D: eighth order), - - - - (C-D: sixth order), ········ (Sixth order Padé), — — — (Fourth order Padé).

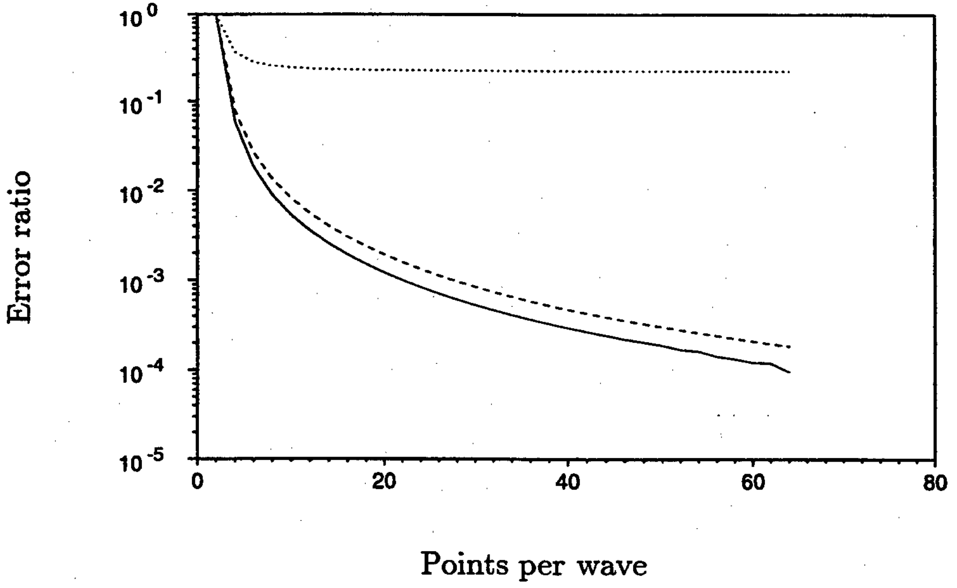

FIGURE 3: The ratio of the error in the first derivative between the C-D schemes and the standard Padé schemes as a function of the resolution. ——— (C-D 8 / Padé 6), - - - - (C-D 6 / Padé 4), ········ (C-D 6 / Padé 6).

	$\epsilon = 0.1$	$\epsilon = 0.01$	$\epsilon = 0.001$
Padé 4	0.59	0.35	0.20
Padé 6	0.70	0.50	0.35
C-D 6	0.75	0.58	0.42
C-D 8	0.81	0.66	0.53

TABLE 3: A comparison of the resolving efficiency of the C-D schemes to the Padé schemes.

	$N = 4$	$N = 8$
Padé 4	4.51 %	2.3×10^{-1} %
Padé 6	0.97 %	1.2×10^{-2} %
C-D 6	0.36 %	3.1×10^{-3} %
C-D 8	0.06 %	1.1×10^{-4} %

TABLE 4: The percentage error in the first derivative, as a function of the number of points per wave (N). The C-D schemes are compared to the standard Padé schemes.

Figure 1 shows that the error increases as kh increases. A measure of the accuracy or 'resolving ability' of the schemes is therefore provided, by specifying a maximum value for ϵ, and estimating the fraction of the entire range of wavenumbers for which this requirement is met. This quantity is termed 'resolving efficiency' by Lele [1], and is a function of the specified tolerance on the error. Table 3 compares the resolving efficiency of the C-D schemes to the standard Padé schemes. The C-D schemes are seen to be noticeably more accurate. In fact, of the different compact schemes considered by Lele, the only scheme that outperforms the eighth order C-D scheme is the pentadiagonal tenth order scheme (designated 'i' by Lele). The pentadiagonal scheme, however, has a stencil of five points on the left hand side, and 7 on the right.

The modified wavenumber may be used to determine the error as a function of the resolution. Consider the case where $k = 1$; *i.e.*, we have one wave of wavelength $\lambda = 2\pi$. The mesh spacing, h is given by $h = 2\pi/N = \lambda/N$. kh is therefore equal to λ/N, the reciprocal of the number of points per wavelength. The percentage error in the first derivative may be computed as a function of the resolution, using $kh = 2\pi/N$, and error$=$ $100|k'h - kh|/kh$. Figure 2 compares the C-D schemes to the standard Padé schemes. Note that all the schemes show 100% error for the two-delta waves (two points per wave). This is because the symmetry of the schemes forces $k'h$ to zero for two-delta waves. The C-D schemes are seen to have noticeably smaller error than the standard Padé schemes. Further indication of this is provided in figure 3, where the ratio of the error between the C-D schemes and the Padé schemes is shown. Table 4 documents the percentage error in the first derivative, for resolutions of 4 and 8 points per wave. The C-D schemes are seen

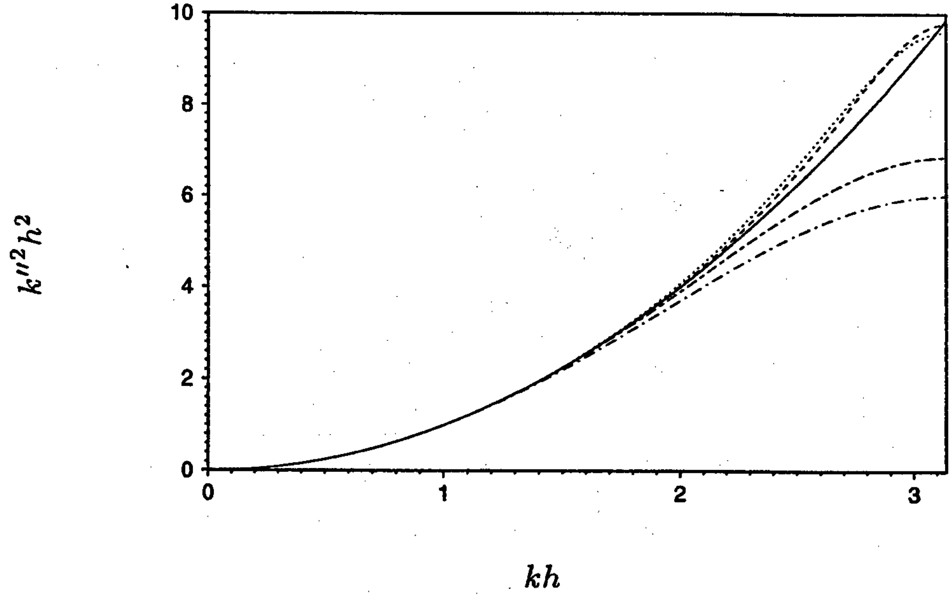

FIGURE 4: The modified wavenumber for the second derivative. The C-D schemes are compared to the standard Padé schemes. ——— (Exact), ---- (C-D: eighth order), ········ (C-D: sixth order), —–— (Sixth order Padé), —·— (Fourth order Padé).

to represent even four delta waves with an accuracy of 0.4% and 0.06%, respectively.

3.4: Evaluation of second derivative

Modified wavenumbers for the second derivative are shown in figure 4. The C-D schemes are seen to be noticeably more accurate at the higher wavenumbers. Interestingly, k''^2h^2 for the C-D schemes is greater than the exact solution for certain wavenumbers. This is in contrast to the standard Padé schemes, whose modified wavenumber is always less than the exact solution. However, this aspect of the C-D schemes does not impact the accuracy. As shown in figures 5 and 6, the C-D schemes are more accurate than the Padé schemes with the same stencil width.

Similar to the first derivative, a resolving efficiency may be defined for the second derivative, as the fraction of the wavenumber range for which the error,

$$\epsilon = \frac{|k''^2h^2 - k^2h^2|}{k^2h^2} \tag{19}$$

is less than a specified tolerance. The resolving efficiency is tabulated in table 5. Note that the requirement that ϵ be less than 0.1, is met over the entire range of wavenumbers. The second derivative computed using the sixth order C-D scheme is slightly more accurate than the sixth order Padé scheme, while the eighth order C-D scheme is noticeably more accurate than the standard Padé schemes. Table 6 shows the percentage error in the second derivative, as a function of the resolution. As was observed for the first derivative, the sixth and eighth order C-D schemes represent even four-delta waves, to an accuracy of about 0.4% and 0.1% respectively.

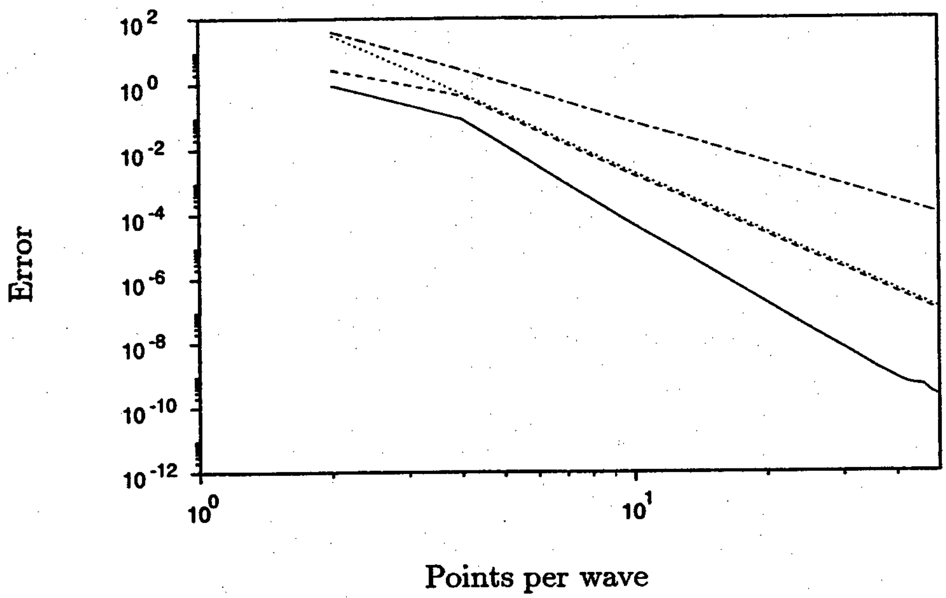

FIGURE 5: The percentage error in the second derivative as a function of the resolution. The C-D schemes are compared to the standard Padé schemes. ——— (C-D: eighth order), - - - - (C-D: sixth order), ········ (Sixth order Padé), — — — (Fourth order Padé).

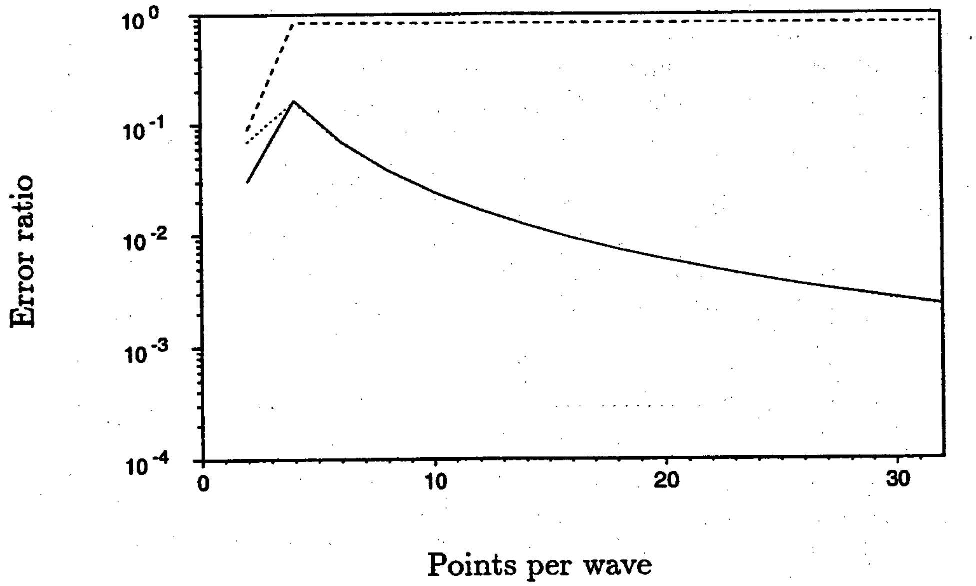

FIGURE 6: The ratio of the error in the second derivative between the C-D schemes and the standard Padé schemes as a function of the resolution. ——— (C-D 8 / Padé 6), - - - - (C-D 6 / Padé 6), ········ (C-D 6 / Padé 4).

	$\epsilon = 0.1$	$\epsilon = 0.01$	$\epsilon = 0.001$
Padé 4	0.68	0.39	0.22
Padé 6	0.80	0.55	0.38
C-D 6	1.00	0.57	0.39
C-D 8	1.00	0.67	0.50

TABLE 5: Comparison of resolving efficiency of the C-D schemes to the Padé schemes.

	$N = 4$	$N = 8$
Padé 4	2.73 %	1.6×10^{-1} %
Padé 6	0.52 %	7.41×10^{-3} %
C-D 6	0.44 %	6.16×10^{-3} %
C-D 8	0.09 %	2.84×10^{-4} %

TABLE 6: The percentage error in the second derivative, as a function of the number of points per wave (N). The C-D schemes are compared to the standard Padé schemes.

4. STABILITY LIMITS OF INTERIOR SCHEME

This section outlines the restrictions imposed by Cauchy stability on the time step, when the C-D schemes are used with Runge-Kutta time advancement. The model wave and diffusion equations are solved. Consider the one-dimensional wave equation on a periodic domain:

$$\frac{\partial u}{\partial t} + c\frac{\partial u}{\partial x} = 0. \tag{20}$$

The above equation is solved by the method of lines. Let $u = \widehat{u}e^{ikx}$. Spatial discretization leads to a set of ODEs of the form:

$$\frac{d\widehat{u}}{dt} = -i\frac{c}{h}\, k'h\widehat{u}. \tag{21}$$

The above equation is of the form $dy/dt = \lambda y$. It is easily shown that numerical stability requires that

$$\frac{c\Delta t}{h} \leq \frac{(\lambda_i \Delta t)_{\max}}{(k'h)_{\max}} \tag{22}$$

where $(k'h)_{\max}$ denotes the maximum value of the modified wavenumber for the first derivative, and $(\lambda_i \Delta t)_{\max}$ denotes the upper bound imposed by numerical stability, when the ODE $dy/dt = i\lambda_i y$ is numerically integrated. $(\lambda_i \Delta t)_{\max}$ has values of $0, \sqrt{3}$ and 2.85 when the standard second, third and fourth order Runge-Kutta schemes [19] are

	$RK2$	$RK3$	$RK4$
Padé 4	0	1.0	1.645
Padé 6	0	0.871	1.433
C-D 6	0	0.815	1.341
C-D 8	0	0.759	1.249
Fourier	0	0.551	0.907

TABLE 7: The maximum CFL number allowed by numerical stability.

	$RK2$	$RK3$	$RK4$
Padé 4	0.333	0.417	0.483
Padé 6	0.292	0.365	0.423
C-D 6	0.208	0.260	0.302
C-D 8	0.205	0.256	0.297
Fourier	0.203	0.253	0.294

TABLE 8: The maximum $\nu\Delta t/h^2$ allowed by numerical stability.

used for time advancement. Table 7 lists the corresponding bounds on the CFL number. As expected, the improved accuracy at the higher wavenumbers, reduces the maximum allowable CFL number.

Similarly, upper bounds on $\nu\Delta t/h^2$ can be obtained when the one-dimensional diffusion equation,

$$\frac{\partial u}{\partial t} = \nu \frac{\partial^2 u}{\partial x^2} \tag{23}$$

is numerically solved on a periodic spatial domain. Table 8 lists the obtained bounds, when the C-D schemes are used with Runge-Kutta time advancement. The accuracy of the C-D schemes for the two-delta waves ($kh = \pi$) results in the viscous restriction on the time step being nearly the same as that for a Fourier spectral method.

5. BOUNDARY SCHEMES

Consider a spatial domain that is discretized by using N points (including those at the boundaries). Equations 8 and 9 show that the sixth order scheme can be applied from $j = 2$ to $N - 1$, while the eighth order scheme can be applied from $j = 3$ to $N - 2$. For problems with periodic boundary conditions, the periodicity of the solution may be used to apply the same equations at the boundary nodes (see the appendix). However, for

	LHS	RHS
f_1	0	$c_1 + c_2 + c_3 + c_4$
f_1'	$a_0 + a_1$	$c_2 + 2c_3 + 3c_4$
f_1''	$h(a_1 + b_0 + b_1)$	$h\left(c_2 + 2^2\ c_3 + 3^2\ c_4\right)/2!$
f_1'''	$h^2(a_1/2! + b_1)$	$h^2\left(c_2 + 2^3\ c_3 + 3^3\ c_4\right)/3!$
f_1^{iv}	$h^3(a_1/3! + b_1/2!)$	$h^3\left(c_2 + 2^4\ c_3 + 3^4\ c_4\right)/4!$
f_1^{v}	$h^4(a_1/4! + b_1/3!)$	$h^4\left(c_2 + 2^5\ c_3 + 3^5\ c_4\right)/5!$
f_1^{vi}	$h^5(a_1/5! + b_1/4!)$	$h^5\left(c_2 + 2^6\ c_3 + 3^6\ c_4\right)/6!$

TABLE 9: Taylor table obtained for the boundary schemes.

non-periodic problems, additional expressions are needed at the boundary nodes to close the system.

Consider $j = 1$. The following general expression may be written for f_1' and f_1'':

$$a_0 f_1' + a_1 f_2' + h(b_0 f_1'' + b_1 f_2'') = \frac{1}{h}(c_1 f_1 + c_2 f_2 + c_3 f_3 + c_4 f_4). \tag{24}$$

The corresponding equation at $j = N$ would be given by:

$$a_0 f_N' + a_1 f_{N-1}' - h(b_0 f_N'' + b_1 f_{N-1}'') = -\frac{1}{h}(c_1 f_N + c_2 f_{N-1} + c_3 f_{N-2} + c_4 f_{N-3}). \tag{25}$$

The width of the stencil on the left hand side of the above equation is restricted to two. This ensures that the number of bands in the left-hand side matrix is still seven. As was done for the interior scheme, the constants in equation 24 may be obtained by expanding the terms in a Taylor's series, and matching expressions of the same order. Recall that we need two independent equations at each node. For the interior schemes, we saw that b_0 was equal to 0 if a_0 was equal to 1, and vice-versa. This yielded the two independent equations. As seen from tables 1 and 2, this relationship between a_0 and b_0 for the interior schemes is a natural consequence of their symmetry. However for the boundary schemes, it turns out that setting a_0 to 1 does not imply that b_0 is zero, and vice-versa. The equation obtained when $a_0 = 1$, is the same as that obtained when $b_0 = 1$. The following procedure is therefore used to obtain two independent equations. When matching the terms in the Taylor table, (a_0, b_0) is first set equal to $(1, 0)$. This yields the first equation. Next, (a_0, b_0) is set equal to $(0, 1)$. This yields the second equation. These expressions are derived below.

Taylor's series expansion of equation 24 yields table 9. There are eight undetermined constants in equation 1. Note that if either of the constraints $(a_0, b_0) = (1, 0)$ or $(0, 1)$ is imposed, and the terms in the Taylor table matched, the maximum order that can be obtained is five. The following family of schemes is obtained by matching the terms in Table 9 to different orders. Consider first the case where $a_0 = 1$, and $b_0 = 0$. The resulting expressions may be considered expressions for the first derivative.

5.1: First equation ($a_0 = 1, b_0 = 0$)

Expressions for the coefficients and the corresponding orders are given below.

Third order

Matching terms up to f_i''' yields,

$$c_1 = -3 + c_3 + 8c_4, \qquad c_2 = 3 - 2c_3 - 9c_4, \qquad a_1 = 2 - 6c_4, \qquad b_1 = -\frac{1}{2} + c_3 + 6c_4. \quad (26a)$$

The leading order error is then $(1/24 + c_3/12 + c_4)h^3 f_1^{iv}$. Note that $c_3 = 1/2, c_4 = 0$ yields the standard one-sided, third order compact scheme for the first derivative.

Fourth order

Matching terms up to f_i^{iv} yields,

$$c_1 = -\frac{7}{2} - 4c_4, \quad c_2 = 4 + 15c_4, \quad c_3 = -\frac{1}{2} - 12c_4, \quad a_1 = 2 - 6c_4, \quad b_1 = -1 - 6c_4. \quad (26b)$$

The error to leading order is given by $(-1/60 + c_4/5)h^4 f_1^v$. Note that $c_4 = -1/6$ yields the standard one-sided, fourth order compact scheme for the first derivative.

Fifth order

Matching terms up to f_i^v yields,

$$c_1 = -\frac{23}{6}, \quad c_2 = \frac{21}{4}, \quad c_3 = -\frac{3}{2}, \quad c_4 = \frac{1}{12}, \quad a_1 = \frac{3}{2}, \quad b_1 = -\frac{3}{2}. \qquad (26c)$$

The error to leading order is equal to $h^5 f_1^{vi}/120$.

5.2: Second equation ($a_0 = 0, b_0 = 1$)

Similar expressions are obtained when $a_0 = 0$, and $b_0 = 1$. These expressions may be considered relations for the second derivative. The order of the expressions will again range from three to five. However, due to the second derivatives being multiplied by h, the corresponding order of the second derivatives ranges from two to four. The values of the constants are given below.

Second order

Matching terms up to f_i''' yields,

$$c_1 = 6 + c_3 + 8c_4, \qquad c_2 = -6 - 2c_3 - 9c_4, \qquad a_1 = -6 - 6c_4, \qquad b_1 = 2 + c_3 + 6c_4. \quad (27a)$$

The error to leading order is given by $(-1/4 + c_3/12 + c_4)h^2 f_1^{iv}$.

Third order

Matching terms up to f_i^{iv} yields,

$$c_1 = 9-4c_4, \quad c_2 = -12+15c_4, \quad c_3 = 3-12c_4, \quad a_1 = -6-6c_4, \quad b_1 = 5-6c_4. \tag{27b}$$

The error to leading order is equal to $(7/60 + c_4/5)h^3 f_1^v$. Note that $c_4 = -1$ yields the standard one-sided third order compact scheme for the second derivative.

Fourth order

Matching terms up to f_i^v yields,

$$c_1 = 34/3, \quad c_2 = -83/4, \quad c_3 = 10, \quad c_4 = -7/12, \quad a_1 = -5/2, \quad b_1 = 17/2. \tag{27c}$$

The resulting leading order error is given by $-23h^4 f_1^{vi}/60$.

5.3: Numerical stability

The interior schemes outlined in section 2.3 are combined with the boundary schemes of sections 4.1 and 4.2, to close the system of equations for the first and second derivatives. Note that the sixth order interior scheme may be applied from $j = 2$ to $j = N-1$ and therefore only needs the boundary expressions at $j = 1$ and N. The eighth order interior scheme uses a five point stencil on the right-hand side. It therefore can only be applied from $j = 3$ to $N-2$. In this paper, if the eighth order scheme is used in the interior, the system of equations is closed by applying the sixth order scheme at $j = 2$ and $N-1$, and the boundary expressions at $j = 1$ and N. These expressions are derived below.

Note that the formal order of accuracy of the boundary schemes is less than the interior. This is due to the negative influence of high order (wide stencil) boundary closures on the stability of the overall scheme. Past work has shown that high order boundary closures can result in numerical instability in hyperbolic problems. For example, Carpenter *et al.* [20] compute solutions to the one-dimensional wave equation, and show that the standard fourth order Padé scheme (equation 10a) is asymptotically unstable when the one-sided fourth order expression,

$$f_1' + 3f_2' = \frac{1}{6h}(-17f_1 + 9f_2 + 9f_3 - f_4) \tag{28}$$

is used at the boundary nodes. The third order boundary expression,

$$f_1' + 2f_2' = \frac{1}{2h}(-5f_1 + 4f_2 + f_3) \tag{29}$$

is shown to be stable.

The combination of the boundary and interior schemes is numerically tested for hyperbolic stability in this section. The standard fourth order Runge-Kutta method is used for time advancement. The one-dimensional wave equation is numerically integrated to long times, and the solution is examined for boundedness (asymptotic stability). Also, the

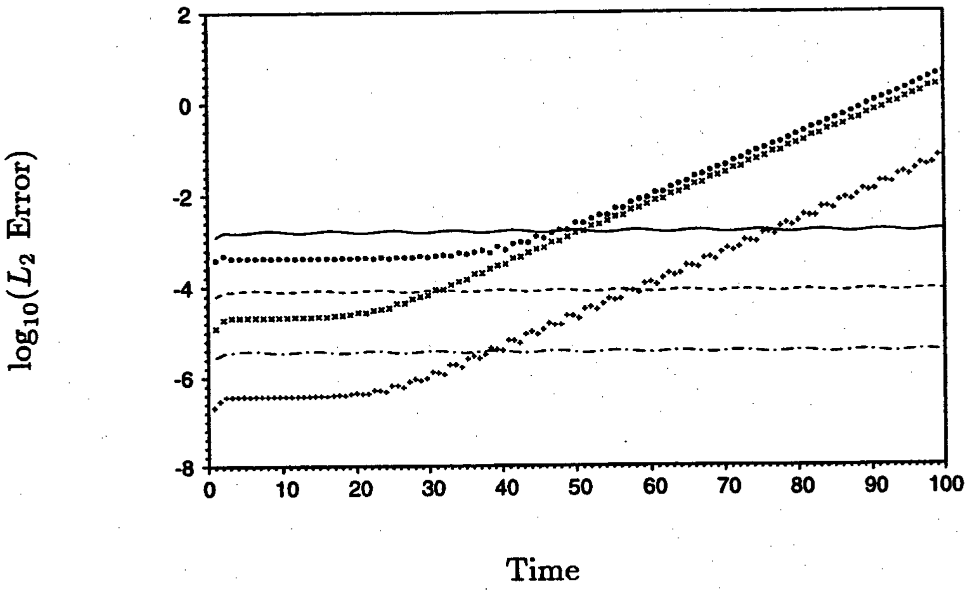

FIGURE 7: Illustration of the asymptotic instability of the sixth order C-D scheme with (4, 3) closure at the boundaries. The lines correspond to a CFL number of 1.33 while the symbols correspond to a CFL number of 0.1. ——— , • ($N = 26$), - - - - , × ($N = 51$), —·— , + ($N = 101$).

computational grid is refined while keeping the CFL number fixed, and convergence of the solution established (Lax stability). Details of this evaluation are provided below.

Consider the one-dimensional wave equation,

$$\frac{\partial u}{\partial t} + \frac{\partial u}{\partial x} = 0. \tag{30}$$

Equation 30 is numerically solved over the domain $-1 \leq x \leq 1$, subject to the following initial and boundary conditions,

$$u(x, 0) = \sin 2\pi x, \qquad u(-1, t) = \sin 2\pi(-1 - t). \tag{31}$$

Note that the exact solution to the above equation is given by

$$u_{\text{exact}}(x, t) = \sin 2\pi(x - t). \tag{32}$$

A uniform mesh is used for spatial discretization. The number of grid points (including the boundaries) is set equal to 26, 51 or 101. The solution is then integrated to a time $t = 100$. Note that the solution travels one wavelength in one time unit, and travels the length of the domain in two time units. The L_2 error defined as,

$$L_2 \ \text{ error} = \frac{1}{N}\sqrt{\sum_{j=1}^{N}(u_j - u_{\text{exact}})^2} \tag{33}$$

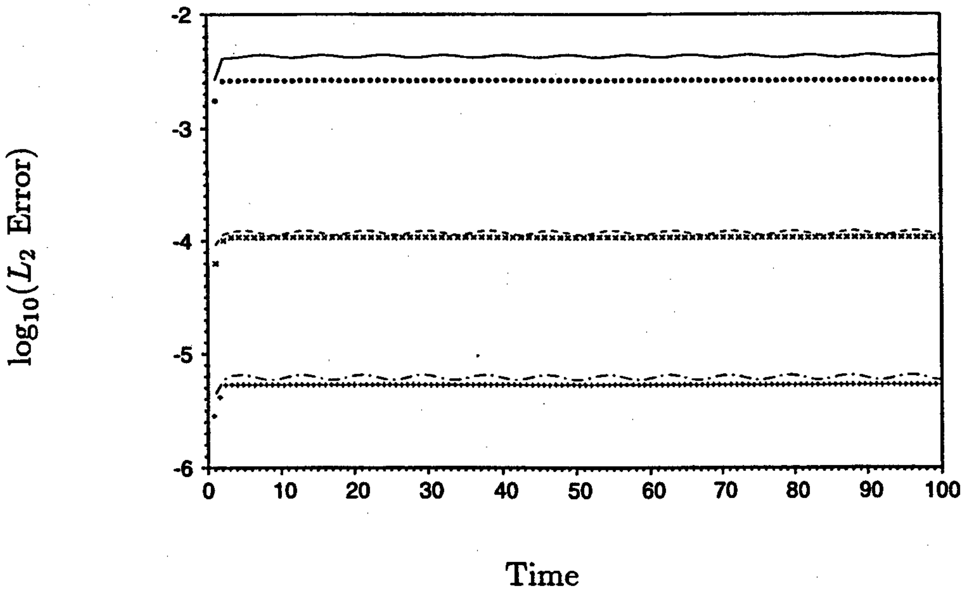

FIGURE 8: Illustration of the asymptotic stability of the sixth order C-D scheme with third order closure at the boundaries. The lines correspond to a CFL number of 1.33 while the symbols correspond to a CFL number of 0.1. ——— , • (N = 26), ---- , × (N = 51), —·— , + (N = 101).

is then examined for boundedness.

Several combinations of the boundary closures, and the interior scheme were examined. In the following discussion, the notation $[a, b-c-a, b]$ is used to denote these combinations. c denotes the order of the interior scheme, while a and b denote the order of the expressions for the first and second derivative at $j = 1$ and N. For example, the notation $[3, 3-6-3, 3]$ implies that the sixth order scheme (equation 8) is used in the interior, and the third order equations 26a and 27b are used at the boundary nodes. Note that if $c = 8$, it is implied that the eighth order scheme is applied from $j = 3$ to $N - 2$, and the sixth order scheme is applied at $j = 2$ and $N - 1$.

The numerical evaluations show that the stability is essentially dictated by the first derivative expression at the boundary. Schemes involving fourth and fifth order expressions for the first derivative, *i.e.*, the schemes $[4, 4-6-4, 4], [4, 3-6-4, 3], [4, 2-6-4, 2], [5, 4-6-5, 4], [5, 3-6-5, 3], [5, 2-6-5, 2]$ were found to be asymptotically unstable. Figure 7 illustrates the observed instability when the $[4, 4-6-4, 4]$ scheme *i.e*, fourth order boundary closure along with a sixth order interior scheme is used. Note that the L_2 error is bounded at a CFL number of 1.33 (the upper limit for stability of the interior scheme; see Table 7). However, the error is seen to grow exponentially at a smaller CFL number of 0.1. This behavior is similar to that observed by Carpenter *et al.* [20] when the standard fourth order Padé scheme (equation 10a) is used along with a fourth order boundary closure (equation 28). It is a result of the spatial discretization yielding a positive eigenvalue that lies within the stability envelope of the Runge-Kutta scheme at a CFL number of 1.33.

Similar tests showed that combinations of the third order expression for the first derivative (equation 26*a*) with second, third and fourth order expressions for the second derivative it i.e., the schemes $[3,2-c-3,2],[3,3-c-3,3],[3,4-c-3,4]$ were stable, for the sixth and eighth order interior schemes. Figure 8 illustrates the stability of the $[3,3-6-3,3]$ scheme.

5.4: Eigenvalue analysis

Section 5.3 used numerical solutions of the wave equation to identify the boundary closures that yielded stable solutions at long times. An eigenvalue analysis is conducted in this section to confirm that these boundary closures do indeed yield asymptotically stable solutions. Consider the wave equation,

$$\frac{\partial u}{\partial t}+c\frac{\partial u}{\partial x}=0 \tag{34}$$

subject to the inflow boundary condition, $u(0,t)=0^{\dagger}$. Discretize u on a uniform grid of N points (including the boundaries). The inflow condition implies that $u_1(t)=0$. Equation 34 is therefore solved for u_j, where j varies from 2 to N. Spatial discretization yields a set of ODEs of the form:

$$\frac{\mathrm{d}u_j}{\mathrm{dt}}=\frac{c}{h}M_{jk}f_k \tag{35}$$

where j and k vary from 2 to N. $\mathbf{M}$ is a $N-1$ by $N-1$ matrix, and is defined such that $u'_j=-M_{jk}u_k$. The eigenvalues of $\mathbf{M}$ determine the asymptotic stability of the system of ODEs. The requirement that the eigenvalues of $\mathbf{M}$ have negative real parts ensures asymptotic stability. The matrix $\mathbf{M}$ is obtained as follows. First, the condition $u_1=0$, the boundary expressions, and the interior scheme are used to eliminate u'_1 and u''_1 from the system of equations for the nodal derivatives. The resulting system of equations is then rearranged as follows. Recall that we use two independent equations relating u'_j and u''_j at each node. It is easily seen that these two equations may be expressed in the following form:

$$\mathbf{A}\ \mathbf{u}'+h\mathbf{B}\ \mathbf{u}''=\frac{1}{h}\mathbf{R}_1\ \mathbf{u}, \tag{36a}$$

$$\mathbf{C}\ \mathbf{u}'+h\mathbf{D}\ \mathbf{u}''=\frac{1}{h}\mathbf{R}_2\ \mathbf{u}. \tag{36b}$$

Note that the above system of equations is applied at the nodes $j=2$ to N. $\mathbf{u}''$ may be eliminated from the above system of equations to obtain an expression relating $\mathbf{u}'$ to $\mathbf{u}$. Premultiplying equations 36*a* and 36*b* by $\mathbf{B}^{-1}$ and $\mathbf{D}^{-1}$ respectively, and subtracting yields:

$$\left(\mathbf{B}^{-1}\mathbf{A}-\mathbf{D}^{-1}\mathbf{C}\right)\mathbf{u}'=\frac{1}{h}\left(\mathbf{B}^{-1}\mathbf{R}_1-\mathbf{D}^{-1}\mathbf{R}_2\right)\mathbf{u}, \tag{37}$$

---

† This simple inflow condition is adequate to determine the inherent stability of the system. A more general inflow condition, $u(0,t)=g(t)$ would simply yield a forcing term on the right-hand side of equation 35. The stability of the system would still be governed by the eigenvalues of $\mathbf{M}$.

implying that

$$\mathbf{f}' = -\frac{1}{h}\Big(\mathbf{B}^{-1}\mathbf{A} - \mathbf{D}^{-1}\mathbf{C}\Big)^{-1}\Big(\mathbf{B}^{-1}\mathbf{R_1} - \mathbf{D}^{-1}\mathbf{R_2}\Big)\mathbf{f}. \tag{38}$$

Comparison to the relation, $u_j' = -M_{jk}u_k$ yields the following expression for $\mathbf{M}$:

$$\mathbf{M} = \Big(\mathbf{B}^{-1}\mathbf{A} - \mathbf{D}^{-1}\mathbf{C}\Big)^{-1}\Big(\mathbf{B}^{-1}\mathbf{R_1} - \mathbf{D}^{-1}\mathbf{R_2}\Big). \tag{39}$$

The stability of the $(3,2), (3,3)$ and $(3,4)$ boundary closures (section 5.2) was tested for both sixth and eighth order interior schemes. The number of points N was set equal to 26, 51 or 101. The matrices $\mathbf{A}, \mathbf{B}, \mathbf{C}, \mathbf{D}, \mathbf{R_1}$ and $\mathbf{R_2}$ were specified, and equation 39 was used to (numerically) obtain $\mathbf{M}$. An eigenvalue solver from the IMSL library was then used to obtain the eigenvalues of $\mathbf{M}$. All three boundary closures were found to yield eigenvalues with negative real parts. Figures 9 and 10 illustrate the eigenvalues obtained when the $(3,3)$ closure was used with the sixth and eighth order interior schemes respectively.

5.5: The stable boundary closures

The stable boundary closures are summarized below. The following expressions are used at $j = 1$. Equation 25 may be used to obtain the corresponding expressions at $j = N$.

(3,4) boundary closure

The third order expression for the first derivative is combined with a fourth order expression for the second derivative.

$$f_1' + 2f_2' - \frac{h}{2}f_2'' = \frac{3}{h}(f_2 - f_1) \tag{40a}$$

$$-\frac{5}{2}f_2' + h(f_1'' + \frac{17}{2}f_2'') = \frac{1}{h}(\frac{34}{3}f_1 - \frac{83}{4}f_2 + 10f_3 - \frac{7}{12}f_4) \tag{40b}$$

(3,3) boundary closure

The third order expression for the first derivative is combined with a third order expression for the second derivative.

$$f_1' + 2f_2' - \frac{h}{2}f_2'' = \frac{3}{h}(f_2 - f_1) \tag{41a}$$

$$-6f_2' + h(f_1'' + 5f_2'') = \frac{3}{h}(3f_1 - 4f_2 + f_3) \tag{41b}$$

(3,2) boundary closure

The third order expression for the first derivative is combined with a second order expression for the second derivative.

$$f_1' + 2f_2' - \frac{h}{2}f_2'' = \frac{3}{h}(f_2 - f_1) \tag{42a}$$

$$-6f_2' + h(f_1'' + 2f_2'') = \frac{6}{h}(f_1 - f_2) \tag{42b}$$

The matrix form of the schemes obtained with the $(3,3)$ closure is provided in the appendix for completeness. The corresponding matrices for the $(3,2)$ and $(3,4)$ closures are easily obtained from equations 40 and 42.

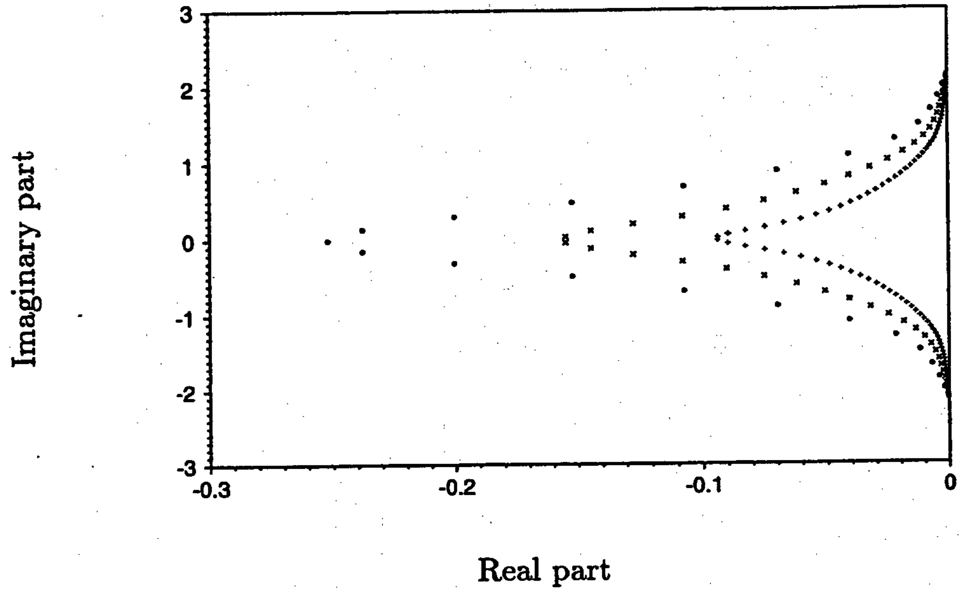

FIGURE 9: Eigenvalues obtained when the $(3,3)$ closure is used along with the sixth order interior scheme. ● ($N = 26$), × ($N = 51$), + ($N = 101$).

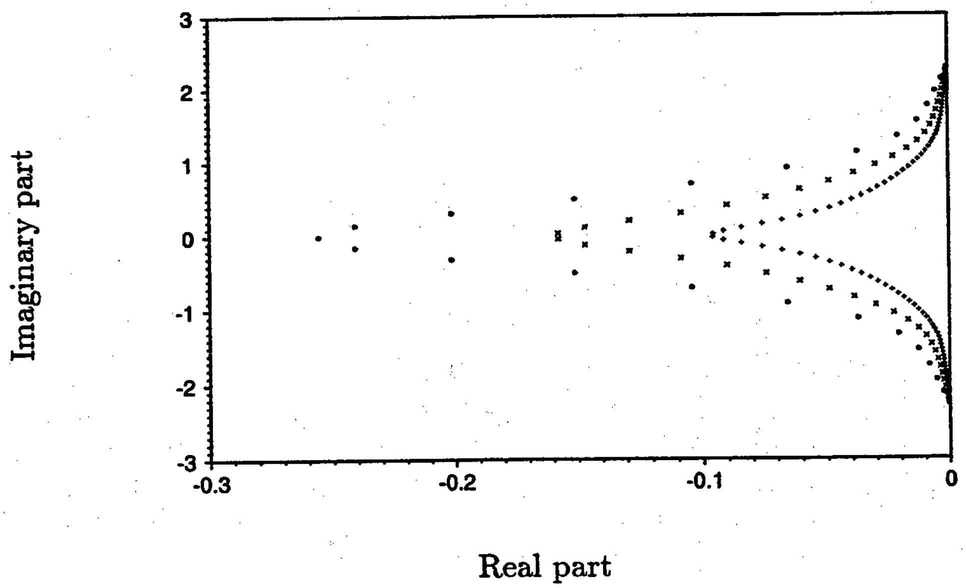

FIGURE 10: Eigenvalues obtained when the $(3,3)$ closure is used along with the eighth order interior scheme. ● ($N = 26$), × ($N = 51$), + ($N = 101$).

	RHS	*LU* solve	Total
Padé 4: first der.	$1+1+0=2$	$2+2+1=5$	$3+3+1=7$
Padé 4: second der.	$2+2+0=4$	$2+2+1=5$	$4+4+1=9$
Padé 6: first der.	$2+3+0=5$	$2+2+1=5$	$4+5+1=10$
Padé 6: second der.	$4+5+0=9$	$2+2+1=5$	$6+7+1=14$
Padé 4: both ders.	$3+3+0=6$	$4+4+2=10$	$7+7+2=16$
Padé 6: both ders.	$6+8+0=14$	$4+4+2=10$	$10+12+2=24$
C-D 6	$3+3+0=6$	$12+4+2=18$	$15+7+2=24$
C-D 8	$3+7+0=10$	$12+4+2=18$	$15+11+2=28$

TABLE 10: The operation count per node to compute the first and second derivative. The entries are of the form, 'number of multiplies + adds/subtracts + divides = total'. The overall cost is obtained by multiplying the entries by the total number of points, N.

6. COST COMPARISON

The computational cost of the C-D schemes is compared to that of the standard Padé schemes, in this section. The standard Padé schemes and the C-D schemes are both of the form,

$$\mathbf{A}\,\tilde{\mathbf{f}} = \mathbf{B}\,\mathbf{f} \tag{43}$$

where $\mathbf{f} = [\ldots f_{i-1}, f_i, f_{i+1}, \ldots]^T$, and $\mathbf{A}$ and $\mathbf{B}$ are constant matrices that depend on the scheme. For the standard Padé schemes, the vector $\tilde{\mathbf{f}}$ is of length N, and is either equal to $[\ldots f'_{i-1}, f'_i, f'_{i+1} \ldots]^T$, or $[\ldots f''_{i-1}, f''_i, f''_{i+1} \ldots]^T$. Also, the matrix $\mathbf{A}$ is tridiagonal with a band-length of N. For the C-D schemes, $\tilde{\mathbf{f}}$ is of length $2N$, and is equal to $[\ldots f'_{i-1}, f''_{i-1}, f'_i, f''_i, f'_{i+1}, f''_{i+1}, \ldots]^T$. The matrix $\mathbf{A}$ now has seven bands (see the appendix), each of length equal to $2N$.

At first glance, it might appear as if the C-D schemes would be significantly more expensive. However, this is not the case. Although the matrix bandwidth, and the solution vector length of the C-D schemes is twice that of the standard schemes, a single evaluation yields both first and second derivatives. When the cost of computing both derivatives is estimated, the C-D schemes are seen to incur essentially the same cost as the standard Padé schemes. This is illustrated below.

In using schemes of the form given by equation 43, the common practice is to perform *LU* decomposition of the matrix $\mathbf{A}$ only once, and store the L and U matrices. Computation of the derivatives therefore involves computing the right-hand side ($\mathbf{B}\ \mathbf{f}$), followed by forward and back substitution. The operation count associated with computing the right-hand side, and solving the resulting system of equations is tabulated in Table 10. When the cost of computing both derivatives is estimated, the C-D schemes are seen to

	LU decomposition	RHS	LU solve	$RHS + LU$ solve
Padé 4	2490	305	468	773
Padé 6	2480	328	470	798
C-D 6	3590	251	412	653
C-D 8	3830	264	424	688

TABLE 11: The time in microseconds to compute both first and second derivatives, on a mesh of 128 points. All computations use LAPACK routines for banded matrices on a CRAY C90 in scalar mode.

involve the same number of divides,† and add/subtracts as the standard Padé schemes with the same stencil width. The only increase in the number of operations involves the number of multiplies: the eighth order scheme has 1.5 times the number of multiplies as the sixth order Padé, while the sixth order scheme has twice the number of multiplies as the fourth order Padé. As shown below, this increase in the number of multiplies is not very significant. A cost evaluation was performed on a CRAY C90 in scalar mode, using LAPACK routines for the LU decomposition, and the solution of the LU decomposed system. The LAPACK routines took advantage of the banded structure of the coefficient matrix. The function $f = \sin(x)$ was discretized using a uniform mesh of 128 points on a domain of length equal to 2π. Individual routines computed the right-hand side, generated and LU decomposed the matrix A, and solved the system of equations. Each of these procedures was performed 1000 times, and the result was averaged to determine the cost per evaluation. The cost in microseconds is listed in Table 11. The C-D schemes are seen to incur essentially the same cost as the standard Padé schemes when the cost of computing both derivatives is considered.

7. CONCLUSION

A family of finite difference schemes for the first and second derivatives of smooth functions were derived. The schemes are Hermitian and symmetric, and may be considered an extension of the standard Padé schemes described in [1]. They are different from the standard Padé schemes, in that the first and second derivatives are simultaneously evaluated. Fourier analysis was used to compare the proposed schemes to the standard Padé schemes. For the same stencil width, the proposed schemes were shown to be two orders higher in accuracy, and have significantly better spectral representation. Numerical solutions to the one-dimensional wave equation, and eigenvalue analysis were used to demonstrate the numerical stability of the schemes. The computational cost of the proposed schemes was assessed, and the cost of computing both derivatives was shown to be essentially the same as the standard Padé schemes.

---

† The divides in the LU solve may be replaced by multiplies if desired, by storing the inverse of the coefficients of the L and U matrices.

Considering that the Navier Stokes equations require both first and second derivatives of most flow variables, the proposed schemes appear to be attractive alternatives to the standard Padé schemes for computations of the Navier Stokes equations.

ACKNOWLEDGEMENTS

This work was supported by the AFOSR under Contract F49620-92-J-0128 with Dr. Len Sakell as technical monitor. I am grateful to Prof. Parviz Moin for many useful discussions, and to Dr. Karim Shariff and Mr. Jon Freund for their comments on a draft of this manuscript.

APPENDIX

The schemes are presented in matrix form below. Both periodic and non-periodic boundaries are considered.

Sixth order scheme: periodic

The sixth order scheme on a periodic domain is given by:

$$\begin{bmatrix} 16 & 0 & 7 & -h & & & & 0 & 7 & h \\ 0 & 8h & 9 & -h & 0 & & & & -9 & -h \\ \ddots & \ddots & \ddots & \ddots & \ddots & \ddots & & & & \\ & 0 & 7 & h & 16 & 0 & 7 & -h & & \\ & & -9 & -h & 0 & 8h & 9 & -h & 0 & \\ & & & \ddots & \ddots & \ddots & \ddots & \ddots & \ddots & \ddots \\ 7 & -h & & & & 0 & 7 & h & 16 & 0 \\ 9 & -h & 0 & & & & -9 & -h & 0 & 8h \end{bmatrix} \begin{bmatrix} f'_1 \\ f''_1 \\ \vdots \\ f'_i \\ f''_i \\ \vdots \\ f'_N \\ f''_N \end{bmatrix} = \frac{1}{h} \begin{bmatrix} 15(f_2 - f_N) \\ 24(f_N - 2f_1 + f_2) \\ \vdots \\ 15(f_{i+1} - f_{i-1}) \\ 24(f_{i-1} - 2f_i + f_{i+1}) \\ \vdots \\ 15(f_1 - f_{N-1}) \\ 24(f_{N-1} - 2f_N + f_1) \end{bmatrix}.$$

Eighth order scheme: periodic

The eighth order scheme on a periodic domain is given by:

$$\begin{bmatrix} 108 & 0 & 51 & -9h & & & & 0 & 51 & 9h \\ 0 & 108h & 138 & -18h & 0 & & & & -138 & -18h \\ \ddots & \ddots & \ddots & \ddots & \ddots & \ddots & & & & \\ & 0 & 51 & 9h & 108 & 0 & 51 & -9h & & \\ & & -138 & -18h & 0 & 108h & 138 & -18h & 0 & \\ & & & \ddots & \ddots & \ddots & \ddots & \ddots & \ddots & \ddots \\ 51 & -9h & & & & 0 & 51 & 9h & 108 & 0 \\ 138 & -18h & 0 & & & & -138 & -18h & 0 & 108h \end{bmatrix} \begin{bmatrix} f'_1 \\ f''_1 \\ \vdots \\ f'_i \\ f''_i \\ \vdots \\ f'_N \\ f''_N \end{bmatrix}$$

$$
= \frac{1}{h}\begin{bmatrix}
107(f_2-f_N)-(f_3-f_{N-1}) \\
-(f_3+f_{N-1})+352(f_2+f_N)-702f_1 \\
\vdots \\
\\
107(f_{i+1}-f_{i-1})-(f_{i+2}-f_{i-2}) \\
-(f_{i+2}+f_{i-2})+352(f_{i+1}+f_{i-1})-702f_i \\
\vdots \\
\\
107(f_1-f_{N-1})-(f_2-f_{N-2}) \\
-(f_2+f_{N-2})+352(f_1+f_{N-1})-702f_N
\end{bmatrix}.
$$

Sixth order scheme: (3, 3) boundary closure

The domain is non-periodic. The sixth order interior scheme is used at the nodes $j = 2$ to $N-1$, and the third order boundary expressions (equation 41) are used at $j = 1$ and N. The resulting scheme is given by:

$$
\begin{bmatrix}
1 & 0 & 2 & -h/2 & & & & & & \\
0 & h & -6 & 5h & 0 & & & & & \\
\ddots & \ddots & \ddots & \ddots & \ddots & \ddots & & & & \\
\\
 & 0 & 7 & h & 16 & 0 & 7 & -h & & \\
 & & -9 & -h & 0 & 8h & 9 & -h & 0 & \\
 & & & \ddots & \ddots & \ddots & \ddots & \ddots & \ddots & \ddots \\
\\
 & & & & & 0 & 2 & h/2 & 1 & 0 \\
 & & & & & & -6 & -5h & 0 & -h
\end{bmatrix}
\begin{bmatrix}
f'_1 \\ f''_1 \\ \vdots \\ \\ f'_i \\ f''_i \\ \vdots \\ \\ f'_N \\ f''_N
\end{bmatrix}
= \frac{1}{h}
\begin{bmatrix}
3(f_2-f_1) \\
9f_1-12f_2+3f_3 \\
\vdots \\
\\
15(f_{i+1}-f_{i-1}) \\
24(f_{i-1}-2f_i+f_{i+1}) \\
\vdots \\
\\
3(f_N-f_{N-1}) \\
-9f_N+12f_{N-1}-3f_{N-2}
\end{bmatrix}.
$$

Eighth order scheme: (3, 3) boundary closure

The domain is non-periodic. The eighth order interior scheme is used at the nodes $j = 3$ to $N-2$. The sixth order interior scheme is used at $j = 2$ and $N-1$, and third order boundary expressions (equation 41) are used at $j = 1$ and N. The resulting scheme is given by:

$$\left[\begin{array}{cccccccccccccc}
1 & 0 & 2 & -h/2 & & & & & & & & & & \\
0 & h & -6 & 5h & 0 & & & & & & & & & \\
7 & h & 16 & 0 & 7 & -h & & & & & & & & \\
9 & -h & 0 & 8h & 9 & -h & 0 & & & & & & & \\
 & \ddots & \ddots & \ddots & \ddots & \ddots & \ddots & \ddots & & & & & & \\
 & & & 0 & 51 & 9h & 108 & 0 & 51 & -9h & & & & \\
 & & & & -138 & -18h & 0 & 108h & 138 & -18h & 0 & & & \\
 & & & & & \ddots & \ddots & \ddots & \ddots & \ddots & \ddots & \ddots & & \\
 & & & & & & & 0 & 7 & h & 16 & 0 & 7 & -h \\
 & & & & & & & & -9 & -h & 0 & 8h & 9 & -h \\
 & & & & & & & & & 0 & 2 & h/2 & 1 & 0 \\
 & & & & & & & & & & -6 & -5h & 0 & -h
\end{array}\right]
\left[\begin{array}{c}
f'_1 \\ f''_1 \\ f'_2 \\ f''_2 \\ \vdots \\ f'_i \\ f''_i \\ \vdots \\ f'_{N-1} \\ f''_{N-1} \\ f'_N \\ f''_N
\end{array}\right]$$

$$= \frac{1}{h}\left[\begin{array}{c}
3(f_2-f_1) \\
9f_1-12f_2+3f_3 \\
15(f_3-f_1) \\
24(f_1-2f_2+f_3) \\
\\
\\
107(f_{i+1}-f_{i-1})-(f_{i+2}-f_{i-2}) \\
-(f_{i+2}+f_{i-2})+352(f_{i+1}+f_{i-1})-702f_i \\
\\
\\
15(f_N-f_{N-2}) \\
24(f_{N-2}-2f_{N-1}+f_N) \\
3(f_N-f_{N-1}) \\
-9f_N+12f_{N-1}-3f_{N-2}
\end{array}\right].$$

The expressions provided in section 5.5 may be used to obtain the matrices corresponding to the (3,2) and (3,4) boundary closures.

REFERENCES

1. S.K. Lele, Compact finite difference schemes with spectral-like resolution, *J. Comp. Phys.*, **103**, 16-42 (1992).
2. R. Vichnevetsky and J.B. Bowles, *Fourier Analysis of Numerical Approximations of Hyperbolic Equations* (SIAM, Philadelphia, 1982).
3. A.G. Kravchenko and P. Moin, On the effect of numerical errors in large eddy simulations of turbulent flows, Center for Turbulence Research, Stanford University, CTR Manuscript 160, 1996, To appear in *J. Comp. Phys.*

4. L. Collatz, *The numerical treatment of differential equations*, (Springer-Verlag, New York, 1966).
5. Z. Kopal, *Numerical Analysis*, (Wiley, New York, 1961).
6. G. Strang, *Linear Algebra and its applications*, (Harcourt Brace Jovanovich, San Diego, 1988).
7. C.D. Pruett and T. Zang, Direct numerical simulation of laminar breakdown in high-speed, axisymmetric boundary layers, *Theor. Comp. Fluid Dyn.*, **3**, 345-367 (1992).
8. C.D. Pruett, T. Zang, C.-L. Chang and M.H. Carpenter, Spatial direct numerical simulation of high-speed, boundary layer flows - part I: algorithmic considerations and validation, *Theor. Comp. Fluid Dyn.*, **7**, 49-76 (1995).
9. C.D. Pruett and C.-L. Chang, Spatial direct numerical simulation of high-speed, boundary layer flows - part II: transition on a cone in Mach 8 flow, *Theor. Comp. Fluid Dyn.*, **7**, 397-424 (1995).
10. N.A. Adams and L. Kleiser, Subharmonic transition to turbulence in a flat plate boundary layer at Mach 4.5, *J. Fluid Mech.*, **317**, 301-335 (1996).
11. Y. Guo and N.A. Adams, Numerical investigation of supersonic turbulent boundary layers with high wall temperature, in *Proceedings, 1994 Summer Program*, Center for Turbulence Research, Stanford University (1994).
12. S. Lee, S.K. Lele and P. Moin, Direct numerical simulation of isotropic turbulence interacting with a weak shock wave, *J. Fluid Mech.*, **251**, 533-562 (1993).
13. K. Mahesh, S.K. Lele and P. Moin, The interaction of a shock wave with a turbulent shear flow, Thermosciences Division, Mech. Engrg., Stanford University, Report No. TF-69 (1996).
14. T. Colonius, P. Moin and S.K. Lele, Direct computation of aerodynamic sound, Thermosciences Division, Mech. Engrg., Stanford University, Report No. TF-65 (1995).
15. B.E. Mitchell, S.K. Lele and P. Moin, Direct computation of the sound generated by subsonic and supersonic axisymmetric jets, Thermosciences Division, Mech. Engrg., Stanford University, Report No. TF-66 (1995).
16. N.A. Adams and K. Shariff, A high-resolution hybrid compact-ENO scheme for shock-turbulence interaction problems, Center for Turbulence Research, Stanford University, CTR Manuscript 155, 1995.
17. R. Peyret and T.D. Taylor, *Computational methods for fluid flow* (Springer-Verlag, New York, 1983).
18. C. Hirsch, *Numerical computation of internal and external flows, Volume 1: Fundamentals of numerical discretization* (Wiley, 1988).
19. C.W. Gear, *Numerical initial value problems in ordinary differential equations* (Prentice -Hall, 1971).
20. M.H. Carpenter, D. Gottlieb and S. Abarbanel, Stable and accurate boundary treatments for compact, high-order finite-difference schemes, *Appl. Num. Math.*, **12**, 55-87 (1993).

PART 4

J. Fluid Mech. (1997), *vol.* 334, *pp.* 353–379

The influence of entropy fluctuations on the interaction of turbulence with a shock wave

By KRISHNAN MAHESH, SANJIVA K. LELE AND PARVIZ MOIN

Center for Turbulence Research, Stanford University, Stanford, CA 94305, USA

(Received 10 June 1996 and in revised form 14 October 1996)

Direct numerical simulation and inviscid linear analysis are used to study the interaction of a normal shock wave with an isotropic turbulent field of vorticity and entropy fluctuations. The role of the upstream entropy fluctuations is emphasized. The upstream correlation between the vorticity and entropy fluctuations is shown to strongly influence the evolution of the turbulence across the shock. Negative upstream correlation between u' and T' is seen to enhance the amplification of the turbulence kinetic energy, vorticity and thermodynamic fluctuations across the shock wave. Positive upstream correlation has a suppressing effect. An explanation based on the relative effects of bulk compression and baroclinic torque is proposed, and a scaling law is derived for the evolution of vorticity fluctuations across the shock. The validity of Morkovin's hypothesis across a shock wave is examined. Linear analysis is used to suggest that shock-front oscillation would invalidate the relation between u_{rms} and T_{rms}, as expressed by the hypothesis.

---

1. Introduction

The interaction of shock waves with turbulent boundary layers has received considerable attention over the past five decades. There have been several experimental studies (Green 1970; Fernholz & Finley 1981; Settles & Dodson 1994; Dolling 1993) of the flow in a compression corner, normal shock/boundary layer interaction and more recently, the interaction of shock waves with three-dimensional boundary layers. These experiments testify to the complex flow field associated with the interaction. Incidence of the shock wave is shown to strongly affect both the mean flow, and the turbulent fluctuations. The Reynolds stresses and temperature fluctuations in the boundary layer are seen to amplify across the shock wave. Significant unsteadiness of the shock wave is observed when the boundary layer separates. The motion of the shock wave seems to be correlated with the upstream pressure fluctuations. Also, high levels of wall- pressure fluctuations are observed in the vicinity of the shock.

The importance of bulk compression in the evolution of the turbulence across the shock was noted by Bradshaw (1974), Dussauge & Gaviglio (1981) and Debieve, Gouin & Gaviglio (1982). Anisotropy of the upstream turbulence was identified as a significant factor by Jacquin, Blin & Geffroy (1991) and Mahesh, Lele & Moin (1993). The role of upstream acoustic waves was studied by Mahesh *et al.* (1995). By comparison, the role of entropy fluctuations in shock wave/boundary layer interaction seems to be under-appreciated. For example, Smits & Muck (1987) suggest that the primary mechanism of turbulence amplification in compression-corner flow is inviscid bulk compression. The adverse pressure gradient, concave streamline curvature, and mean compression downstream of the corner are found to further enhance turbulence levels. Also, unsteadiness of the shock front is identified as becoming important across strong shocks.

No mention is made of the likely influence that upstream entropy fluctuations would have on the evolution of the turbulence. Morkovin's (1961) hypothesis,

$$\frac{\rho'}{\overline{\rho}} = -\frac{T'}{\overline{T}} = (\gamma - 1)M^2\frac{u'}{\overline{U}}, \tag{1.1}$$

suggests that in addition to being correlated, the intensity of the vortical field and entropy fluctuations in a constant-pressure boundary layer are of comparable magnitude. Experimental data (Bradshaw 1977) support the above hypothesis. Also, measurements (Fernholz & Finley 1981) show that $\rho_{rms}/\overline{\rho}$ in a constant-pressure boundary layer can have values as high as $5\% - 10\%$. This suggests that entropy fluctuations might play an important role in the shock wave/boundary layer interaction.

Past analytical work (Morkovin 1960; Chang 1957; Cuadra 1968) has examined the interaction of plane entropy waves with a shock. These studies emphasize the pressure field that is produced through the interaction. Morkovin's one-dimensional analysis shows that the pressure fluctuations generated behind a detached shock are quite intense, and may affect the transition of the boundary layer on the body. Cuadra's parametric study demonstrates that entropy fluctuations in shear flows can generate noise levels comparable to those generated by vortical fluctuations. Rapid distortion theory was used by Goldstein (1979) to examine the influence of upstream entropy fluctuations on turbulence passing through a wind-tunnel contraction. His analysis showed that the entropy fluctuations produced turbulence, whose magnitude increased more rapidly with contraction ratio than that of the upstream imposed turbulence. With the exception of Hesselink & Sturtevant's (1988) experiments, it appears that the interaction of a turbulent field of entropy fluctuations with a shock wave has not been examined. Also, Hesselink & Sturtevant were interested in the sonic boom problem. As a result, their study emphasized the evolution of the shock front, and restricted the shock strength to Mach 1.1.

This paper studies the interaction of a normal shock with a turbulent field of vorticity and entropy fluctuations. Direct numerical simulation (DNS) and inviscid linear analysis are used for this purpose. The focus is on the influence of the upstream entropy fluctuations. Shock waves of strength Mach 1.29 and Mach 1.8 are computed using DNS, while the linear analysis considers a range of Mach numbers from 1 to 3. The paper is organized as follows. A description of the problem is provided in §2. Some details of the DNS and linear analysis are also summarized. Section 3 discusses the results and provides an explanation for the role of entropy fluctuations. Also, a scaling law for the evolution of vorticity fluctuations across the shock is derived. The paper is then concluded with a brief summary in §4.

2. Description of the problem

Direct numerical simulation and linear analysis are used to study the interaction of a normal shock wave with turbulence. The turbulent velocity field upstream of the shock wave is isotropic, and the mean flow is uniform. Also, the upstream turbulence essentially comprises a vortical velocity field and entropic thermodynamic field. This composition is exactly enforced within the linear analysis, and is only approximately satisfied in the DNS. The upstream thermodynamic field in the DNS approximately

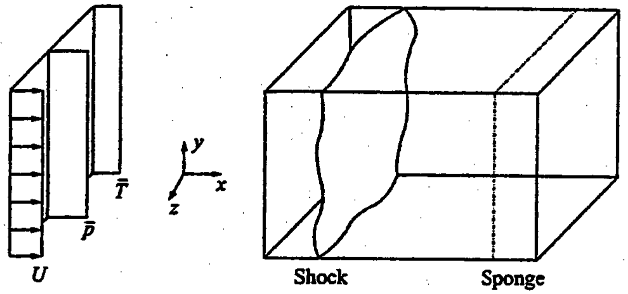

FIGURE 1. Schematic of the numerical simulation.

satisfies the weak form of Morkovin's hypothesis. The analysis considers two different spectra for the upstream thermodynamic field: one that satisfies the strong form of Morkovin's hypothesis (axisymmetric), and the other that is isotropic. Note that $\overline{u'T'}$ is negative if Morkovin's hypothesis holds upstream of the shock wave. For the isotropic upstream thermodynamic field, the analysis considers two possibilities: one where $\overline{u'T'}$ is negative, and the other where it is positive.

Section 2.1 outlines the relevant details of the DNS. The inflow and outflow boundary conditions are emphasized. A brief description of the linear analysis is then provided in §2.2.

2.1. *Details of the direct numerical simulation*

A schematic of the computed flow is shown in figure 1. Note that the shock wave is stationary in the mean. The governing equations are the unsteady three-dimensional compressible Navier–Stokes equations in the following conservative, non-dimensional form:

$$\frac{\partial \rho}{\partial t} = -\frac{\partial}{\partial x_i}(\rho u_i), \tag{2.1a}$$

$$\frac{\partial}{\partial t}(\rho u_i) = -\frac{\partial}{\partial x_j}(\rho u_i u_j + p\delta_{ij}) + \frac{\partial \tau_{ij}}{\partial x_j}, \tag{2.1b}$$

$$\frac{\partial E_t}{\partial t} = -\frac{\partial}{\partial x_i}[(E_t + p)u_i] - \frac{\partial q_i}{\partial x_i} + \frac{\partial}{\partial x_j}(u_i \tau_{ij}). \tag{2.1c}$$

The viscous stress tensor and heat flux vector are given by

$$\tau_{ij} = \frac{\mu}{Re}\left(\frac{\partial u_i}{\partial x_j} + \frac{\partial u_j}{\partial x_i} - \frac{2}{3}\frac{\partial u_k}{\partial x_k}\delta_{ij}\right), \tag{2.2a}$$

$$q_i = -\frac{\mu}{RePr}\frac{\partial T}{\partial x_i}. \tag{2.2b}$$

The variable E_t denotes the total energy, defined as $E_t = p/(\gamma-1) + \rho u_i u_i/2$. Note that the mean sound speed, density and dynamic viscosity at the inflow of the domain are used to non-dimensionalize velocity, density and viscosity respectively. The reference lengthscale L_r is related to the other reference variables by $Re = \rho_r c_r L_r/\mu_r$. The fluid is assumed to be an ideal gas with 1.4 as the ratio of specific heats. The dynamic viscosity is related to the temperature by a power law with 0.76 being the exponent, and the Prandtl number is assigned a constant value of 0.7.

The computational mesh is uniform in the directions transverse to the shock wave. A non-uniform mesh is used in the streamwise direction, such that points are clustered in the vicinity of the shock. The following analytical mapping is used for this purpose.

Using the variable s to denote a uniform mesh from 0 to 1_x, the non-uniform mesh is given by

$$\frac{x}{L_x} = \frac{rs + \dfrac{r-d}{2b}\ln\left[\dfrac{\cosh b(s-3c/2)\cosh bc/2}{\cosh b(s-c/2)\cosh 3bc/2}\right]}{r + \dfrac{r-d}{2b}\ln\left[\dfrac{\cosh b(1-3c/2)\cosh bc/2}{\cosh b(1-c/2)\cosh 3bc/2}\right]}. \tag{2.3}$$

Values of b, r, d and c used in the Mach 1.29 simulations are 12, 1.95, 0.04 and 0.281 respectively. The Mach 1.8 computation uses values of 12, 1.95, 0.02 and 0.283 respectively.

A combination of the sixth-order Padé scheme (Lele 1992) and the sixth-order ENO scheme (Shu & Osher 1988, 1989) is used to compute spatial derivatives. The shock-capturing scheme (ENO) uses the global Lax–Friedrichs flux splitting. The degeneracy in the base form of the ENO scheme is removed (Shu 1990) by biasing the adaptive choice of stencil towards central differences. Also, the shock-capturing scheme is applied only in the streamwise (shock-normal) direction in the vicinity of the shock wave. The sixth-order Padé scheme is therefore used to compute all spatial derivatives except the streamwise inviscid fluxes around the shock: the ENO scheme is used to compute those terms. Time advancement is performed using the compact-storage third-order Runge–Kutta scheme (Wray 1986). Since the turbulence is statistically homogeneous transverse to the shock wave, periodic boundary conditions are imposed in those directions. Turbulent fluctuations are superposed onto the mean field at the inflow boundary while non-reflecting boundary conditions are specified at the exit through use of a 'sponge' zone. Details of the inflow and outflow boundary conditions are provided below. The Mach 1.29 simulations are used for illustration; the same procedure was followed for the Mach 1.8 computation.

2.1.1. *Inflow turbulence*

Since the flow upstream of the shock wave is supersonic, all the flow variables are specified at the inflow boundary. Turbulent fluctuations in velocity, density and pressure are superposed on the uniform mean flow. The turbulence upstream of the shock wave is required to have an isotropic velocity field. When entropy fluctuations are present, the upstream velocity–temperature correlation is required to be similar to that found in adiabatic boundary layers, i.e. $R_{u'T'}$ is required to be nearly -1. The correlation between the velocity and temperature (entropy) fluctuations in turbulent boundary layers is a consequence of the turbulent velocity field stirring the mean temperature (entropy) gradients to produce temperature (entropy) fluctuations. However, due to the absence of a mean temperature gradient upstream of the shock in the computation, there is no mechanism to sustain a negative velocity–temperature correlation. This may be anticipated from the independence of the velocity and entropy fluctuations in the linear inviscid limit for uniform mean flow. The following procedure is therefore used to generate the desired upstream turbulence in the computations.

The turbulent fluctuations are obtained from a separate *temporal* simulation of isotropic, decaying turbulence. The temporal simulation (which has periodic boundary conditions in all three directions) is advanced in time until the flow field is well-developed, i.e. the velocity derivative skewness $S_\alpha = \overline{(\partial u'_\alpha/\partial x_\alpha)^3}/[\overline{(\partial u'_\alpha/\partial x_\alpha)^2}]^{3/2}$ attains (Tavoularis, Bennett & Corrsin 1978; Erlebacher *et al.* 1992) a value between -0.4 and -0.6. Typically, this happens after a time $t \sim \lambda/u_{rms}$. Taylor's hypothesis is then invoked, and a single realization of the developed field is convected through the inflow plane of the spatial simulation. Details of this procedure are described by Mahesh, Lele & Moin (1996). Note that Lee, Lele & Moin (1992) have shown the validity of Taylor's hypothesis in isotropic compressible turbulence for fluctuation Mach number $M_t = (q^2)^{1/2}/\bar{c}$, and turbulence intensity $u_{rms}/\overline{U}$ as high as 0.5 and 0.15 respectively. As shown in table 1, the turbulence at the inflow is within these limits.

The simulations with the shock wave compare two different cases at each Mach number. The two cases differ in the nature of the turbulence upstream of the shock wave. While the upstream turbulence in one case (case A) is composed of vortical fluctuations, a combination of vorticity and entropy fluctuations is present in the other (case B). The upstream entropy field in case B is required to approximately satisfy the weak form of Morkovin's hypothesis, i.e. (1.1) is satisfied in the r.m.s. sense. Also, the inflow spectra and r.m.s. levels of velocity in both cases are required to essentially be the same. The same temporal simulation is therefore used to generate the inflow turbulence in the two cases.

This is done as follows. A temporal simulation of isotropic turbulence is first conducted. The initial velocity field is solenoidal with energy spectrum $E(k) \sim k^4 \mathrm{e}^{-2k^2/k_0^2}$, and the initial thermodynamic fluctuations are set to zero. The simulation is advanced in time until the velocity derivative skewness attains its developed value. An instantaneous flow field is then taken. The thermodynamic fluctuations in this field are nearly isentropic. To generate a realistic turbulent field of vorticity and entropy fluctuations, the following procedure is carried out. The pressure fluctuations in the stored flow field are set to zero while density fluctuations that satisfy $\rho'/\bar{\rho} = (\gamma - 1)M_{spat}^2 u'/U_{spat}$ are specified† (the subscript *spat* denotes spatial). This modified field is then advanced in time. Statistics from the simulation are compared to a parallel simulation, where the same field without the above modifications is advanced for the same length of time.

As expected from Kovasznay's (1955) modal decomposition, the entropy fluctuations that are introduced do not significantly influence the evolution of the velocity fluctuations. After a brief acoustic transient ($t \sim M_t\lambda/u_{rms}$), the decay rate of turbulence kinetic energy, and the velocity derivative skewness match those in the simulation without entropy fluctuations. However as expected, the solution deviates from Morkovin's hypothesis as it evolves in time. To ensure that the weak formulation of the hypothesis is approximately satisfied by the turbulence upstream of the shock, an instantaneous realization is taken immediately after the acoustic transient, and used to specify inflow turbulence in case B. A realization at exactly the same instant of time is taken from the temporal simulation without entropy fluctuations and used to specify inflow turbulence in case A.

Figures 2 and 3 present results from the temporal simulation used to generate inflow turbulence in the Mach 1.29 simulations. Note that the solution at the end of the temporal simulation is used to generate the turbulence upstream of the shock wave. The initial temporal velocity field is chosen to have fluctuation Mach number $M_t = (q^2)^{1/2}/\bar{c} = 0.22$ and microscale Reynolds number $R_\lambda = u_{rms}\lambda/\bar{\nu} = 39.5$. A uniform mesh of 81^3 points is used on a domain of length 2π in all three directions. The solution is advanced for time $t = 1.58\tau_t$, where τ_t is a turbulence time scale defined as the ratio of λ to u_{rms} at $t = 0$. As shown in figure 2, the velocity derivative skewness has attained a value of -0.48 by this time. Also, M_t and R_λ have dropped to 0.16 and 22.8 respectively. Entropy fluctuations are then introduced, and the solution

---

† If these entropy fluctuations were specified at $t = 0$, $R_{u'T'}$ would drop to very small levels by the time the turbulence is well-developed.

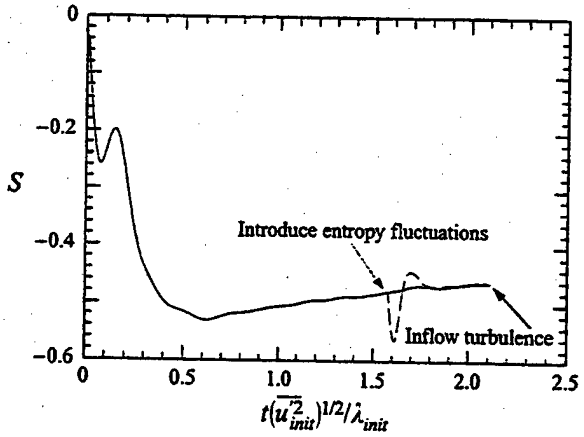

FIGURE 2. Temporal evolution of the velocity derivative skewness in the temporal decay of isotropic turbulence: ——, without entropy fluctuations; ----, with entropy fluctuations.

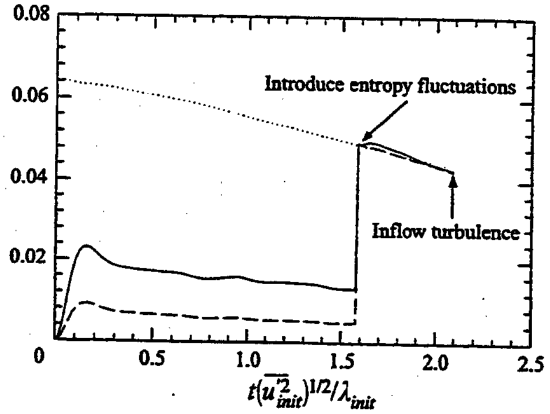

FIGURE 3. Temporal evolution of r.m.s values of terms in Morkovin's hypothesis in the temporal decay of isotropic turbulence: ——, $\rho_{rms}/\overline{\rho}$; ----, $T_{rms}/\overline{T}$; ·······, $[\gamma-1]M^2_{spat}u_{rms}/U_{spat}$.

is advanced in time. At the end of the simulation, the skewness has reattained its developed value (figure 2), and the weak form of the hypothesis is approximately satisfied; $\rho_{rms}/\overline{\rho}, T_{rms}/\overline{T}$ and $(\gamma-1)M^2_{spat}u_{rms}/U_{spat}$ have values of 0.043, 0.043 and 0.044 respectively. By comparison, $p_{rms}/\gamma\overline{p}$ is 0.01. Also, M_t, R_λ and $\theta_{rms}/\omega_{rms}$ have values of 0.14, 20.6 and 0.085 respectively (θ_{rms} and ω_{rms} denote the r.m.s. dilatation and vorticity respectively). The solution is therefore considered to be dominated by vorticity and entropy fluctuations that approximately satisfy the weak form of Morkovin's hypothesis.

The solution at the end of the calculations shown in figures 2 and 3 is used to specify inflow turbulence in the Mach 1.29 spatial simulations. The relevant parameters of the inflow turbulence are listed in table 1. The fidelity of the temporal simulations was checked by examining the energy spectra and two-point correlations of the fluctuations. One-dimensional spectra of the velocity field show very good agreement between the two cases, A and B. The spectra show about five decades of drop-off, indicating adequate resolution. Also, two-point correlations of the velocity and density field drop off to zero, indicating adequate size of computational domain.

2.1.2. *Outflow boundary conditions*

Approximately non-reflecting boundary conditions are specified at the subsonic outflow boundary. The boundary conditions comprise a 'sponge layer' in the streamwise direction, followed by a characteristics-based boundary condition (Poinsot & Lele 1992) at the outflow plane. Boundary conditions involving a sponge layer have been used in the past in a variety of problems: e.g. Israeli & Orszag (1981), Givoli (1991), Colonius, Moin & Lele (1995). The boundary conditions with a sponge were shown to yield significantly better results than boundary conditions without the sponge layer.

The governing equations in the 'sponge layer' are modified, such that the solution in the layer is gently damped to a reference solution. A term of the form $-\sigma(U-U_{ref})$ is added to the right-hand side of governing equations over the sponge layer alone. U_{ref} denotes the vector of reference variables towards which the solution in the sponge layer is forced. It is obtained from the Rankine–Hugoniot equations for a laminar shock. The coefficient $\sigma(x)$ is a polynomial function; i.e.

$$\sigma(x) = A_s \frac{(x-x_s)^n}{(L_x-x_s)^n} \qquad (2.4)$$

where x_s and L_x denote the start of the sponge and the length of the domain respectively. Values of A_s, n and $(L_x-x_s)/L_x$ used in our simulations are 5, 3 and 0.14 respectively.

The outflow boundary conditions are evaluated below. The interaction of the Mach 1.29 shock with a plane vorticity–entropy wave (45° incidence angle) is computed. Linear analysis predicts that the incident wave would generate downstream-propagating acoustic, vorticity and entropy waves behind the shock. The ability of the boundary conditions to allow these waves to smoothly exit the domain is thus tested. The mean flow parameters, domain length in the x-direction, and grid in the x-direction are matched to those in the turbulent simulation. The wavenumber of the upstream disturbance is set equal to the wavenumber at which the energy spectrum of the upstream turbulence peaks. The r.m.s. level of the upstream disturbance is matched to that of the upstream turbulence. The extent of the domain in y is set equal to one wavelength of the upstream disturbance, and a grid of 231 by 16 points is used to discretize the flow. The disturbance at the inflow boundary is given by the real part of (A 1*c*–*e*) (see the Appendix) where the variables k, ψ_1, A_v and A_e are set equal to 5, 45°, 0.05 and 0.05 respectively. The computation is initialized by a numerically computed steady laminar shock. The disturbance is then introduced at the inflow boundary. Statistics are gathered over each period of the inflow disturbance, after one domain flow-through time has passed. The statistics from successive periods are compared to check if initial transients persist. After a time $U_1t/L_x = 3.5$, the transient effects are found negligible and the statistics have converged.

To evaluate the outflow boundary conditions, the same flow is computed on a domain twice as long behind the shock wave. 1100 points are used in the streamwise direction. The resulting resolution is greater than that in the shorter domain. Statistics from the two simulations are then compared to each other and to linear analysis. Figure 4 shows the streamwise evolution of the averaged kinetic energy, vorticity and density in the two computations. Only the 'useful region' (L_x-x_s) of the shorter domain is shown. Good agreement between the two computations is observed, indicating that the non-reflecting nature of the sponge region is acceptable. Some influence of the sponge region (maximum value about 3.5%) on the statistics of $\overline{v'^2}$ and $\overline{\rho'^2}$ is observed immediately upstream of the sponge.

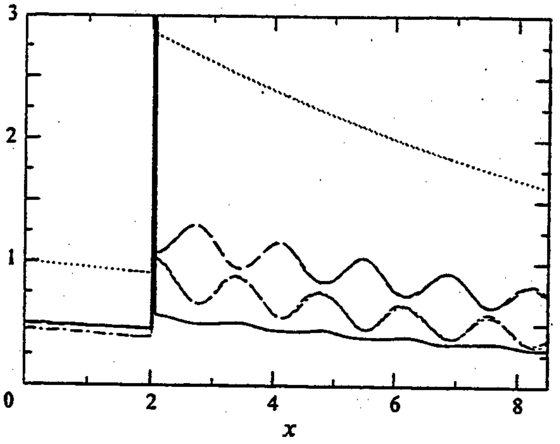

FIGURE 4. Spatial evolution of statistics from a computation of the interaction of a Mach 1.29 shock wave with a plane vorticity–entropy wave. Results from short and long domains are both indicated as follows: ——, $\overline{u'^2}/q_{in}^2$; ----, $\overline{v'^2}/q_{in}^2$; ·······, $\overline{\omega'^2}/\overline{\omega_{in}'^2}$; —-—, $(\overline{\rho'^2}/\overline{\rho_2}^2)/(q_{in}^2/U_1^2)$. The subscript *in* denotes inflow.

The spatial evolution of the statistics is not compared to inviscid linear analysis owing to significant viscous decay in the computation. However, the amplification of statistics immediately across the shock wave is compared to analysis. The comparison shows that the error (computed with respect to analysis) in $\overline{u'^2}, \overline{v'^2}, \overline{\omega'^2}$ and $\overline{\rho'^2}$ is 0.8%, 1.6%, 0.8% and 0.5% respectively. Linear analysis shows that only waves whose incidence angle is less than a critical incidence angle generate downstream-propagating disturbances behind the shock. Evanescent waves are generated at higher angles of incidence. In computing shock/turbulence interaction, the fraction of incident waves that generate these downstream-propagating disturbances poses the primary challenge to outflow boundary conditions. The performance of the outflow boundary for the incidence angle of 45° suggests that the boundary conditions are quite adequate for the turbulent simulations.

In evaluating the outflow boundary conditions, it was mentioned that the streamwise grid was the same as that used in the turbulent simulation. This streamwise grid is chosen as follows. The shock-capturing scheme is used to compute the corresponding steady laminar shock, and the solution is evaluated. The ENO schemes are known (Meadows, Caughy & Casper 1993; Woodward & Collela 1984; Roberts 1990; Lindquist & Giles 1991) to produce spurious entropy oscillations when applied to slowly moving shock waves. In contrast to standard central differences, these oscillations are bounded; they do not cause instability. The spurious oscillations in density and temperature are typically the largest, those in velocity and pressure are much smaller. To compute shock/turbulence interaction, we require that the amplitude of these spurious oscillations be small compared to the physical fluctuations. The amplitude of these spurious oscillations can be reduced by increasing the shock speed relative to the mesh (Meadows *et al.* 1993), or by refining the mesh (for a viscous computation). The shock is stationary in the mean in our computations. The shock speed with respect to the grid is therefore determined entirely by the upstream disturbances. We therefore use the shock-capturing scheme to compute the corresponding laminar shock, and refine the mesh until the spurious oscillations are acceptably small. For example, the mesh used in our Mach 1.29 computations yields spurious density oscillations that are 0.03% of the mean density behind the Mach 1.29 shock (the spurious oscillations in temperature, velocity and pressure are smaller). Table 1 shows that the upstream intensity of density fluctuations in the turbulent simulations is greater than 1.2%. The above level of spurious oscillations generated by the shock-capturing scheme is therefore considered acceptable. This streamwise grid is then used to perform the computations.

2.1.3. *Simulations performed*

The relevant parameters of the numerical simulations are given in table 1. Note that the values at the inflow are quoted. Essentially, the simulations consider the interaction of low-Reynolds-number turbulence with shock waves of strengths equal to Mach 1.29 and Mach 1.8. Note that one of the cases (free-stream Mach number 2.9, wedge angle 8°) in the compression-corner experiments of Smits & Muck (1987) yields a normal Mach number of 1.29 if one assumes that the entire flow is turned across a single shock. Also, only one simulation (with upstream entropy fluctuations) is performed for the Mach 1.8 shock. In §2.1 it was noted that the shock-capturing scheme was only applied in the streamwise direction for the Mach 1.29 shock wave. However, applying the shock-capturing scheme in only the streamwise direction set up unstable oscillations for the Mach 1.8 shock. As a result, the shock-capturing scheme was applied in all three directions in the immediate vicinity of the shock for the Mach 1.8 shock wave.

2.2. *Linear analysis*

Details of the linear analysis are provided in the Appendix. Essentially, the linearized Euler equations are used to study the interaction between the upstream turbulence and the shock wave, which is modelled as a discontinuity. The upstream turbulence (being homogeneous) is represented as a superposition of Fourier modes (plane waves), each of which independently interacts with the shock. The analysis is therefore initiated by considering the interaction of a single plane wave with the shock. Workers such as Ribner (1953, 1954) and Chang (1957) have developed the procedure to obtain the disturbance field behind the shock and the distortion of the shock front. Other references to work using linear analysis are provided by Mahesh *et al.* (1995). This solution is then integrated over all the incident waves to obtain a statistical description of the turbulence behind the shock wave. The turbulence statistics thus obtained are functions of the distance behind the shock wave, the Mach number of the shock, and the incident velocity and density spectra. In presenting results from the linear analysis, this paper will occasionally refer to the variables A_r and ϕ_r. Essentially, A_r represents the amplitude of the upstream density field, and ϕ_r represents the sign of the upstream velocity–temperature correlation. If $\phi_r = 0$, $\overline{u'T'}$ is negative upstream of the shock wave; $\phi_r = 180°$ implies that $\overline{u'T'}$ is positive upstream of the shock.

3. Results

Turbulence statistics in the simulation are computed by averaging over time and the y- and z-directions. The ratios of mean velocity, temperature and pressure across the shock wave are very nearly equal to their corresponding laminar values (Mahesh *et al.* 1996). A small overshoot in pressure and temperature is observed immediately downstream of the shock. The mean velocity exhibits a corresponding

	Case 1.29A	Case 1.29B	Case 1.8
M_1	1.29	1.29	1.8
R_λ	19.1	19.1	19.5
M_t	0.14	0.14	0.18
$(q^2)^{1/2}/\overline{U_1}$	0.11	0.11	0.10
$\rho_{rms}/\overline{\rho_1}$	0.012	0.042	0.076
$T_{rms}/\overline{T_1}$	0.0042	0.041	0.076
$p_{rms}/\gamma\overline{p_1}$	0.011	0.010	0.018
$\overline{u'T'}/u_{rms}T_{rms}$	−0.06	−0.84	−0.85
(N_x, N_y, N_z)	(231, 81, 81)	(231, 81, 81)	(231, 81, 81)

TABLE 1. Parameters in the simulations performed.

undershoot, following which it remains practically constant. However, mean pressure and temperature exhibit a small positive gradient behind the shock wave. The presence of upstream entropy fluctuations has no noticeable effect on the mean flow behind the shock. Entropy fluctuations do however influence the thickness of the shock wave as inferred from the mean flow profiles. The 'mean shock thickness' is larger in the presence of entropy fluctuations; i.e. the mean gradients in the vicinity of the shock are smaller. Given that the 'mean shock thickness' reflects the amplitude of shock oscillation, this indicates an increase in shock motion when the upstream fluctuations satisfy Morkovin's hypothesis.

The following sections present results for the evolution of the turbulence across the shock. The results from the DNS and linear analysis are compared. In §3.1 the evolution of the turbulence kinetic energy across the shock are discussed. The influence of the shock on the vorticity fluctuations is considered in §3.2. This is followed in §3.3 by a physical argument for the role of the upstream entropy fluctuations. In §3.4 a scaling for the amount of vorticity produced by the upstream entropy fluctuations is derived. Then in §3.5 the evolution of the thermodynamic fluctuations and the validity of Morkovin's hypothesis across the shock are discussed.

3.1. *Turbulence kinetic energy*

The presence of upstream entropy fluctuations has a noticeable effect on the evolution of turbulence kinetic energy across the shock wave. Figures 5 and 6 show the streamwise evolution of turbulence kinetic energy in cases 1.29A and 1.29B. Note that $\overline{v'^2} = \overline{w'^2}$ behind the shock. The intermittency associated with shock oscillation is seen to cause high fluctuation levels in the vicinity of the shock (Debiève & Lacharme 1986; Lee *et al.* 1992). The width of this intermittent region (denoted by δ_{inter}) nearly equals the 'mean shock thickness'. Using the mean velocity profile to determine its value, $k_0\delta_{inter}$ is approximately 0.3 and 0.4 in cases 1.29A and 1.29B respectively† . We focus our attention on the evolution of kinetic energy outside this intermittent region in the following paragraphs.

As shown in figure 6, kinetic energy levels behind the shock wave are noticeably higher in case 1.29B. The streamwise component is affected more than the transverse components. Comparison of the peak in the profile of $\overline{u'^2}$ (at $k_0x = 14$) reveals 20% higher levels in case 1.29B. Comparison of $\overline{v'^2}$ at the same location shows

† The smallest mesh spacing is in the vicinity of the shock, and is equal to $0.02/k_0$ in both simulations. Also, the shock-capturing scheme is applied over a width equal to $1.8/k_0$ on either side of the mean shock.

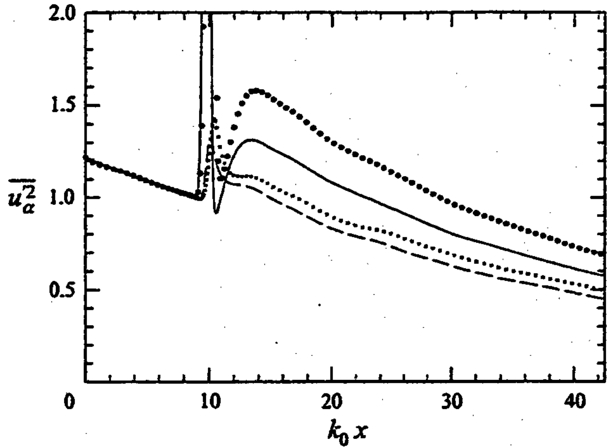

FIGURE 5. Turbulence kinetic energy from DNS of the Mach 1.29 shock wave. All the curves are normalized by their value immediately upstream of the shock ($k_0 x = 8.97$): ——, $\overline{u'^2}$, case 1.29A; ----, $\overline{v'^2}$, case 1.29A; •, $\overline{u'^2}$, case 1.29B; ×, $\overline{v'^2}$, case 1.29B.

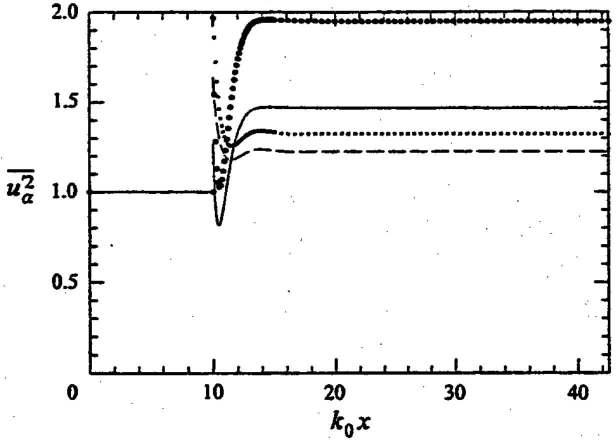

FIGURE 6. Evolution of turbulence kinetic energy behind a Mach 1.29 shock wave as predicted by linear analysis. All the curves are normalized by their value immediately upstream of the shock: ——, $\overline{u'^2}$, without entropy fluctuations; ----, $\overline{v'^2}$, without entropy fluctuations; •, $\overline{u'^2}$, with entropy fluctuations; ×, $\overline{v'^2}$, with entropy fluctuations.

the level of enhancement to be a modest 7%. This enhancement in the presence of entropy fluctuations is predicted by linear analysis. Note that quantitative comparison of turbulence kinetic energy between analysis and DNS is made difficult by the viscous decay in the simulations. If the peak levels of kinetic energy behind the shock wave are compared, the linear analysis predictions are seen to be higher. As seen from figure 6, the amplification of $\overline{u'^2}$ as predicted by linear analysis is 1.47 and 1.95 in the absence and presence of entropy fluctuations (that satisfy Morkovin's hypothesis) respectively. Corresponding values for $\overline{v'^2}$ are predicted to be 1.22 and 1.32 respectively. Thus linear analysis predicts that the upstream entropy fluctuations would enhance the amplification of $\overline{u'^2}$ by 33%, and that of $\overline{v'^2}$ by about 8%.

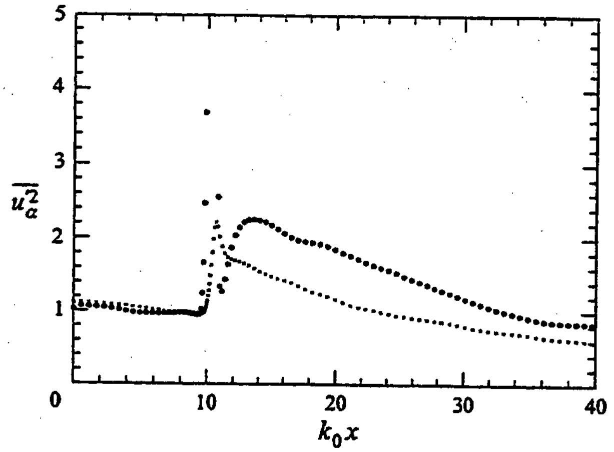

FIGURE 7. Turbulence kinetic energy from DNS of the Mach 1.8 shock wave. Both the curves are normalized by their value immediately upstream of the shock. •, $\overline{u'^2}$; ×, $\overline{v'^2}$.

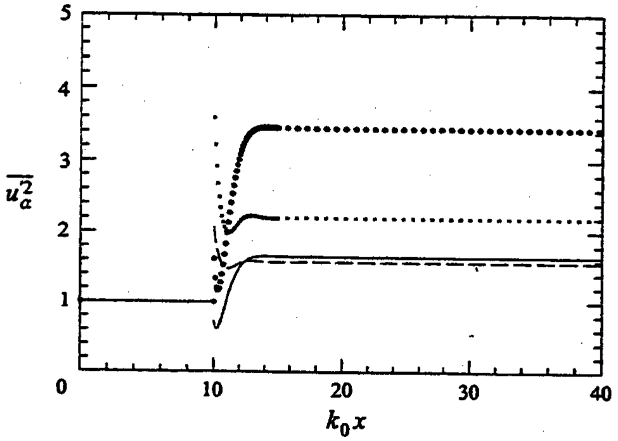

FIGURE 8. Evolution of turbulence kinetic energy behind a Mach 1.8 shock wave as predicted by linear analysis. All the curves are normalized by their value immediately upstream of the shock: ——, $\overline{u'^2}$, without entropy fluctuations; ----, $\overline{v'^2}$, without entropy fluctuations; •, $\overline{u'^2}$, with entropy fluctuations; ×, $\overline{v'^2}$, with entropy fluctuations.

Figures 7 and 8 show the evolution of turbulence kinetic energy across the Mach 1.8 shock wave. The amplification levels are noticeably higher than those across the Mach 1.29 shock. Using values measured at $k_0x = 13.4$ (the location behind the shock where $\overline{u'^2}$ is maximum) $\overline{u'^2}$ and $\overline{v'^2}$ are seen to amplify by 2.25 and 1.61 respectively. These levels are lower than predicted by linear analysis, where Morkovin's hypothesis is assumed to exactly hold upstream of the shock. The predicted (far-field) values of kinetic energy amplification are 3.44 and 2.2 respectively. Linear analysis predicts that the upstream entropy fluctuations would enhance the amplification of $\overline{u'^2}$ and $\overline{v'^2}$ by 110% and 40% respectively across a Mach 1.8 shock.

Note that $\overline{u'T'}$ is negative if Morkovin's hypothesis is valid. Linear analysis shows that the sign of the correlation between the upstream velocity and entropy fields is of considerable importance. If the upstream correlation between u' and

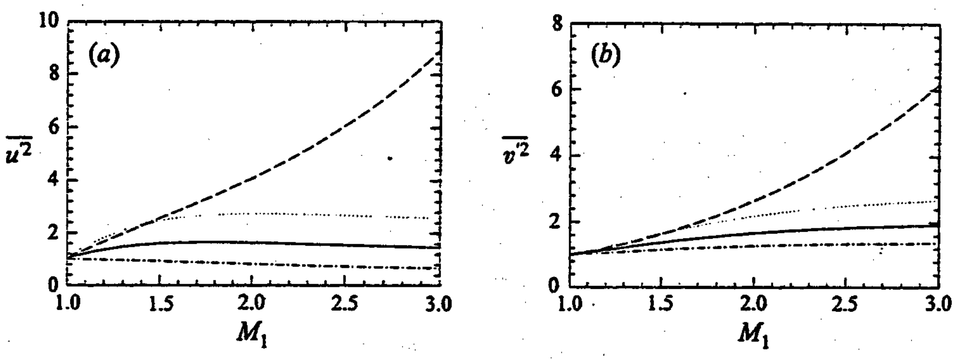

FIGURE 9. (*a*) $\overline{u'^2}$ and (*b*) $\overline{v'^2}$ in the far field of the shock wave as predicted by linear analysis. All the curves are normalized by their upstream values. ——— , pure vorticity; ---- , Morkovin's hypothesis satisfied upstream; ········ , $A_r = 0.54, \phi_r = 0°$; —·— , $A_r = 0.54, \phi_r = 180°$.

T' is negative, then the upstream entropy fluctuations are seen to enhance kinetic energy amplification. This is the trend seen in the DNS. However, if $\overline{u'T'}$ is positive upstream of the shock, the amplification of kinetic energy is strongly suppressed. Practical situations where this might occur include strongly cooled boundary layers, and mixing layers where the mean velocity and density gradients are of opposite sign. This influence of entropy fluctuations increases with increasing Mach number. Figures 9(*a*) and 9(*b*) show linear analysis predictions of kinetic energy amplification in the far field of the shock wave. If Morkovin's hypothesis is assumed to hold upstream, the amplification of $\overline{u'^2}$ is predicted to be enhanced by more than 100% for Mach numbers exceeding about 1.8. The primary reason for this increase in enhancement with increasing Mach number is that $(\rho_{rms}/\bar{\rho})/(q_{rms}/U)$ increases with Mach number if Morkovin's hypothesis is satisfied upstream of the shock wave.

3.2. *Vorticity fluctuations*

All components of vorticity are affected by the upstream entropy fluctuations. As shown in figure 10(*a*), the levels of vorticity fluctuations behind the shock wave are higher in case 1.29B. The amplification of $\overline{\omega_2'^2}$ is seen to increase by 8.7% when entropy fluctuations are present upstream of the shock. This increase is qualitatively predicted by linear analysis. The increase in amplification predicted by analysis is much higher – about 19.4%. The primary reason for this difference between analysis and DNS is believed to be the strict imposition of Morkovin's hypothesis upstream of the shock in the analysis. Owing to the absence of mean temperature gradients, the upstream fluctuations in the simulation only approximately satisfy Morkovin's hypothesis (table 1). Support for this reasoning is provided by the fact that the vorticity amplification in case 1.29A is within 6.3% of analysis while the deviation in case 1.29B is about 16.2%.

Linear analysis predicts the transverse vorticity components to amplify across the shock wave, and remain constant downstream. The streamwise vorticity component is predicted to remain constant across and downstream of the shock. DNS shows that the streamwise vorticity component does indeed remain constant across the shock. However, it increases immediately downstream of the shock wave. In fact, the peak level of $\overline{\omega_1'^2}$ behind the shock wave in case 1.29B is about 7.1% greater than its upstream value. Lee *et al.* (1992) noted for vortical upstream turbulence that this behaviour is nonlinear in nature; it is caused by the stretching of vorticity fluctuations

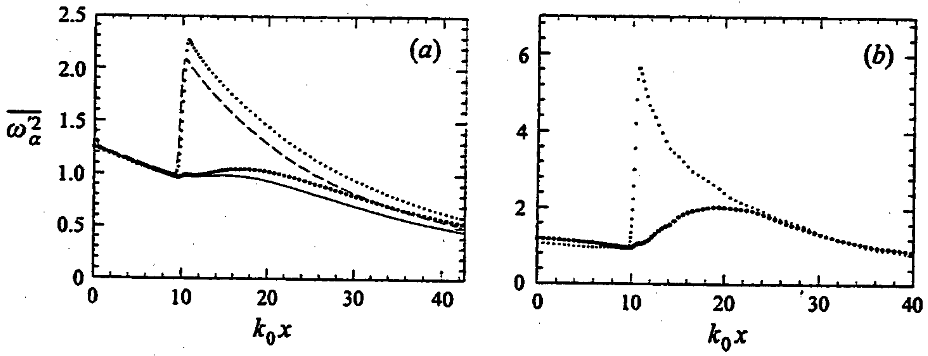

FIGURE 10. Streamwise evolution of vorticity fluctuations from DNS of (*a*) the Mach 1.29 shock wave and (*b*) the Mach 1.8 shock wave. All the curves are normalized by their value immediately upstream of the shock ($k_0x = 8.97$). (*a*) ——, $\overline{\omega_1'^2}$, case 1.29A; ----, $\overline{\omega_2'^2}$, case 1.29A; •, $\overline{\omega_1'^2}$, case 1.29B; ×, $\overline{\omega_2'^2}$, case 1.29B. (*b*) •, $\overline{\omega_1'^2}$; ×, $\overline{\omega_2'^2}$.

by the fluctuating strain rate. In the presence of upstream entropy fluctuations, it is likely that nonlinear baroclinic effects might provide an additional contribution. This downstream rise in $\overline{\omega_1'^2}$ is noticeably higher behind the Mach 1.8 shock. As shown in figure 10(*b*), the peak level of $\overline{\omega_1'^2}$ behind the Mach 1.8 shock is about twice its upstream value. By comparison, Lee *et al.*'s results (in the absence of upstream entropy fluctuations) show that $\overline{\omega_1'^2}$ behind a Mach 2 shock is about 1.5 times its upstream value. The inability to predict this rise in $\overline{\omega_1'^2}$ behind the shock wave is probably the most serious limitation of the linear analysis. Also, it is interesting to note (figures 7 and 10(*b*)) that the vorticity fluctuations in the DNS approach isotropy more rapidly than the velocity fluctuations. This is consistent with the notion that the small scales would return to isotropy more rapidly than the larger scales. Linear analysis is used to determine the influence of mean Mach number on the amplification of the transverse vorticity fluctuations in figure 11. As observed with the turbulence kinetic energy, negative upstream $\overline{u'T'}$ is seen to enhance the amplification of vorticity fluctuations, while positive correlation is seen to suppress it.

3.3. *A simple explanation*

An explanation is provided here for the influence of entropy fluctuations on the evolution of a turbulent flow across a shock wave. Note that Hayes' (1957) results (equation (30) in his paper) for the jump in vorticity across an unsteady shock wave require the unsteady evolution of the shock front to be known accurately enough that derivatives normal and tangent to the front may be obtained. This is quite difficult to obtain from a computation where the shock wave is 'captured' in the Navier–Stokes equations. It is therefore not possible to use Hayes' results to interpret the DNS. Consider the following idealization of the mean field associated with the shock:

$$U = U(x), \quad \bar{p} = \bar{p}(x), \quad \bar{\rho} = \bar{\rho}(x). \tag{3.1}$$

Linearizing the Euler equations about the above mean flow yields the following governing equations for the vorticity fluctuations (denoted by ω'):

$$\omega'_t + U\omega'_x = -\omega' U_x - \frac{\rho'_y}{\bar{\rho}^2}\,\bar{p}_x + \frac{p'_y}{\bar{\rho}^2}\,\bar{\rho}_x. \tag{3.2}$$

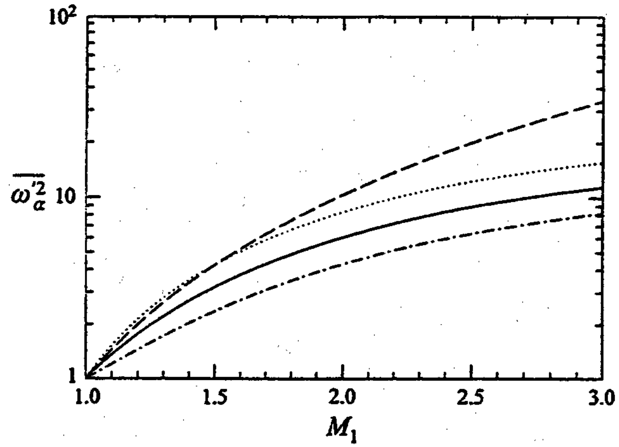

FIGURE 11. Amplification of $\overline{\omega_2'^2} = \overline{\omega_3'^2}$ across the shock wave as predicted by linear analysis. ——, Pure vorticity; – – – –, Morkovin's hypothesis satisfied upstream; ········, $A_r = 0.54, \phi_r = 0°$; —·—·—, $A_r = 0.54, \phi_r = 180°$.

Note that although irrotational acoustic fluctuations are generated at the shock, their contribution to the downstream kinetic energy is not significant; linear analysis (Mahesh *et al.* 1996) shows that vortical fluctuations account for about 99% of the turbulence kinetic energy behind the shock wave. Equation (3.2) represents the effects of bulk change on the evolution of vorticity fluctuations across the shock. Linear effects due to shock distortion are absent. Also, the effects of shock curvature (Hayes 1957) are ignored. As a result of these assumptions, the relations obtained are expected to function more as scaling laws than predictive formulae.

If the incident disturbance comprises vorticity and entropy fluctuations, then $p' = 0$ in the incident field and hence

$$\omega'_t + U\omega'_x = -\omega' U_x - \frac{\rho'_y}{\bar{\rho}^2}\bar{p}_x. \tag{3.3}$$

The term $-\omega' U_x$ represents the effect of bulk compression. The drop in mean velocity across the shock wave indicates that this term would enhance the incident vorticity fluctuations. The incident entropy fluctuations produce vorticity at the shock wave through the baroclinic term. The baroclinic contribution can enhance or oppose the effect of bulk compression. The phase difference between the upstream vorticity and entropy waves determines whether enhancement or opposition is observed.

Consider for example the plane vorticity–entropy wave represented by (A 1*c–e*). It is easily shown that

$$-\omega' U_x - \frac{\rho'_y}{\bar{\rho}^2}\bar{p}_x \sim A_v\, U U_x - A_e\, l\frac{\bar{p}_x}{\bar{\rho}}. \tag{3.4}$$

Since U_x is negative and $\bar{p}_x$ is positive across a shock wave, the two sources of vorticity are of the same sign if A_e and A_v are of the same sign. They oppose each other if A_e and A_v are of opposite sign. Thus if u' and T' are negatively correlated, the entropy field enhances the amplification of fluctuating vorticity. On the other hand, a positive correlation between u' and T' suppresses the amplification of vorticity across the shock wave.

Further insight is gained from a schematic illustration of this effect. Figure 12 shows

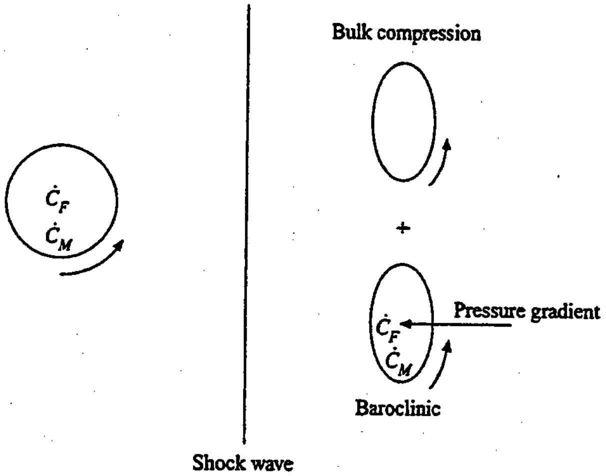

FIGURE 12. A spherical element of fluid passing through a shock wave. The effects of bulk compression and baroclinic vorticity production are shown. u' and T' are negatively correlated upstream of the shock wave.

a fluid element of circular cross-section passing through a shock wave. The geometric centre of this element is denoted by C_F, while C_M denotes the centre of mass. The disturbance field associated with the fluid element is that of a vorticity–entropy wave. The element therefore exhibits solid-body rotation (with associated vorticity ω') which is assumed positive in the direction shown. Also, the density gradient associated with the entropy wave causes the centre of mass to differ from the centre of force (the geometric centre). Note that C_M is below C_F if the correlation between u' and T' is negative. Bulk compression compresses the element in the streamwise direction thereby enhancing the rotation. In addition, the shock wave exerts a pressure force (associated with the adverse pressure gradient) that passes through C_F. This pressure force would exert a torque about the centre of mass. This torque manifests itself as the baroclinic source of vorticity. Note that if C_M is below C_F the baroclinic rotation is in the same direction as the rotation due to bulk compression. It is in the opposite direction if C_M is above C_F (positive correlation between u' and T'). The upstream correlation between u' and T' thus determines the location of C_M with respect to C_F, and thereby the relative sense of rotation that the baroclinic torque produces.

3.4. *Scaling of the evolution of vorticity across a shock wave*

Equation (3.3) is used to derive approximate expressions for the evolution of vorticity fluctuations across the shock. The expressions are evaluated by comparing to the linear analysis predictions. Equation (3.3) is rewritten as

$$\mathrm{D}_t(U\omega') = -\frac{\rho'_y}{\bar{\rho}^2}\, U\bar{p}_x \tag{3.5}$$

where D_t denotes the material derivative $\partial/\partial t + U\partial/\partial x$. Using the relation $\bar{p}_x = -\bar{\rho}UU_x$ in the above equation yields

$$\mathrm{D}_t(U\omega') = \frac{\rho'_y}{\bar{\rho}}\, U^2 U_x = \frac{\rho'_y}{3\bar{\rho}}\, (U^3)_x. \tag{3.6}$$

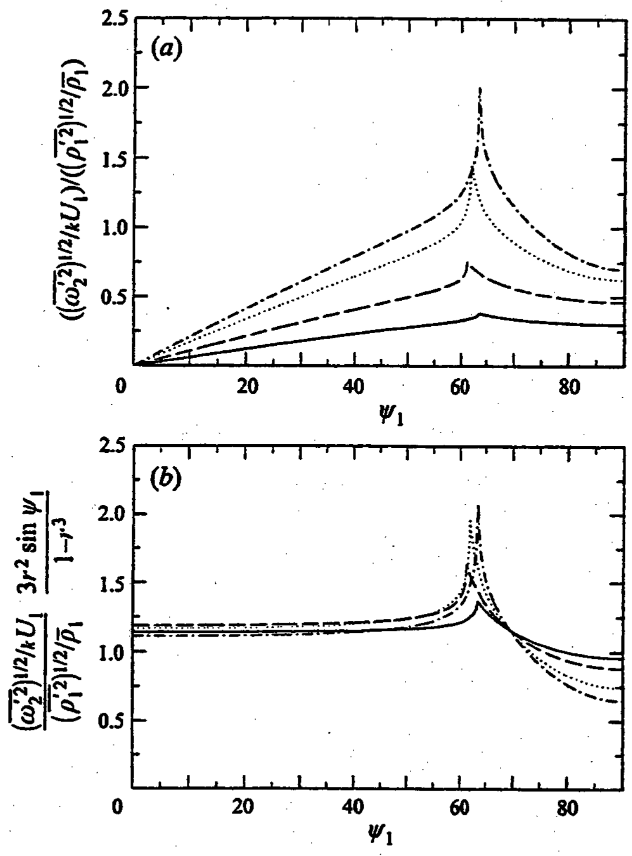

FIGURE 13. (*a*) Unscaled and (*b*) scaled r.m.s. vorticity produced in the interaction of an entropy wave with a shock wave. ——— ($M_1 = 1.25$), ---- ($M_1 = 1.5$), ········ ($M_1 = 2$), —·—·— ($M_1 = 2.5$).

The shock wave is approximated as a discontinuity. $(U^3)_x$ is expressed as $\Delta(U^3)\delta(x)$, where $\Delta(U^3)$ represents the difference in U^3 across the shock wave, and $\delta(x)$ denotes the Dirac delta function. An approximate solution to the above equation is obtained by setting ρ'_y equal to its upstream value (see (A 1*c*–*e*)). Transforming coordinates to $x' = x - Ut, \tau = t$ and integrating yields the following expression for the change in vorticity across the shock wave:

$$U_2\omega_2' - U_1\omega_1' \sim \frac{ikl}{3}A_e\frac{U_2^3 - U_1^3}{U_1}, \tag{3.7}$$

which yields

$$\omega_2' \sim r\omega_1' + \frac{ikl}{3}\,A_e\,U_1\,\frac{1-r^3}{r^2} \tag{3.8}$$

where $r = U_1/U_2$ is obtained from the Rankine–Hugoniot equations. Equation (3.8) suggests that incident vorticity fluctuations amplify by an amount equal to the mean density ratio. The vorticity produced by the incident entropy fluctuations is predicted to scale as $kA_e \sin\psi_1(1-r^3)/r^2$.

These expressions are next compared to linear analysis. Figures 13(*a*) and 13(*b*) show the levels of vorticity produced when an entropy wave interacts with a shock. Mean Mach numbers from 1.25 to 2.5 are considered. Both unscaled and scaled

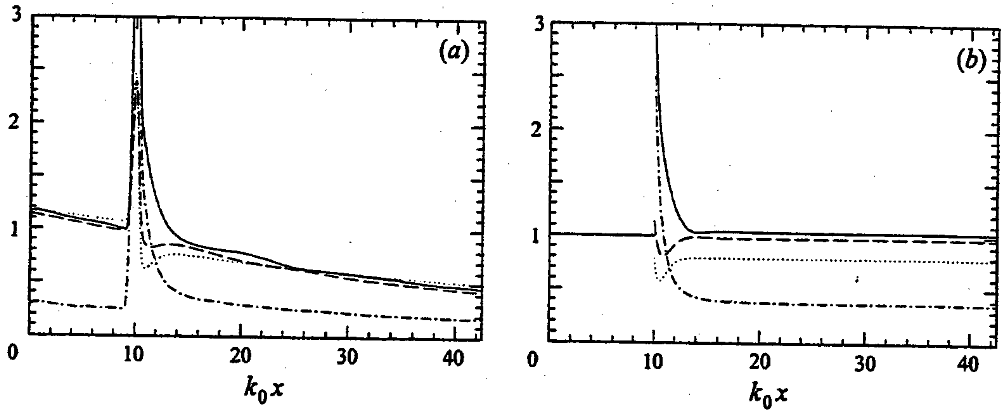

FIGURE 14. The intensities of thermodynamic fluctuations (*a*) from DNS and (*b*) as predicted by linear analysis, for case 1.29B. All variables are non- dimensionalized by the value of $\rho_{rms}/\overline{\rho}$ immediately upstream of the shock wave ($k_0x = 8.97$). ——— , $\rho_{rms}/\overline{\rho}$; ‐ ‐ ‐ ‐ , $T_{rms}/\overline{T}$, ········ , $(\gamma-1)M^2u_{rms}/U$; —·— , $p_{rms}/\gamma\overline{p}$.

values of r.m.s. vorticity behind the shock wave are plotted as a function of incidence angle. The proposed scaling seems to yield reasonable collapse of the curves in the propagating regime. The validity of the scaling for a turbulent field would depend upon the fraction of incident waves in the propagating regime.

The interaction of a vorticity wave with a shock has been considered, and the scaling compared to linear analysis (Mahesh *et al.* 1996). The scaling was less satisfactory: unscaled values ranging from 1 to 6 were collapsed to vary from 0.5 to 1.4. The amplification of incident vorticity was very nearly equal to the mean density ratio for incidence angles near zero; however, a systematic deviation was seen with increasing incidence angle. This evolution of the vorticity waves is in agreement with Jacquin, Cambon & Blin (1993) who observe large discrepancies at the higher Mach numbers when the effect of shock distortion is not represented in the linear limit.

3.5. *Thermodynamic fluctuations and Morkovin's hypothesis*

The thermodynamic fluctuations behind weak shock waves were noted by Lee, Lele & Moin (1994) to be nearly isentropic. The thermodynamic field in case 1.29A follows this trend, i.e. $p_{rms}/\gamma\overline{p}$, $\rho_{rms}/\overline{\rho}$ and $T_{rms}/(\gamma-1)\overline{T}$ are nearly equal over the entire domain. However, upstream entropy fluctuations were not present in Lee *et al.*'s computations. As might be expected, the downstream thermodynamic field is not isentropic when upstream entropy fluctuations are present. Figure 14(*a*) shows the streamwise evolution of the pressure, density, and temperature fluctuations in case 1.29B. The quantity $(\gamma-1)M^2u_{rms}/U$ is also shown. This allows the weak form of Morkovin's hypothesis to be evaluated across the shock. The corresponding predictions made by linear analysis are shown in figure 14(*b*).

Good qualitative agreement is observed between analysis and simulation. The intensity of pressure fluctuations in the near field is seen to be comparable to that of the density and temperature. However, the pressure fluctuations decay behind the shock wave, causing their far-field intensity to be smaller. Considerable deviation from Morkovin's hypothesis is observed in the near field behind the shock. The extent of deviation in the far field is seen to be smaller. The linear analysis predicts a larger deviation from the hypothesis in the far field than the DNS. Owing to viscous decay, the notion of far field is not as precise in the DNS as it is in the analysis. Linear

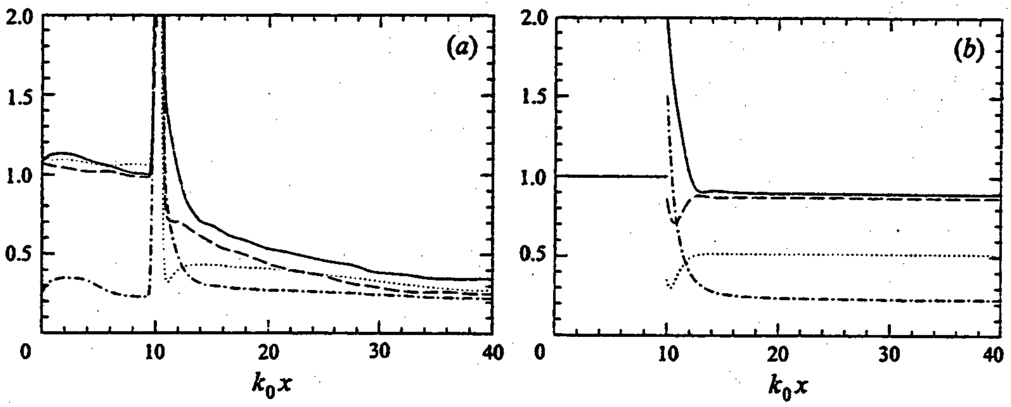

FIGURE 15. Thermodynamic fluctuations (*a*) from DNS and (*b*) as predicted by linear analysis, for case 1.8. All variables are non-dimensionalized by the value of $\rho_{rms}/\bar{\rho}$ immediately upstream of the shock wave. ——, $\rho_{rms}/\bar{\rho}$; ----, $T_{rms}/\overline{T}$, ········, $(\gamma-1)M^2u_{rms}/U$; —·—, $p_{rms}/\gamma\bar{p}$.

analysis suggests (figure 14(*b*)) that the far-field values are attained at approximately $k_0x = 17$. If the weak form of Morkovin's hypothesis is evaluated at this location in the computation, it shows behaviour comparable to analysis. Interestingly however, the validity of the hypothesis in the DNS is seen to increase with distance downstream of this location. The exact cause of this trend is not known. Also, although the r.m.s values of the terms in the hypothesis approach each other behind the shock in the DNS, $\overline{u'T'}/u_{rms}T_{rms}$ does not approach -1. It drops in magnitude across the shock, and decreases further in magnitude downstream, e.g. the correlation coefficient at $k_0x = 20$ is -0.54.

A similar trend is observed in the Mach 1.8 computation. Morkovin's hypothesis is evaluated across the Mach 1.8 shock wave in figures 15(*a*) and 15(*b*) respectively. The far-field values in the analysis are attained at about $k_0x = 15$. Both analysis and DNS show considerable deviation from the hypothesis at this location. However, the intensities of the density and temperature fluctuations decay behind the shock wave in the DNS, resulting in increased validity of the hypothesis behind the shock. Interestingly, although $\rho_{rms}/\bar{\rho}$, $T_{rms}/\overline{T}$ and $(\gamma-1)M^2u_{rms}/U$ approach each other behind the shock, the intensity of the pressure fluctuations is not negligible. As seen in figure 15(*a*), $p_{rms}/\gamma\bar{p}$ is nearly of the same magnitude as $T_{rms}/\overline{T}$ at about $k_0x = 40$. Also, $\overline{u'T'}/u_{rms}T_{rms}$ does not approach -1. Its value at $k_0x = 20$ is -0.22.

Linear analysis is used to examine the influence of mean Mach number on the validity of Morkovin's hypothesis across the shock wave. The incident fluctuations are constrained to satisfy the strict form of the hypothesis. The fluctuations in the far field are then examined to see if the hypothesis holds in the r.m.s. sense. The results (figure 16) show that the first part of the hypothesis, i.e. $\rho_{rms}/\bar{\rho} = T_{rms}/\overline{T}$, is still a good approximation behind the shock wave (especially if M_1 is less than about 2). However, the part of the hypothesis that relates T' to u' exhibits large deviation with Mach number. This behaviour is explained below.

The equation $\rho'/\bar{\rho} = -T'/\overline{T}$ is obtained by setting p' to zero in the linearized equation of state. It amounts to neglecting the acoustic mode in comparison to the entropy mode. As seen from (*A*1*d*), it holds exactly for the upstream turbulence. Upon interaction with the shock, the incident fields of vorticity and entropy fluctuations generate acoustic waves. The generation of acoustic waves is however accompanied by amplification of the incident entropy fluctuations. Also, a fraction of

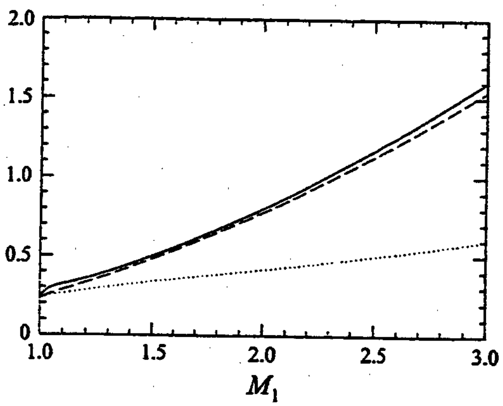

FIGURE 16. Evaluation of Morkovin's hypothesis in the far field of the shock wave using linear analysis. All the curves are non-dimensionalized by the upstream value of u_{rms}/U. ——, $\rho_{rms}/\overline{\rho}$; ----, $T_{rms}/\overline{T}$; ········, $(\gamma-1)M^2u_{rms}/U$.

the acoustic waves decays behind the shock. As a result, the acoustic contribution to the thermodynamic fluctuations in the far field is significant only at the larger Mach numbers. The first part of the weak form of Morkovin's hypothesis is therefore a good approximation behind shock waves of moderate strength.

The relation

$$\frac{T'}{\overline{T}} = -(\gamma-1)M^2\frac{u'}{U} \tag{3.9}$$

is obtained by assuming that stagnation temperature fluctuations are small in the linear limit. Denote the stagnation temperature by T_0,

$$T_0 = \overline{T} + T' + \frac{(U+u')^2 + v'^2 + w'^2}{2C_p}, \tag{3.10}$$

where C_p denotes the specific heat at constant pressure. Linearizing the above equation yields the following expression for fluctuations in stagnation temperature: $T_0' = T' + Uu'/C_p$. Setting T_0' to zero and rearranging yields (3.9).

In the linear limit, fluctuations in stagnation temperature obey the relation, $\mathrm{D}T_0'/\mathrm{D}t = \partial p'/\partial t$ behind the shock wave ($\mathrm{D}/\mathrm{D}t$ denotes the material derivative based on the mean velocity). Decomposing the temperature field into acoustic and entropic components, and the velocity into acoustic and vortical components allows decomposition of T_0' into $T'_{0_{ent}}$ and $T'_{0_{acous}}$ such that $\mathrm{D}T'_{0_{ent}}/\mathrm{D}t = 0$ and $\mathrm{D}T'_{0_{acous}}/\mathrm{D}t = \partial p'/\partial t$. Next, the Rankine–Hugoniot equations may be used to show that (3.9) cannot be valid behind a shock wave if it is assumed to hold upstream of the shock. The energy equation requires the stagnation temperature to be constant across the shock in a frame of reference that moves at the instantaneous speed of the shock wave, i.e.

$$\overline{T}_1 + T_1' + \frac{(U_1 + u_1' - \xi_t)^2 + v_1'^2 + w_1'^2}{2C_p} = \overline{T}_2 + T_2' + \frac{(U_2 + u_2' - \xi_t)^2 + v_2'^2 + w_2'^2}{2C_p}. \tag{3.11}$$

Linearizing the above equation and constraining the incident fluctuations to satisfy (3.9) yields

$$T_2' + \frac{U_2u_2'}{C_p} = -\frac{\xi_t}{C_p}(U_1 - U_2), \tag{3.12}$$

i.e. the fluctuations of stagnation temperature are not zero immediately behind the

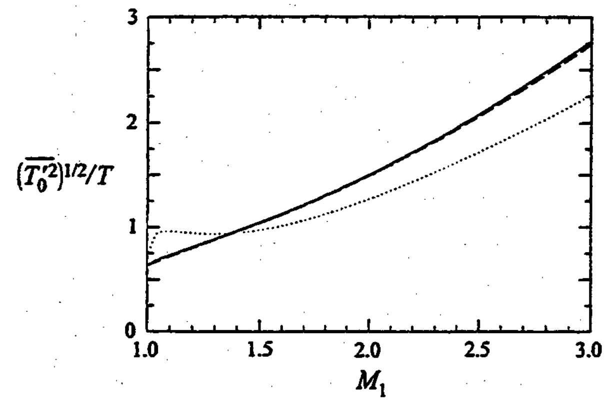

FIGURE 17. Decomposition of stagnation temperature fluctuations using linear analysis. All the curves are non-dimensionalized by the upstream value of u_{rms}/U. ——— , Far-field value; ---- , contribution due to vorticity and entropy fluctuations; ········ , near-field value.

shock wave. Dividing through by $\overline{T}_2$ and rearranging, we get

$$\frac{T_2'}{\overline{T}_2} + (\gamma - 1)M_2^2\frac{u_2'}{U_2} = -(\gamma - 1)M_2\left(\frac{U_1}{U_2} - 1\right)\frac{\xi_t}{a_2}. \tag{3.13}$$

Thus, applicability of Morkovin's hypothesis immediately behind the shock wave requires that

$$(\gamma - 1)M_2\left(\frac{U_1}{U_2} - 1\right)\frac{\xi_t}{a_2} \sim 0. \tag{3.14}$$

The r.m.s. values of the near-field ($k_0x = 10$) stagnation temperature are plotted in figure 17 as a function of the mean Mach number. The plotted values are seen to be comparable to the terms in Morkovin's hypothesis (figure 16). The hypothesis is therefore invalid immediately behind the shock wave. The above argument is next extended to show why the hypothesis does not hold in the far field. Decomposition of the stagnation temperature fluctuations into vorticity–entropy and acoustic components shows that both near- and far-field values of the stagnation temperature fluctuations are dominated by the vorticity–entropy component. As shown in figure 17, the vorticity–entropy component is nearly equal to the total level in the far field, while its contribution to the near-field level is greater than 80% over the range of Mach numbers shown. Figure 17 and (3.13) therefore show that appreciable levels of stagnation temperature fluctuations are generated immediately behind the shock wave due to oscillation of the shock front. Most of these fluctuations arise from vorticity–entropy fluctuations, which convect downstream to generate an appreciable level of stagnation temperature fluctuations in the far field of the shock wave. This leads to inapplicability of Morkovin's hypothesis in the far field.

4. Summary

Direct numerical simulation and inviscid linear analysis were used to study the interaction of a normal shock wave with an isotropic turbulent field of vorticity and entropy fluctuations. Shock waves of strength Mach 1.29 and Mach 1.8 were computed using DNS, while the linear analysis considered a range of Mach numbers from 1 to 3. Our objective was to study the role of the upstream entropy fluctuations in the evolution of the turbulent flow across the shock.

The upstream entropy fluctuations were shown to significantly affect shock/turbulence interaction. The magnitude of the entropy fluctuations, and the sign of the upstream velocity–temperature correlation were both seen to be important. Higher levels of kinetic energy and vorticity amplification were observed across the shock when u' and T' were negatively correlated upstream of the shock. Positive correlation had the opposite effect. An explanation was provided to explain these trends. The evolution of fluctuating vorticity across the shock wave was noted to have two important contributions: bulk compression of incident vorticity and baroclinic production of vorticity through the incident entropy fluctuations. The upstream correlation between vorticity and entropy fluctuations was shown to determine whether these two sources of vorticity enhance or oppose each other, thereby determining kinetic energy levels behind the shock wave. A scaling was then proposed for the evolution of vorticity across the shock wave. Since Morkovin's hypothesis is known to apply in adiabatic turbulent boundary layers, the results suggest that the entropy fluctuations in the boundary layer would play a very significant role in the interaction between the boundary layer and a shock wave.

The validity of Morkovin's hypothesis behind a shock was examined. Linear analysis indicates that neglecting the acoustic mode is a good approximation in the far field of shock waves of moderate strength ($M_1 < 2$). The part of the hypothesis relating u' and T' was predicted to be invalid. Non-negligible oscillation of the shock front was shown to be responsible. The thermodynamic fluctuations in the simulations followed linear analysis predictions immediately behind the shock. Interestingly however, the terms in the weak form of the hypothesis approached each other as the solution decayed behind the shock. Despite this trend, the pressure fluctuations in the DNS were not negligible in the far field. Also, $\overline{u'T'}$ did not approach −1. Its value in the far field was about −0.54 and −0.22 for the Mach 1.29 and Mach 1.8 shock waves.

This study was supported by the Air Force Office of Scientific Research under Grant 88-NA-322 and Contract F49620-92-J-0128 with Dr Leonidas Sakell as the technical monitor. The authors would also like to express their gratitude to NAS and NASA-Ames Research Center for the use of their computer facilities.

Appendix

The linear analysis is summarized below. The interaction of a single vorticity–entropy wave with a shock is first considered in §A.1. The analysis is then extended in §A.2 to describe the evolution of the turbulent field across the shock.

A.1. *Interaction of a shock with a plane vorticity–entropy wave*

The two-dimensional interaction of a shock wave with a plane vorticity–entropy wave is schematically illustrated in figure 18. Note that the shock wave is stationary in the mean. The variables $U, \overline{p}, \overline{\rho}, \overline{T}$ and M denote the mean velocity, pressure, density, temperature and Mach number respectively and subscripts 1 and 2 denote the upstream and downstream states. The flow upstream of the shock wave is perturbed by the weak disturbance field of the incident vorticity–entropy wave which is assumed to be a plane wave that makes angle ψ_1 with the x-axis. The variables u', v', p', ρ' and T' represent the fluctuating velocities, pressure, density and temperature. The

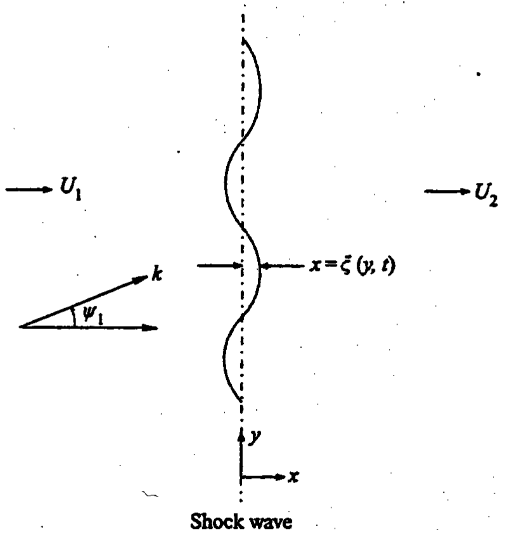

FIGURE 18. Schematic of the interaction of a vorticity–entropy wave with a shock wave.

incident field has the following form:

$$\frac{u_1'}{U_1} = lA_v\,\mathrm{e}^{ik(mx+ly-U_1mt)}, \quad \frac{v_1'}{U_1} = -mA_v\,\mathrm{e}^{ik(mx+ly-U_1mt)}, \tag{A 1a,b}$$

$$\frac{\rho_1'}{\bar{\rho}_1} = A_e\,\mathrm{e}^{ik(mx+ly-U_1mt)}, \quad \frac{T_1'}{\overline{T}_1} = -\frac{\rho_1'}{\bar{\rho}_1}, \quad p_1' = 0, \tag{A 1c–e}$$

where $m = \cos\psi_1$ and $l = \sin\psi_1$. The shock wave deforms in response to the incident disturbance; the displacement is denoted by $x = \xi(y, t)$.

Details of the analysis may be found in Mahesh *et al.* (1996). The solution obtained is summarized below. The solution behind the shock wave is a superposition of vortical, acoustic and entropic components. It has the following dimensionless form:

$$\frac{1}{A_v}\frac{u_2'}{U_1} = \widetilde{F}\,\mathrm{e}^{i\tilde{k}x}\mathrm{e}^{ik(ly-mU_1t)} + \widetilde{G}\,\mathrm{e}^{ik(mrx+ly-mU_1t)}, \tag{A 2a}$$

$$\frac{1}{A_v}\frac{v_2'}{U_1} = \widetilde{H}\,\mathrm{e}^{i\tilde{k}x}\mathrm{e}^{ik(ly-mU_1t)} + \widetilde{I}\,\mathrm{e}^{ik(mrx+ly-mU_1t)}, \tag{A 2b}$$

$$\frac{1}{A_v}\frac{p_2'}{\overline{p_2}} = \widetilde{K}\,\mathrm{e}^{i\tilde{k}x}\mathrm{e}^{ik(ly-mU_1t)}, \tag{A 2c}$$

$$\frac{1}{A_v}\frac{\rho_2'}{\bar{\rho}_2} = \frac{\widetilde{K}}{\gamma}\,\mathrm{e}^{i\tilde{k}x}\mathrm{e}^{ik(ly-mU_1t)} + \widetilde{Q}\,\mathrm{e}^{ik(mrx+ly-mU_1t)}, \tag{A 2d}$$

$$\frac{1}{A_v}\frac{T_2'}{\overline{T}_2} = \frac{\gamma-1}{\gamma}\widetilde{K}\,\mathrm{e}^{i\tilde{k}x}\mathrm{e}^{ik(ly-mU_1t)} - \widetilde{Q}\,\mathrm{e}^{ik(mrx+ly-mU_1t)}. \tag{A 2e}$$

The boundary conditions across the shock wave yield the following expressions for the velocity and slope of the shock front:

$$\frac{1}{A_v}\frac{\xi_t}{U_1} = \widetilde{L}\,\mathrm{e}^{ik\,(ly-mU_1t)}, \quad \frac{1}{A_v}\xi_y = -\frac{l}{m}\widetilde{L}\,\mathrm{e}^{ik\,(ly-mU_1t)}. \tag{A 3}$$

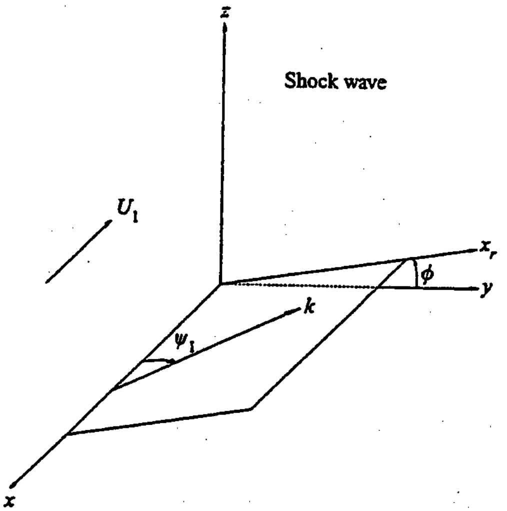

FIGURE 19. Coordinate system used in the interaction of isotropic turbulence with a shock wave.

The variable r denotes the mean density ratio $\overline{\rho}_2/\overline{\rho}_1$ across the shock wave; $\tilde{k}(M_1, \psi_1)$ represents the streamwise wavenumber of the acoustic component behind the shock wave. It is real in the propagating regime and complex in the decaying regime. The coefficients $\tilde{F}, \tilde{H}$ and $\tilde{K}$ are associated with the acoustic component. The vortical component is represented by $\tilde{G}$ and $\tilde{I}$ while $\tilde{Q}$ represents the entropy component. The coefficients $\tilde{F}, \tilde{H}, \tilde{K}, \tilde{G}, \tilde{I}$ and $\tilde{Q}$ are functions of M_1, ψ_1 and the amplitude ratio (A_r) and phase difference (ϕ_r) between the vorticity and entropy waves, i.e. $A_r e^{i\phi_r} = A_e/A_v$. Expressions for the coefficients are given in Mahesh *et al.* (1996).

A.2. *Interaction of a shock wave with an isotropic turbulent field*

As suggested by Morkovin's hypothesis, the upstream turbulence is represented as a random three-dimensional field of vorticity–entropy waves. The turbulent velocity field is assumed to be isotropic. The incident turbulent field is represented as a superposition of plane vorticity–entropy waves (Fourier modes) in three dimensions. Each of these waves would interact independently with the shock wave under linear analysis. For a given upstream spectrum, the interaction of each wave with the shock wave is predicted. The solution is integrated over all incident waves to obtain turbulence statistics behind the shock.

The three-dimensional problem is related to the two-dimensional analysis of the preceding section as follows. Consider an incident plane wave in three dimensions. As shown in figure 19, the wavenumber vector of the wave lies in a plane that makes angle ϕ with the y-axis. In this plane, which we call the (x, x_r)-plane, the wave makes angle ψ_1 with the x-axis. It is readily seen that the (x, x_r)-plane is identical to the plane of interaction in the two-dimensional problem. The solenoidal nature of the incident velocity field requires the velocity vector of the wave to be normal to the wavenumber vector. The velocity field may therefore be expressed as a sum of two components: one normal to the wavenumber vector in the (x, x_r)-plane and the other normal to the (x, x_r)-plane (the ϕ-direction). It is intuitively clear that the ϕ-component of velocity would pass unchanged through the shock wave. As a result, the three-dimensional problem may be solved using results of the two-dimensional analysis in the (x, x_r)-plane.

Results from §A.1 are used to obtain expressions for the energy spectra behind the shock wave. The spectra depend upon the upstream three-dimensional energy spectrum, $E(k)$. This paper assumes the following form for $E(k)$:

$$E(k) \sim \left(\frac{k}{k_0}\right)^4 \mathrm{e}^{-2(k/k_0)^2}. \tag{A 4}$$

The results also depend upon the upstream density spectrum. The quantity A_e/A_v may be represented as $A_r \mathrm{e}^{\mathrm{i}\phi_r}$, where A_r and ϕ_r are both functions of the wavenumber vector. Appropriate functional dependencies may be assumed depending upon the flow being considered. This paper presents results for $\phi_r = 0$ and π, i.e. the density field is either perfectly correlated or perfectly anti-correlated with the velocity field, Also, two forms of the upstream density spectrum are considered. One case assumes the density field to be isotropic with the same three-dimensional spectrum as the velocity field, i.e. A_r is assumed constant. For this case it is easily shown that

$$A_r = \sqrt{2}\frac{(\overline{\rho_1'^2})^{1/2}/\overline{\rho_1}}{(\overline{q_1^2})^{1/2}/U_1}. \tag{A 5}$$

The second case assumes that the density field satisfies Morkovin's hypothesis at every wavenumber. If the velocity fluctuations are isotropic, it is easily seen that the resulting density field is axisymmetric, i.e.

$$A_r = (\gamma - 1)M^2 \sin\psi_1. \tag{A 6}$$

The spectra are then numerically integrated to obtain the turbulence statistics behind the shock. Further details are provided by Mahesh *et al.* (1996).

REFERENCES

Bradshaw, P. 1974 The effect of mean compression or dilatation on the turbulence structure of supersonic boundary layers. *J. Fluid Mech.* **63**, 449–464.

Bradshaw, P. 1977 Compressible turbulent shear layers. *Ann. Rev. Fluid Mech.* **9**, 33–54.

Chang, C. T. 1957 Interaction of a plane shock and oblique plane disturbances with special reference to entropy waves. *J. Aero. Sci.* **24**, 675–682.

Colonius, T., Moin, P. & Lele, S. K. 1995 Direct computation of aerodynamic sound. *Rep. TF-65*. Department of Mechanical Engineering, Stanford University, Stanford, California.

Cuadra, E. 1968 Flow perturbations generated by a shock wave interacting with an entropy wave. *AFOSR-UTIAS Symp. on Aerodynamic Noise, Toronto*, pp. 251–271. University of Toronto Press.

Debieve, F. R., Gouin, H. & Gaviglio, J. 1982 Evolution of the Reynolds stress tensor in a shock wave-turbulence interaction. *Indian J. Technol.* **20**, 90–97.

Debieve, J. F. & Lacharme, J. P. 1986 A shock wave/free-turbulence interaction. In *Turbulent Shear Layer/Shock Wave Interactions* (ed. J. Delery). Springer.

Dolling, D. S. 1993 Fluctuating loads in shock wave/turbulent boundary layer interaction: tutorial and update. *AIAA Paper* 93-0284.

Dussauge, J. P. & Gaviglio, J. 1987 The rapid expansion of a supersonic turbulent flow: role of bulk dilatation. *J. Fluid Mech.* **174**, 81–112.

Erlebacher, G., Hussaini, M. Y., Speziale, C. G. & Zang, T. A. 1992 Towards the large eddy simulation of compressible turbulent flows. *J. Fluid Mech.* **238**, 155–185.

Fernholz, H. H. & Finley, P. J. 1981 A further compilation of compressible boundary layer data with a survey of turbulence data. *AGARDograph* 263.

Givoli, D. 1991 Non-reflecting boundary conditions. *J. Comput. Phys.* **94**, 1–29.

Goldstein, M. E. 1979 Turbulence generated by the interaction of entropy fluctuations with non-uniform mean flows. *J. Fluid Mech.* **93**, 209–224.

GREEN, J. E. 1970 Interaction between shock waves and turbulent boundary layers. *Prog. Aerospace Sci.* **11**, 235–340.

HAYES, W. D. 1957 The vorticity jump across a gasdynamic discontinuity. *J. Fluid Mech.* **2**, 595–600.

HESSELINK, L. & STURTEVANT, B. 1988 Propagation of weak shocks through a random medium. *J. Fluid Mech.* **196**, 513–553.

HONKAN, A. & ANDREOPOULOUS, J. 1992 Rapid compression of grid-generated turbulence by a moving shock wave. *Phys. Fluids* A **4**, 2562–2572.

ISRAELI, M. & ORSZAG, S. A. 1981 Approximation of radiation boundary conditions. *J. Comput. Phys.* **41**, 115–135.

JACQUIN, L., BLIN, E. & GEFFROY, P. 1991 Experiments on free turbulence/shock wave interaction. *Proc. Eighth Symp. on Turbulent Shear Flows, Munich* (ed. F. Durst, R. Friedrich, B. E. Launder, F. W. Schmidt, U. Schumann & J. H. Whitelaw). Springer.

JACQUIN, L., CAMBON, C. & BLIN, E. 1993 Turbulence amplification by a shock wave and rapid distortion theory. *Phys. Fluids* A **5**, 2539–2550.

KELLER, J. & MERZKIRCH, W. 1990 Interaction of a normal shock wave with a compressible turbulent flow. *Exps. Fluids* **8**, 241–248.

KOVASZNAY, L. S. G. 1953 Turbulence in supersonic flow. *J. Aero. Sci.* **20**, 657–682.

LEE, S., LELE, S. K. & MOIN, P. 1992 Simulation of spatially evolving turbulence and the applicability of Taylor's hypothesis in compressible flow. *Phys. Fluids* A **4**, 1521–1530.

LEE, S., LELE, S. K. & MOIN, P. 1993 Direct numerical simulation of isotropic turbulence interacting with a weak shock wave. *J. Fluid Mech.* **251**, 533–562. Also see Corrigendum, *J. Fluid Mech.* **264**, 373–374.

LEE, S., LELE, S. K. & MOIN, P. 1994 Interaction of isotropic turbulence with a strong shock wave. *AIAA Paper* 94-0311.

LELE, S. K. 1992 Compact finite difference schemes with spectral-like resolution. *J. Comput. Phys.* **103**, 16–42.

LELE, S. K. 1994 Compressibility effects on turbulence. *Ann. Rev. Fluid Mech.* **26**, 211–254.

LINDQUIST, D. R. & GILES, M. B. 1991 On the validity of linearized unsteady Euler equations with shock-capturing. *AIAA Paper* 91-1598-CP.

MAHESH, K., LEE, S., LELE, S. K. & MOIN, P. 1995 The interaction of an isotropic field of acoustic waves with a shock wave *J. Fluid Mech.* **300**, 383–407.

MAHESH, K., LELE, S. K. & MOIN, P. 1993 The response of anisotropic turbulence to rapid homogeneous one-dimensional compression. *Phys. Fluids* **6**, 1052–1062.

MAHESH, K., LELE, S. K. & MOIN, P. 1996 The interaction of a shock wave with a turbulent shear flow. *Report* TF-69. Thermosciences Division, Mechanical Engineering Department, Stanford University, Stanford, CA.

MEADOWS, K. R., CAUGHEY, D. A. & CASPER, J. 1993 Computing unsteady shock waves for aeroacoustic applications. *AIAA Paper* 93-4329.

MORKOVIN, M. V. 1960 Note on the assessment of flow disturbances at a blunt body traveling at supersonic speeds owing to flow disturbances in the free stream. *Trans. ASME, J. Appl. Mech.*, No. 60-APM-10.

MORKOVIN, M. V. 1961 Effects of compressibility on turbulent flows. In *Mecanique de la Turbulence* (ed. A. Favrè), pp. 367–380. Paris, Editions du Centre National de la Recherche Scientifique.

POINSOT, T. J. & LELE, S. K. 1992 Boundary conditions for direct simulation of compressible viscous reacting flow. *J. Comput. Phys.* **101**, 104–129.

RIBNER, H. S. 1953 Convection of a pattern of vorticity through a shock wave. *NACA TN* 2864.

RIBNER, H. S. 1954 Shock-turbulence interaction and the generation of noise. *NACA TN* 3255.

ROBERTS, T. W. 1990 The behavior of flux difference splitting schemes near slowly moving shocks. *J. Comput. Phys.* **90**, 141–160.

SETTLES, G. S. & DODSON, L. J. 1994 Supersonic and hypersonic shock/boundary-layer interaction database. *AIAA J.* **32**, 1377–1383.

SHU, C.-W. 1990 Numerical experiments on the accuracy of ENO and modified ENO schemes. *J. Sci. Comput.* **5**, 127–149.

SHU, C.-W. & OSHER, S. 1988 Efficient implementation of essentially non-oscillatory shock-capturing schemes. *J. Comput. Phys.* **77**, 439–471.

SHU, C.-W. & OSHER, S. 1989 Efficient implementation of essentially non-oscillatory shock-capturing schemes II. *J. Comput. Phys.* **83**, 32–78.

SMITS, A. J. & MUCK, K. C. 1987 Experimental study of three shock wave/turbulent boundary layer interactions. *J. Fluid Mech.* **182**, 294–314.

TAVOULARIS, S., BENNETT, J. C. & CORRSIN, S. 1978 Velocity-derivative skewness in small Reynolds number, nearly isotropic turbulence. *J. Fluid Mech.* **176**, 33–66.

WOODWARD, P. & COLLELA, P. 1984 The numerical simulation of two-dimensional flow through shocks. *J. Comput. Phys.* **54**, 115–173.

WRAY, A. A. 1986 Very low storage time-advancement schemes. *Internal Rep.* NASA-Ames Research Center, Moffett Field, CA.